Molecular Electronics: When Multiple Orbitals Matter

Koole, Max

DOI
10.4233/uuid:8d7ac522-9d79-4af5-b2e3-7eeccab06055

Publication date
2017

Document Version
Final published version

Citation (APA)
Koole, M. (2017). *Molecular Electronics: When Multiple Orbitals Matter*. [Dissertation (TU Delft), Delft University of Technology]. https://doi.org/10.4233/uuid:8d7ac522-9d79-4af5-b2e3-7eeccab06055

MOLECULAR ELECTRONICS: WHEN MULTIPLE ORBITALS MATTER

MOLECULAR ELECTRONICS:
WHEN MULTIPLE ORBITALS MATTER

Proefschrift

ter verkrijging van de graad van doctor
aan de Technische Universiteit Delft,
op gezag van de Rector Magnificus prof. ir. K.C.A.M. Luyben,
voorzitter van het College voor Promoties,
in het openbaar te verdedigen op 3 februari 2017 om 10:00 uur

door

Max KOOLE

natuurkundig ingenieur
geboren te Seria, Brunei.

Dit proefschrift is goedgekeurd door de promotor:

Prof. dr. ir. H. S. J. van der Zant

Samenstelling promotiecommissie:

Rector Magnificus,	voorzitter
Prof. dr. ir. H. S. J. van der Zant,	Technische Universiteit Delft, promotor
Dr. F. C. Grozema,	Technische Universiteit Delft, co-promotor
Onafhankelijke leden:	
Prof. dr. Y. M. Blanter,	Technische Universiteit Delft
Prof. dr. L. Kuipers,	Technische Universiteit Delft
Prof. dr. J. C. Hummelen,	Rijksuniversiteit Groningen
Prof. dr. P. Hedegård,	Københavns Universitet
Prof. dr. P. Lafarge,	Université Paris Diderot

Keywords: Molecular electronics, charge transport, conjugation, Kondo effect, quantum interference, electromigration, nanotechnology

Printed by: Gildeprint - Enschede

Front & Back: Art and design by Anje Eichhorn.

Casimir PhD Series, Delft-Leiden 2016-41

ISBN 978-90-8593-284-0

An electronic version of this dissertation is available at
http://repository.tudelft.nl/.

J. L. M. Koole

CONTENTS

1

INTRODUCTION

In this chapter we introduce the field of molecular electronics and discuss its relevance to society. Conjugation in organic molecules and experimental methods of measuring current through a single molecule are explained. Extra emphasis is put on the electromigration technique as it is the dominant technique used in this thesis.

1

The fact that electrons can move through materials has had an enormous impact on society. Known as electricity, electricity lights our homes, powers our appliances and, increasingly, our cars. It is at the base of computers; they compute by moving electrons around. However, in most cases, it is not the electron itself that defines the function of a device, but it is the conductive materials of which the device is built. For example, the electron itself does not shine in a light bulb, but it is the metallic filament that glows due to electrons moving through it. The electron's interaction with a material therefore gives a device its function.

In the 19th century and the beginning of the 20th century metals, such as gold and copper, were the prevailing materials to build electrical devices from. A metal on its own can act as a wire, moving electrons from A to B, and heat up (glow) when enough electrons are supplied. In itself, metals have little intrinsic functionality when electrons move through them. To create an electrical device from metals significant engineering is needed. By placing a metallic wire in an inert atmosphere a lamp can be made or when metallic conductors interact with magnets, motors can be created. Nowadays alternating-current motors that drive trains, and possibly your car, are widespread and until ten years ago filament light-bulbs were in every home.

In 1943 the first all-electric computer was developed. It used vacuum-tube transistors which work due to thermionic emission from metals. To use vacuum-tube transistors to build the phones and laptops we have today is impossible due to the fact that vacuum-tube transistors can not easily be scaled down. Semiconductor based transistors were needed to realize the miniaturization that happened in the last few decades. Semiconductor materials (e.g. silicon, gallium arsenide) have the property that with ion-doping the electronic properties in the material can be changed locally. Furthermore semiconductors, much more than metals, are sensitive to external stimuli like, for example, electric fields, magnetic fields and temperature. These two factors make it possible that with a semiconductor material more functionality can be created when electrons flow through it, than with metals. This decreases the challenges in engineering (figure 1.1), making it in the case of semiconductor transistors possible to build them orders of magnitude smaller than metallic vacuum-tube transistors. Resulting in the powerful and energy-efficient smartphones and laptops we have today.

Materials with more intrinsic functionality when electrons move through them, make it possible to reduce the engineering challenge to build more advanced devices. This is one of the main driving factors behind academic research on new materials and how electrons behave in them. Which material will help us further advance society? There are many options and it is likely not a single material on its own. A few examples of novel electronic materials in development are: complex oxides that show high-temperature superconductivity[1] and 2D-materials which since their discovery in 2004 have shown high electron-mobility[2]. Another promising route is to shape pre-existing materials (e.g. metals, semiconductors) on the nanometer scale. This gives rise to quantum mechanical effects resulting in novel functionality; an example

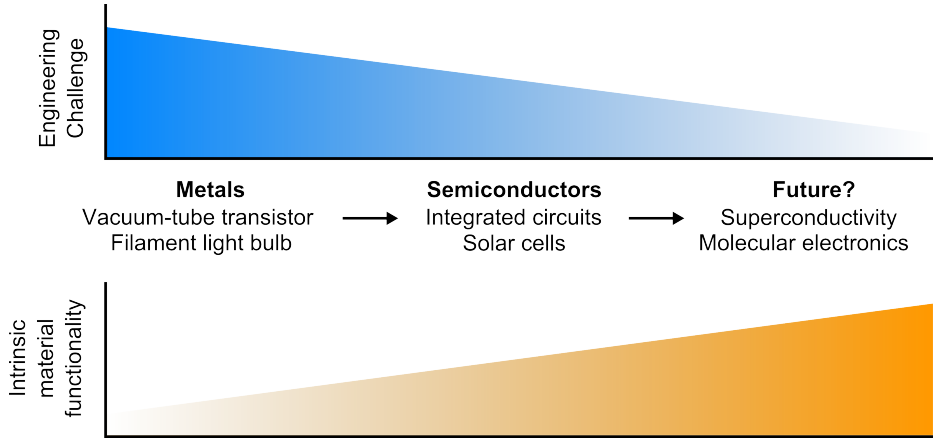

Figure 1.1: Material functionality and engineering challenge. The development of new electronic materials with increased intrinsic functionality, decreases the challenges in engineering for a specific application.

is the semiconductor quantum-dot television. In this thesis we will investigate organic molecules as a potential new electronic material that can help advance society.

1.1. ORGANIC MOLECULES

Organic molecules are molecules with one or more atoms of carbon covalently linked to atoms of other elements, for example hydrogen or oxygen. The term "organic" originates from the fact that scientists in the past thought that organic molecules could only be synthesized by living beings; fortunately nowadays this can be done artificially. Examples of organic molecules are methane (CH_4) and benzene (C_6H_6) but also sugars (sucrose ($C_6H_{12}O_6$)), vitamins and fats which are abundantly present in our body. When joining organic molecules together in long chains a polymer is formed, which is the basis of most plastics used today.

Most polymers are excellent isolators, they can for instance be used as coating around electricity cables. This shows that materials made from organic molecules do not necessarily conduct electrons well. Conduction in these materials is determined by how well electrons move in between molecules and within the molecules. Conduction in between molecules is a big research field and although we will allude to it in chapter 6 it is not the topic of this thesis. In this thesis we will study electron transport within molecules.

An interesting class of molecules to study is conjugated molecules, as they have the property that electrons can move through them relatively easily. Conjugation is determined by how the carbon atoms in the molecule bond. Carbon needs four bonds, as it has four electrons in its outer shell to share with other atoms. The first bond a carbon atom makes with a neighbouring atom is a σ-bond. If a carbon atom

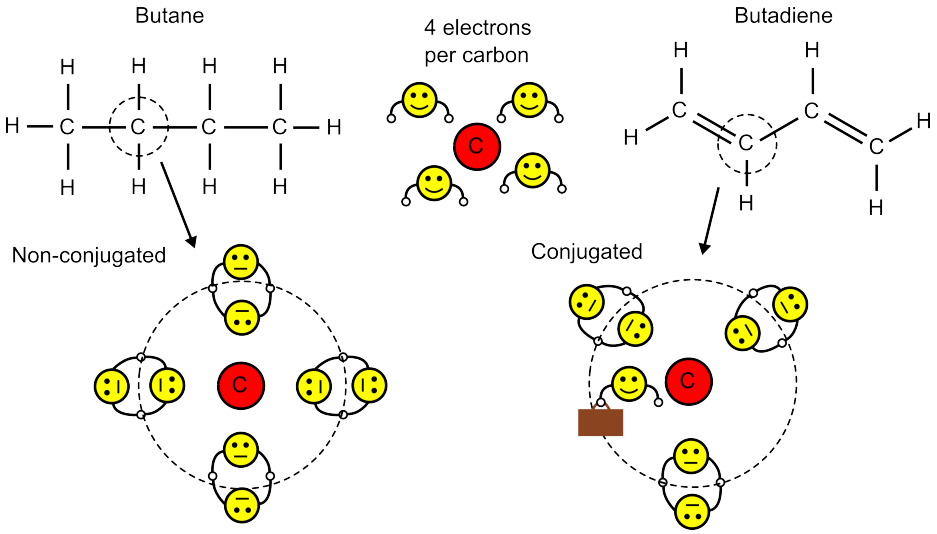

Figure 1.2: Conjugation in organic molecules. Left side: Butane is non-conjugated. The carbon atom bonds to four other atoms and thus all four electrons form σ-bonds. Right side: Butadiene is conjugated; each carbon atom bonds to three atoms and the fourth electron thus forms a π-bond.

has four neighbouring atoms as in butane (left side figure 1.2), all the four electrons of carbon will form σ-bonds. If a carbon atom has less then four atoms to bond to, it will form a double bond to a neighbouring atom, this second bond is called a π-bond. In Butadiene, a conjugated molecule, carbon only has three neighbouring atoms, resulting in the fourth electron to form a π-bond (right side figure 1.2). π-bonds are generally more diffuse then σ-bonds and make it possible for the electron to delocalize. The π-bonds and the delocalization of the electrons are at the basis of conjugation.

A fully conjugated molecule has electrons that are delocalized throughout the molecule. This significantly increases the conductivity of a molecule. It is possible to conjugate only certain areas of the molecule. This is shown in chapter 4 where at the center of a molecule the conjugation is "broken", influencing electron transport through the molecule. Furthermore in chapter 3 we show that by playing with the exact shape of the conjugated region of the molecule, it is possible to cancel out the movement of electrons and therefore make a conjugated molecule a bad conductor.

1.1.1. ORGANIC ELECTRONICS

Bulk conjugated-molecules can form organic electronic materials. These organic materials have desirable properties, like for example flexibility and relatively low fabrication cost. Furthermore with the knowledge from organic chemistry it is possible to build a wide variety of functionality in an organic material, as the number of different organic molecules is enormous. Applications of organic electronics can, at this mo-

ment, be seen in the wide spread use as light emitting diodes for screens in televisions and mobile phones. Research is also done on organic solar cells as this could result in flexible and low-cost solar panels.

Significant challenges remain to further utilize organic electronics in our society. Certain properties of a single molecule do not necessarily translate to the properties of bulk organic materials, as the interaction between the molecules also matters. Furthermore, due to the large variety of molecules that can be synthesized, finding the best molecule for a certain application remains a challenge. These questions and more are actively being researched in the field of organic electronics.

1.1.2. MOLECULAR ELECTRONICS

In this thesis we measure electron transport through single molecules instead of a bulk organic material. This research field is called molecular electronics and has, in general, two main goals. The first is to increase our understanding of electron transport through molecules. This can benefit the field of organic electronics, as the study of electron transport on the single-molecule scale can help to understand which molecules are useful in bulk organic materials. Furthermore, it also makes it possible to discern between transport phenomena that originate from the molecule itself and that originate from the collective action of the bulk material. This is demonstrated in chapter 6.

The second goal is the design and realization of single-molecule electronics. In semiconductor technology, the transistor (the basic building block of computers) has significantly decreased in size resulting in a few billion ($1 \cdot 10^9$) transistors on a single computer-chip. Each transistor measures only tens of nanometers in size. This makes it possible to build compact, powerful and energy efficient computers like for example our smart phones. However, semiconductor technology (silicon in particular) is reaching its limits for fabricating even smaller transistors. The properties of semiconductor materials arise from their crystal structure and to take advantage of this structure, thousands of atoms need to be present and thereby limiting further downscaling of semiconductor transistors. In molecules the functionality can be based on the structure of a single molecule, which is often only a nanometer long. This therefore makes single-molecule electronics a promising route in creating even smaller electronic devices than is possible at the moment.

1.2. HOW TO MEASURE A SINGLE MOLECULE?

Measuring the transport of electrons through a single molecule has only become possible with the advent of nanotechnology. However, the idea has already been proposed by Aviram en Ratner in 1974[3]. In the decades after that steps have been made into molecular electronics using thin molecular films[4]. This made it possible to measure current through many single molecules in parallel. The first single-molecule junction was measured in 1997[5]; since then many different molecules have been measured on the single molecule scale with a wide variety of techniques.

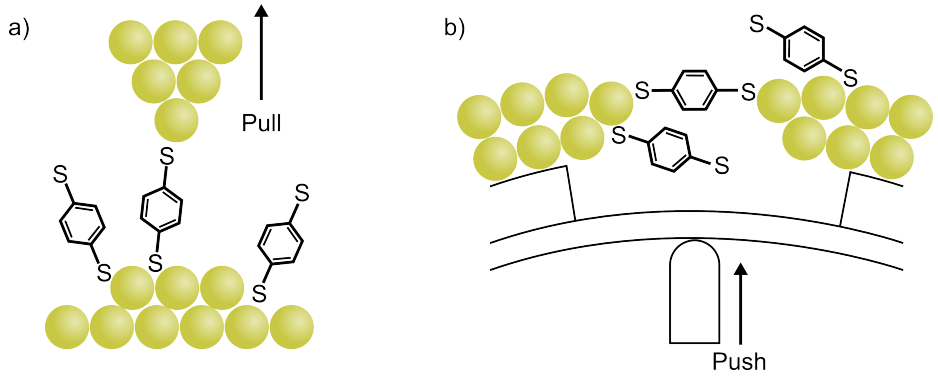

Figure 1.3: Schematic representation of the breakjunction techniques. a) In a STM breakjunction a metallic tip is pulled away from a metallic substrate to create a nanogap. b) In the MCBJ technique a metallic wire on top of a bendable substrate is broken by bending the substrate. Drawings not to scale.

The dominating experimental method is the break-junction technique. Here, a metallic wire is broken in such a way that a gap of nanometer size is created. This can be done using a scanning tunneling microscope (STM)[6] where the height of a metallic tip above a surface can be controlled. The tip is moved into the surface and then slowly retracted until a gap is formed which can be bridged by a single molecule (figure 1.3a). The setup is very sensitive, versatile and has the advantage that it can, at low temperature, image the surface beforehand to identify molecules. A drawback is that the sensitivity results in limited stability in junction formation at room temperature; not at low temperature. The STM-breakjunction technique has mostly been used to statistically identify the conductance of molecules[7] at room temperature.

Another method similar to the STM based technique is the mechanically controlled break-junction technique (MCBJ)[5] used in chapter 6. It works on the same principle as the STM-breakjunction (by pulling apart a metallic wire), however now the wire is on top of a substrate that can bend (figure 1.3b). The bending results in a stretching of the top surface of the substrate. If a suspended wire is placed on top of this surface it can potentially break and form a nano-gap. The advantage of the MCBJ technique is that it is more stable than the STM-breakjunction technique. The gap in the wire can thus be held at a precise distance, resulting in the possibility to form stable molecular junctions which at room temperature can last for minutes up to hours[8] and at cryogenic temperature up to weeks. The stability makes it possible to perform detailed investigation of transport properties both statistically[9] and one single molecule at a time[5]. It is also possible to include a gate electrode[10] to investigate transport as a function of Fermi-energy. The bendable substrate, however, makes it challenging. For measurements using a gate electrode the electromigration breakjunction technique described in the next subsection is more suitable.

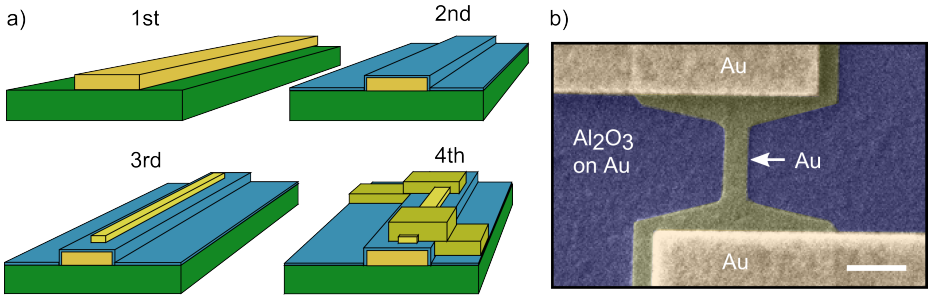

Figure 1.4: Fabrication steps and SEM image of an electromigration breakjunction. a) 1st step: Silicon (green) substrate with gate electrode (Au 70 nm) deposited on top. 2nd step: Covering of gate with ALD deposited Al_2O_3 (blue). 3rd step: Deposition of 12 nm thick gold nanowire (yellow). 4th step: Deposition of thick (110 nm) pads to contact the nanowire and wire-bonding pads. b) SEM image of an electromigration junction before electromigration. The white scale bar indicates 250nm.

1.2.1. ELECTROMIGRATION JUNCTION

The last method to be discussed here is the electromigrated-breakjunction technique. This technique is used in chapters 3, 4 and 5 and will therefore be described in some more detail. To form a nanogap, instead of pulling a wire apart, the metallic wire is electromigrated[11]. By applying a voltage over the wire, a current runs through it. Some of the conduction electrons will collide with the atoms forming the wire. When the momentum transfer from the conduction electrons to an atom is large enough, the atom will move[12]. If enough atoms are moved, a constriction may form and continuing this process results in breakage of the wire. By using a feedback controlled approach to electromigration[13], a gap in the gold wire can be formed controllably. Contrary to the STM and MCBJ approach it is not possible to close the gap again. This is the main limitation of the electromigration technique, making it difficult to build up statistics. This disadvantage is offset by the fact that no moving parts are present in the junction, making it significantly easier to study electron transport through a single molecule over a wide temperature range[14], in a magnetic field[15], and most importantly, in an electric field[16] applied by a gate electrode.

Figure 1.4a shows a schematic representation of the fabrication process of the electromigration junctions used in this thesis. In the first step a 70 nm thick gold gate-electrode is deposited on top of a silicon substrate. Subsequently a 5 nm thick layer of aluminum oxide dielectric is deposited on top of the gate electrode using atomic layer deposition (ALD). Some junctions in this thesis are fabricated with an older technique, where the gate-electrode is from aluminum which is then oxidized in a pure oxygen atmosphere. Both approaches result in a metallic gate electrode that has a few-nanometer thick dielectric around it. In the third step a 12 nm thick gold nanowire is deposited, which will later be electromigrated. As a final step the nanowire is contacted to bond pads with 110 nm thick gold patches. On a single substrate 24 junctions are fabricated in parallel. A scanning electron microscope (SEM)

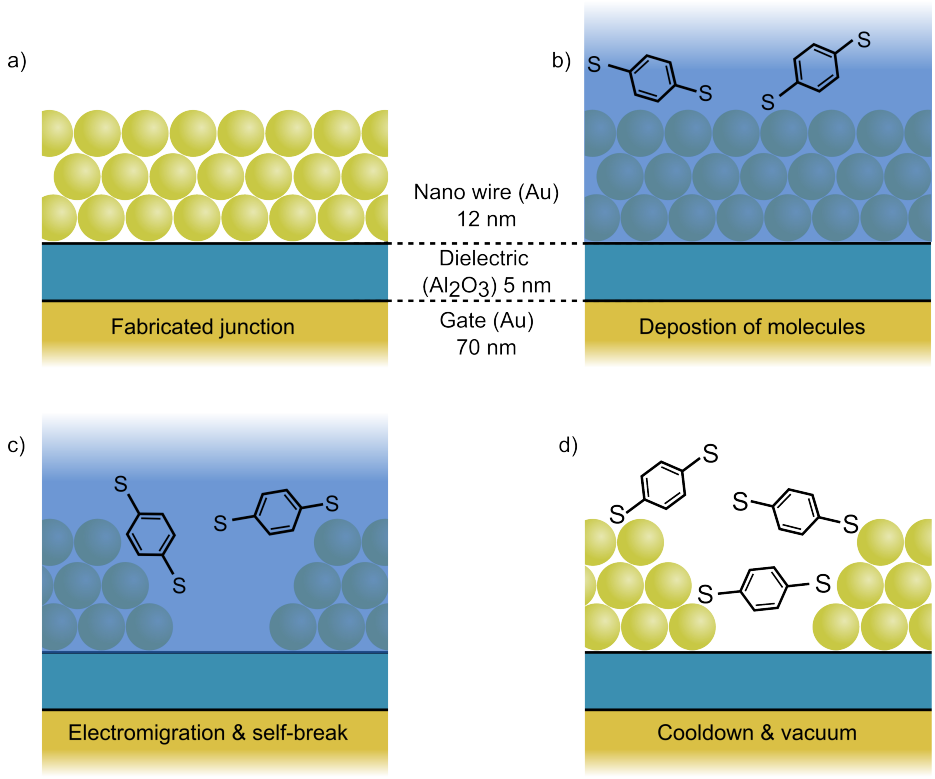

Figure 1.5: Steps in sample preparation for forming a single-molecule junction. Images are not drawn to scale. a) As fabricated gold nanowire on top of a gate with a dielectric in between. b) Solvent with molecules deposited on the junction. c) Electromigration and self-breaking is performed at room temperature and in solution. d) Solvent is evaporated by vacuum pumping and junction is cooled down.

image of a single junction is shown in figure 1.4b.

A description of the sample preparation after junction fabrication is shown in figure 1.5. A substrate with 24 junctions is ozone-cleaned to remove organic contaminants. After that a solution containing the molecules under investigation (concentration of molecules varies from 0.1 to 0.5 mM depending on the particular molecule) is deposited on the junctions (figure 1.5b). In the solution and at room temperature each of the 24 junction is electromigrated until a final resistance of 2 to 5 KΩ; after this the wire is let to self-brake[17] (figure 1.5c). After a waiting time ranging from 0.5 to 2 hours (depending on the resistance of the junctions) the sample chamber is evacuated to evaporate the remaining solvent and cooled down to cryogenic temperatures. Only at cryogenic temperatures the single-molecule junctions are stable enough to be investigated. Yields of successful electromigration are high (typically 95 %), however

the yield of single-molecule junction formation varies significantly, depending on the particular molecule and features investigated.

1.3. THESIS OUTLINE

Following this introduction there is a theory chapter on electron transport through single-molecule junctions. After this, in four chapters the experimental results will be discussed. These can be divided into two parts. The first three experimental chapters (chapters 3, 4 and 5) treat three structurally similar molecules consisting of an anthracene core functionalized with sulfur anchoring groups (figure 1.6a). The side groups of the carbon atoms at the 9 and 10 position of the anthracene core are varied in each chapter. In chapter 3 each carbon gets an oxygen atom; this results in cross-conjugation and destructive quantum interference in electron transport through the molecule. In chapter 4 the two carbon atoms have two hydrogens each, thereby breaking the conjugation and forming a double quantum dot in a single molecule. In chapter 5, the 9,10 positions are connected to 1,3-dithiole groups which can easily be oxidized. This results in localized orbitals and strong differential gating. All three molecules are experimentally investigated using the electromigration technique.

In the last experimental chapter (6) the influence of an azomethine bond on transport through molecules is investigated (figure 1.6b). This research is related to a newly developed process route to fabricate organic solar cells[18]. Using the MCBJ technique, we show that molecular electronics can be used as a tool to investigate processes that occur in organic electronics.

The last chapter (7) is an outlook. It discusses the opportunities and challenges of the single-molecule transport phenomena investigated in the experimental chapters. The gate electrode is identified as a limiting factor and alternatives are given. Furthermore, a proposal is discussed which combines quantum interference and a double quantum dot to detect single-electron tunneling events in a single molecule.

1

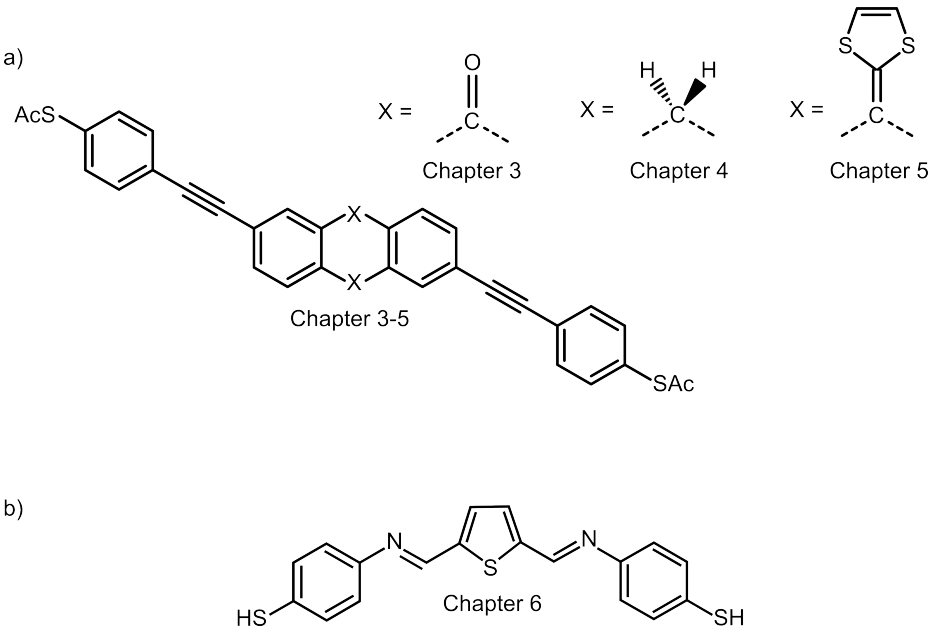

Figure 1.6: Molecules investigated in this thesis. a) An anthracene like core with acethyl (Ac) capped anchoring groups separated by spacers is used in chapter 3 to 5. In each chapter the groups attached at the carbon atoms located at X are varied. In chapter 3 an oxygen is connected to form anthraquinone. In chapter 4, two hydrogens are connected to form 9,10-dihydroanthracene. In chapter 5 two 1,3-dithiole groups are connected to form a π-extended tetrathiafulvalene. b) Azomethine based molecule investigated in chapter 6.

REFERENCES

[1] M. K. Wu, J. R. Ashburn, C. J. Torng, P. H. Hor, R. L. Meng, L. Gao, Z. J. Huang, Y. Q. Wang, and C. W. Chu, *Superconductivity at 93 K in a new mixed-phase Y-Ba-Cu-O compound system at ambient pressure,* Phys. Rev. Lett. **58**, 908 (1987).

[2] K. S. Novoselov, A. K. Geim, S. V. Morozov, D. Jiang, Y. Zhang, S. V. Dubonos, I. V. Grigorieva, and A. A. Firsov, *Electric field effect in atomically thin carbon films,* Science **306**, 666 (2004).

[3] A. Aviram and M. A. Ratner, *Molecular rectifiers,* Chem. Phys. Lett. **29**, 277 (1974).

[4] B. Mann and H. Kuhn, *Tunneling through fatty acid salt monolayers,* J. Appl. Phys. **42**, 4398 (1971).

[5] M. A. Reed, C. Zhou, C. J. Muller, T. P. Burgin, and J. M. Tour, *Conductance of a molecular junction,* Science **278**, 252 (1997).

[6] C. Joachim, J. K. Gimzewski, R. R. Schlittler, and C. Chavy, *Electronic transparence of a single C_{60} molecule,* Phys. Rev. Lett. **74**, 2102 (1995).

[7] B. Xu and N. J. Tao, *Measurement of single-molecule resistance by repeated formation of molecular junctions,* Science **301**, 1221 (2003).

[8] R. Frisenda, S. Tarkuç, E. Galán, M. L. Perrin, R. Eelkema, F. C. Grozema, and H. S. J. van der Zant, *Electrical properties and mechanical stability of anchoring groups for single-molecule electronics,* Beilstein J. Nano. **6**, 1558 (2015).

[9] M. T. González, S. Wu, R. Huber, S. J. van der Molen, C. Schonenberger, and M. Calame, *Electrical conductance of molecular junctions by a robust statistical analysis,* Nano Lett. **6**, 2238 (2006).

[10] A. R. Champagne, A. N. Pasupathy, and D. C. Ralph, *Mechanically adjustable and electrically gated single-molecule transistors,* Nano Lett. **5**, 305 (2005).

[11] H. Park, A. K. L. Lim, A. P. Alivisatos, J. Park, and P. L. McEuen, *Fabrication of metallic electrodes with nanometer separation by electromigration,* Appl. Phys. Lett. **75**, 301 (1999).

[12] P. S. Ho and T. Kwok, *Electromigration in metals,* Rep. Prog. Phys. **52**, 301 (1989).

[13] D. R. Strachan, D. E. Smith, D. E. Johnston, T.-H. Park, M. J. Therien, D. A. Bonnell, and A. T. Johnson, *Controlled fabrication of nanogaps in ambient environment for molecular electronics,* Appl. Phys. Lett. **86**, 043109 (2005).

[14] M. Poot, E. Osorio, K. O'Neill, J. M. Thijssen, D. Vanmaekelbergh, C. A. van Walree, L. W. Jenneskens, and H. S. J. van der Zant, *Temperature dependence of three-terminal molecular junctions with sulfur end-functionalized tercyclohexylidenes,* Nano Lett. **6**, 1031 (2006).

[15] J. Park, A. N. Pasupathy, J. I. Goldsmith, C. Chang, Y. Yaish, J. R. Petta, M. Rinkoski, J. P. Sethna, H. D. Abruna, P. L. McEuen, and D. C. Ralph, *Coulomb blockade and the Kondo effect in single-atom transistors,* Nature **417**, 722 (2002).

[16] H. Park, J. Park, A. K. L. Lim, E. H. Anderson, A. P. Alivisatos, and P. L. McEuen, *Nanomechanical oscillations in a single-C_{60} transistor,* Nature **407**, 57 (2000).

[17] K. O'Neill, E. A. Osorio, and H. S. J. van der Zant, *Self-breaking in planar few-atom Au constrictions for nanometer-spaced electrodes,* Appl. Phys. Lett. **90**, 133109 (2007).

[18] M. L. Petrus, R. K. M. Bouwer, U. Lafont, S. Athanasopoulos, N. C. Greenham, and T. J. Dingemans, *Small-molecule azomethines: organic photovoltaics via Schiff base condensation chemistry,* J. Mater. Chem. A **2**, 9474 (2014).

2

THEORY

In this chapter we introduce the theory of charge transport through single molecules coupled to electrodes. We start with a general discussion of different types of charge transport through nanostructures. We find that to describe charge transport occurring in the experimental chapters of this thesis, a fully coherent quantum-mechanical approach should be used. Therefore, non-equilibrium Green's function theory is discussed and applied to simple model systems. To understand the basic features of three-terminal transport the constant interaction model is explained and some features arising from Kondo correlations are discussed.

In this chapter we will discuss the theory that is relevant to understand transport through molecules bridging gold electrodes. In general, the theory that will be described here, is applicable to coherent transport through structures of nanometer dimension. This chapter has been based on multiple sources[1–7].

A simple schematic of a charge-transport measurement through a nanostructure between two electrodes is shown in figure 2.1. In grey the electrodes and in black the nanostructure are drawn; in the latter the influence of its small size has a determining effect on transport of electrons through it. The left electrode is connected to a voltage source and therefore a bias potential can be applied across the nanostructure. Through the right electrode current can flow via an ammeter to ground. This simple two-terminal setup makes it possible to measure the current (I) through the nanostructure as a function of applied voltage (V). We use the flow of electrons as a probe to explore the physics in these nanostructures.

2.1. TRANSPORT REGIMES

The size of the nanostructure and how it is connected to the electrodes are important factors in determining which features will appear in charge transport through it and the theory needed to understand them.

2.1.1. SIZE

The type of transport through a nanostructure can be subdivided according to a set of length scales related to the conduction electrons (the electrons that participate in transport). These are: the mean free path (l), phase coherence length (l_ϕ) and the Fermi wavelength (λ_F) of the conduction electrons. Electron transport through a

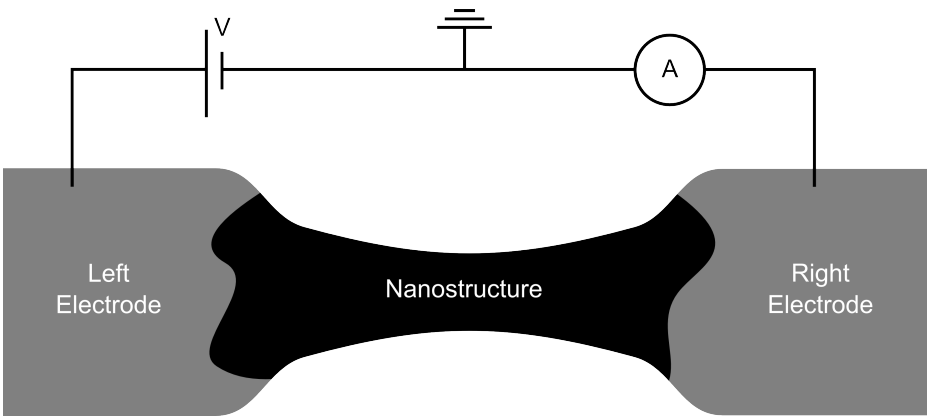

Figure 2.1: Sketch of a two-terminal charge-transport measurement through a nanostructure. The nanostructure is connected to a left electrode onto which a bias voltage (V) is applied. On the other side is the right electrode which is connected via an ammeter to ground.

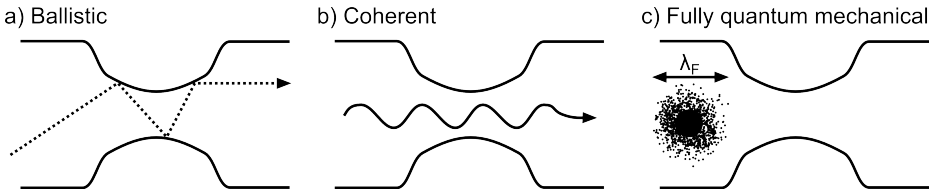

Figure 2.2: Three different length scales in electron transport. a) Dimension of the nanostructure is smaller than the mean free path. Electrons move ballistically through the structure. b) Nanostructure is smaller than the coherence length of the conduction electrons. No dephasing happens to the electrons when traversing the nanostructure; transport is therefore coherent. c) Nanostructure is of the size of the Fermi-wavelength so that quantum mechanical effects dominate transport.

structure with dimensions larger than these three length scales can, to a good approximation, be described using the Drude model[8] leading to the well known Ohms law for the resistance.

Shrinking the nanostructure to a size smaller than the mean free path or phase coherence length results in respectively ballistic (figure 2.2a) or coherent (figure 2.2b) electron transport. The Drude model will fail and quantum mechanical effects have to be taken into account. For ballistic transport the path of the conduction electrons becomes important, due to the absence of scattering centers. This leads to conductance quantization[9]. For coherent transport the phase of the electron becomes important, leading to constructive and destructive interference of electrons in transport as in the Aharonov-Bohm rings[10]. Note that both ballistic and coherent transport at the same time is also possible. Scaling down the nanostructure even further, smaller than the Fermi wavelength of the conduction electrons (figure 2.2c), quantum mechanical effects become significant in transport. The size of the nanostructure is of the same order or smaller than the size of the wave-function of the conduction electrons.

In this thesis we investigate transport through single molecules connected to gold electrodes. The length scales of the conduction electrons in gold are at low temperatures, $l = 10 \sim 100$ nm, $l_\phi = 1 \sim 10$ µm and $\lambda_F = 0.5$ nm. The smallest region of our junction is the molecule itself (~ 1 nm or smaller) and the last few gold atoms of the molecule-gold contact region (size of a gold atom ~ 150 pm). These sizes are much smaller than the coherence length and mean free path. It is even smaller or on par with the Fermi wavelength and therefore it is necessary to use a fully quantum mechanical treatment of electron transport through molecules in between gold electrodes.

2.1.2. COUPLING

The electrode coupling (Γ) is the rate at which electrons transfer from the electrodes to the nanostructure or vice versa. This can also be seen as the degree of interaction a nanostructure has via electrons with the electrodes. If the coupling is small,

electrons will hop on and off relatively infrequently and will therefore have a rather long residence-time on the nanostructure. A large coupling implies many electrons hopping on and off; an individual electron will only spend a short time on the nanostructure.

The time ($\tau \approx \hbar/\Gamma$) a conduction electron spends on the nanostructure when going from one electrode to the other, is essential to determine the interactions it experiences. Two important interactions are the electron-electron interaction characterized by the coulomb repulsion energy (U_{e-e}) and the electron-phonon interaction(λ_{e-ph}). If $\Gamma \gg U_{e-e}, \lambda_{e-ph}$ the time an electron spends traversing the nanostructure is much shorter than the time it takes to interact with other electrons or vibrations. If this is the case, then the nanostructure is in the strong coupling regime and electrons preserve their phase while moving through it.

On the other hand, when $\Gamma \ll U_{e-e}, \lambda_{e-ph}$, the conduction electrons have ample time to interact with the nanostructure. In this case, the structure is weakly coupled and the interactions will result in dephasing; this is the incoherent transport regime. Clearly, a nanostructure can also be in between the two regimes, which is called the intermediate coupling regime.

In this thesis transport through small (nanometer-sized) molecules is studied. This necessitates a full quantum mechanical treatment of electron transport. Two often used starting points for this are the non-equilibrium Green's function (NEGF) scattering approach and the master equation approach. The master equation approach is based on incoherent transport, making it possible to treat strong interactions in the nanostructure. The NEGF scattering approach, in its simplest form, neglects interactions, so coherent transport can be described.

As we will see in the experimental chapters, the molecular junctions studied in this thesis are in the intermediate to strong coupling regime. This motivates the use of the NEGF approach to describe transport through our junctions. Furthermore, as the experiments are performed at cryogenic temperatures and the coupling is strong ($\Gamma > k_b T$), temperature is assumed to play a negligible role in transport. In the following sections we will discuss the NEGF scattering approach for coherent quantum mechanical transport through single molecules.

2.2. NON-EQUILIBRIUM GREEN'S FUNCTIONS APPROACH

A practical starting point to discuss NEGF is the closely related Landauer scattering approach. From there we will go into the NEGF approach. This will then be applied to a single site and a two-site model connected to electrodes, resulting in basic features in transport which are also observed in experimental transport through single molecules.

2.2.1. LANDAUER SCATTERING APPROACH

One of the main assumptions in the Landauer scattering approach is that all the complex interactions in the electrodes can be captured in a set of boundary conditions.

We can treat electrons in the electrodes as coherent electron waves that have an energy dependent probability $T(E)$ to be transmitted though the molecule and appear in the other electrode. If only one electron at a time is allowed to pass (which in nanostructures of the scale of the Fermi-wavelength is often the case), the current is given by the Landauer formula:

$$I(V) = \frac{2e}{h} \int_{-\infty}^{\infty} T(E)[f_L(E) - f_R(E)]\,\mathrm{d}E. \tag{2.1}$$

Here, e is the charge of an electron, h is Planck's constant, $f_{L,R}$ the occupation of the density of states of the left (L) or right (R) electrode and $T(E)$ the transmission of the molecule. The description of the electrodes is now condensed into a pair of ideal electron reservoirs at equilibrium and populated according to the Fermi function (equation 2.2). This describes the filling of an electron state with energy E as a function of temperature T (k_b is the Boltzmann constant) and chemical potential μ:

$$f(E) = \frac{1}{\mathrm{e}^{\frac{E-\mu}{k_b T}} + 1}. \tag{2.2}$$

The electron occupation in both the left and right electrode matters, as an electron can only move from one electrode to the other when a filled state is present in the first and an empty state is present in the latter.

It is interesting to note that when the temperature is zero the low-bias current reduces to $I = GV$ with $G = (2e^2/h)T(E)$. A fully transmitting channel ($T(E) = 1$) therefore has a low-bias conductance (dI/dV) of $G_0 = 2e^2/h = 77\ \mu\mathrm{S}$.

The problem of determining the current through a molecule connected to metallic electrodes has thus been narrowed down to calculating the transmission through the molecule itself. The Landauer approach does not give a recipe for how to do this. To calculate the transmission through a molecule we turn to the non-equilibrium Green's functions approach described in the next section.

2.2.2. NON-EQUILIBRIUM GREEN'S FUNCTION APPROACH

The following section introduces the NEGF approach to derive an expression for the transmission that appears in the Landauer scattering approach. This section will not be mathematically rigorous as many steps in the derivation will be skipped. For a full derivation see for example Cuevas and Scheer [1].

In the previous section we have divided the junction into a pair of electron reservoirs and a molecule which connects the electron reservoirs. We will keep this distinction but add a hopping between the three regions so that the structure of the Hamiltonian of the full system can be written as:

$$H = \begin{bmatrix} H_L & t_{LM} & 0 \\ t_{ML} & H_M & t_{MR} \\ 0 & t_{RM} & H_R \end{bmatrix}. \tag{2.3}$$

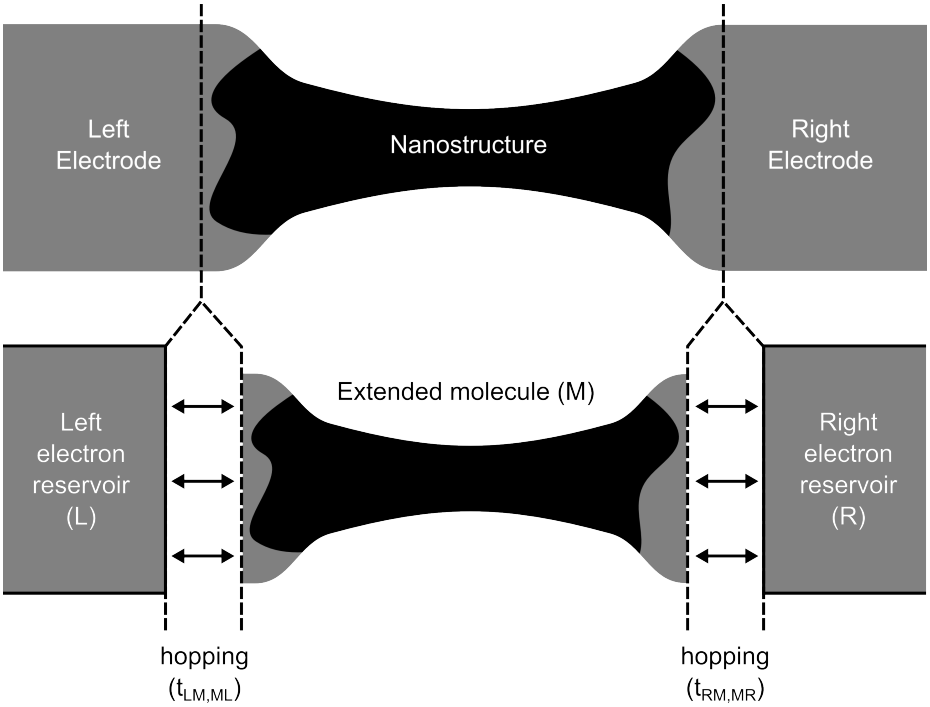

Figure 2.3: The sketch of figure 2.1 can be divided into different regions labeled left electrode (L), extended molecule (M) and right electrode (R) connected by a hopping parameter t. Note that parts of the electrodes where quantum mechanical effects start to dominate are now included in the extended molecule.

Here, the Hamiltonians labeled L, M and R are respectively the left electrode, the molecule and the right electrode. The hopping parameter t (taken to be real) describes the hopping between the distinct regions, with the subscript indicating the hopping direction (LM thus means a hop from the left electrode to the molecule and reversed for ML). The same applies for the R label but then for the right electrode. Note, that no hopping is assumed between the source and drain electrode directly. In realistic junctions this may not always be the case.

The labeling and structure is shown graphically in figure 2.3. The exact division of the three regions is determined by how close to the molecule the electrodes behave as ideal electron reservoirs. For molecular electronics it would seem a natural choice to make the division at where the metallic electrodes contact the molecule. However, the last few layers of the metal electrodes are often not in an equilibrium state and small enough in size so that significant quantum mechanical effects appear. Therefore, the last few layers of metal atoms are added to the molecule region. It is then renamed as the extended molecule, as shown in the lower part of figure 2.3.

For the derivation of the transmission we begin with an expression of the current

through the junction. At the interface between the left electrode and the extended molecule we get (assuming no dependence on spin):

$$I = i\frac{2e}{\hbar}\sum_{i\in L; j\in M}(t_{i,j}\langle c_i^\dagger c_j\rangle - t_{j,i}\langle c_j^\dagger c_i\rangle). \tag{2.4}$$

This corresponds to counting all electrons which hop from the extended molecule to the left electrode minus all electrons which hop from the left electrode to the extended molecule. The expectation of the hopping operator $\langle c_i^\dagger c_j\rangle$ can be rewritten as $G^<_{i,j}(t,t) = i\langle c_i^\dagger(t)c_j(t)\rangle$. Here, we introduce the lesser Green's function from the non-equilibrium Green's functions theory. As $t_{LM} = t_{ML}$ we can also change to a matrix notation (bold font) instead of the individual elements. This results in equation 2.4 to be rewritten as equation 2.5, which introduces the Green's functions into the expression for the current:

$$I = \frac{2e}{\hbar}\mathrm{Tr}[\boldsymbol{G}^<_{ML}(t,t)\boldsymbol{t}_{LM} - \boldsymbol{t}_{ML}\boldsymbol{G}^<_{LM}(t,t)]. \tag{2.5}$$

In steady state one can Fourier transform this expression to go from the time-domain to the energy-domain resulting in the following equation:

$$I = \frac{2e}{h}\int_{-\infty}^{\infty}\mathrm{Tr}[\boldsymbol{G}^<_{ML}(E)\boldsymbol{t}_{LM} - \boldsymbol{t}_{ML}\boldsymbol{G}^<_{LM}(E)]\,\mathrm{d}E. \tag{2.6}$$

At this point a complex series of rearrangements and substitutions is needed, where the full machinery of the non-equilibrium Green's functions theory is used. One important substitution to note is the following: $\boldsymbol{\Gamma}_L = 2\mathrm{Im}\{\boldsymbol{t}_{ML}\boldsymbol{g}_L\boldsymbol{t}_{LM}\}$ (and the same for the R index), which relates the coupling of the extended molecule to the electrodes as the product of the hopping (t) squared and the density of states of the electrode ($\mathrm{Im}\{g_L\}$). The equation that results is:

$$I = \frac{2e}{h}\int_{-\infty}^{\infty}\mathrm{Tr}[\boldsymbol{\Gamma}_L\boldsymbol{G}^r_M\boldsymbol{\Gamma}_R\boldsymbol{G}^a_M](f_L - f_R)\,\mathrm{d}E. \tag{2.7}$$

A comparison with equation 2.1 shows that the expression for the transmission of the extended molecule in the non-equilibrium Green's function approach is:

$$T(E,V) = \mathrm{Tr}[\boldsymbol{\Gamma}_L\boldsymbol{G}^r_M\boldsymbol{\Gamma}_R\boldsymbol{G}^a_M]. \tag{2.8}$$

The transmission can be expressed as the trace of the matrix product of the coupling of the extended molecule to the left electrode ($\boldsymbol{\Gamma}_L$), the retarded Green's function of the extended molecule ($\boldsymbol{G}^r_M$), the coupling to the right electrode ($\boldsymbol{\Gamma}_R$) and the advanced Green's function of the extended molecule ($\boldsymbol{G}^a_M$).

There are multiple approaches to calculate the Green's function for a system. Here we make use of the Dyson equation:

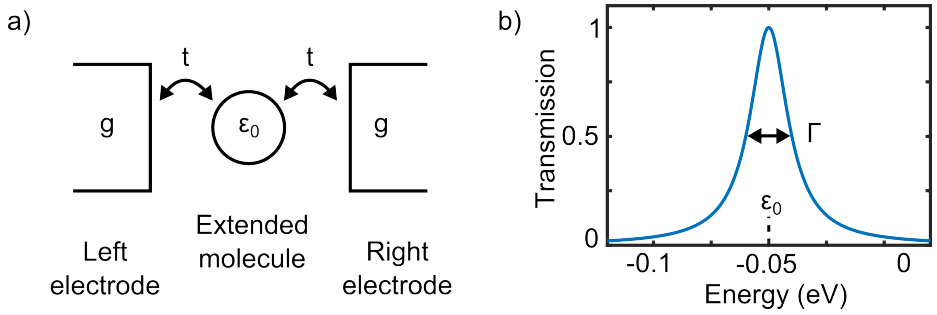

Figure 2.4: Transport through a single level with parameters $\epsilon_0 = -0.05$, $t = \sqrt{0.005}$, $T = 0$ K and $g = i$. a) Schematic of the extended molecule and the electrodes connecting it. b) Transmission calculated with equation 2.8. A single Lorentzian function is centered at ϵ_0.

$$\boldsymbol{G}_M^a = (\boldsymbol{G}_M^r)^\dagger = \frac{1}{(\boldsymbol{E} - i0^+)\mathbf{1} - \boldsymbol{H}_M - \sum_L - \sum_R}, \tag{2.9}$$

where the Hamiltonian of the extended molecule ($\boldsymbol{H}_M$) for the first time appears. Furthermore the two terms $\sum_L$ and $\sum_R$ are the self-energies. They describe the interaction of the extended molecule with the left and right electrodes, and can be derived to be of the form $\sum_L = \boldsymbol{t}_{ML}\boldsymbol{g}_L\boldsymbol{t}_{LM}$ (the same for index R), where $\boldsymbol{g}_{L,R}$ is the Green's function of the electrode without interactions with the molecule.

2.2.3. SINGLE- AND TWO-SITE MODEL

In this subsection, we apply the NEGF approach to simple model-systems to get an idea of the transport phenomena we can expect coherent quantum-mechanical transport through molecules. To simplify the calculations, the wide-band limit is assumed for the electrodes and it is assumed that the electrodes are identical. This means that the Green's function of the electrodes is a complex constant. When we also assume that the hopping (t) from the molecule to the left electrode and from the molecule to the right electrode is identical, the self-energies of the extended molecule reduce to $\sum_{L,R} = itgt = i\Gamma/4$, with $\Gamma_L = \Gamma_R = \Gamma/2$.

The first model system, shown in figure 2.4, is a single site (a single electron state) in between two electrodes. Panel a) shows a schematic of the system. The two electrodes are fully defined by their Green's function (g) and connected to an electron state at energy ϵ_0 with hopping parameter t. Using equation 2.8 and 2.9, the resulting transmission can be calculated and is shown in panel b). The transmission of this simple system also has an analytical solution, given by:

$$T(E) = \frac{(\Gamma/2)^2}{(E - \epsilon_0)^2 + (\Gamma/2)^2}. \tag{2.10}$$

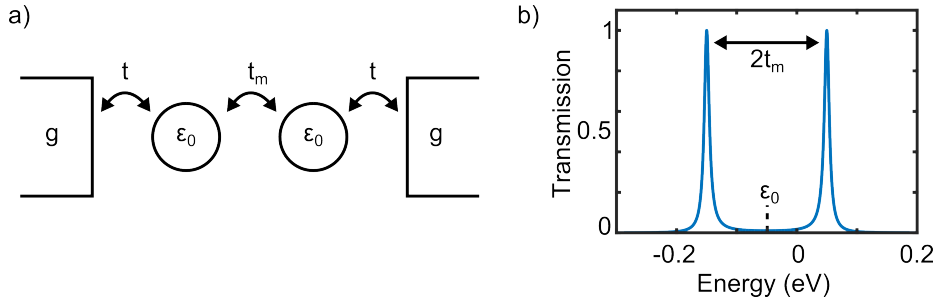

Figure 2.5: Transport through two sites with parameters $\epsilon_0 = -0.05$, $t = \sqrt{0.005}$, $t_m = 0.1$, $T = 0$ K and $g = i$. a) Schematic of the system. b) Calculated transmission as a function of energy. Two Lorentzian broadened resonances appear, centered around ϵ_0 and $2t_m$ apart.

The transmission through a single electron state forms a Lorentzian shaped resonance at the energy of the electron state. The full width at half maximum of the Lorentzian is given by $\Gamma = 4t^2 g$, showing that the transmission of the electron state is broadened by the interaction (coupling) with the electrodes. Charge transport is now not only possible at ϵ_0 but also a few units of Γ away from ϵ_0. Irrespective of the magnitude of the coupling the transmission maximum is one.

This model can be expanded by adding a second site with the same energy in series to it (figure 2.5). Each site is coupled to its closest electrode with hopping parameter t. The two sites are coupled through a hopping parameter t_m. The resulting transmission in panel b) shows two broadened resonances spaced $2t_m$ apart and centered around ϵ_0. The coupling of the two sites, of the same energy, therefore creates two resonances at different energies. Analogous to the hydrogen molecule, the coupling of the two sites creates a bonding (lower energy) and an anti-bonding (higher energy) orbital. Extending the system with more sites would result in a set of orbitals on the molecule leading to a set of transmission resonances in transport.

How individual resonances interact with each other, is determined by the exact arrangement of the sites and couplings. Figure 2.6 essentially shows the same model as in figure 2.5, with the only difference being the location of the coupling to the electrodes. As seen in panel a), one site is coupled to both electrodes and the other is only coupled to the first site. Again as in the series arrangement, two resonances appear due to the inter coupling, centered around ϵ_0 and $2t_m$ apart from each other. However, zooming in on the transmission in panel c) and d), it can be seen that in this case the transmission in between the resonances is lower (blue) than in the serially arranged case (orange). This is caused by destructive interference of electron transport. The phase an electron acquires when passing through a resonance, is different for each resonance. Therefore, the electron interferes destructively with itself. Small changes in the exact molecular structure can therefore have a large impact on electron transport in the coherent quantum regime.

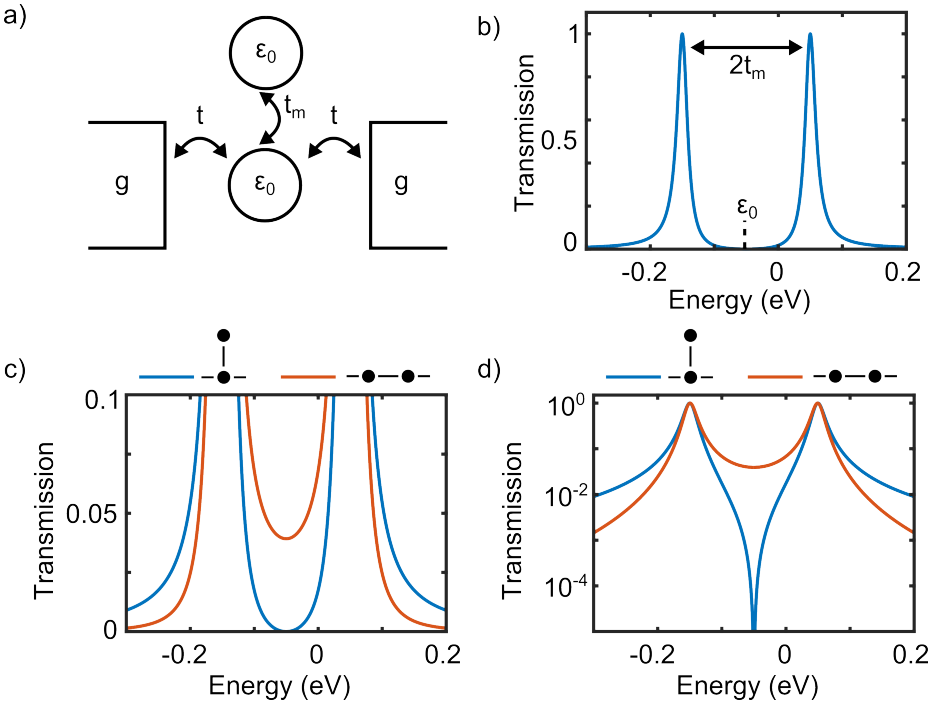

Figure 2.6: Transport through two sites with parameters $\epsilon_0 = -0.05$, $t = \sqrt{0.005}$, $t_m = 0.1$, $T = 0$ K and $g = i$. a) Schematic of the system. Now one site is coupled to both electrodes (t) and the second site is only coupled to the first (t_m). b) Calculated transmission function. Two Lorenztian broadened resonances appear, centered around ϵ_0 and $2t_m$ apart. c) Plot of both the perpendicular (blue) and series (orange) two-site configuration (shown in figure 2.5) zoomed in at low transmission. d) Again both two-site models, but now on a logarithmic scale. The perpendicular model has a pronounced dip in its transmission at ϵ_0.

From the three models discussed above we have seen the demonstration of broadening of electron states into transport resonances due to the coupling to the electrodes. The appearance of resonances at different energies arising from internal coupling of multiple sites and the constructive or destructive interference of resonances depending on the exact arrangement of the sites with respect to each other and the electrodes. As we will see in the coming experimental chapters, these transport features can be experimentally observed in electron transport through single molecules. This can be intuitively understood by taking as a crude model for the molecule and apex atoms of the electrodes, a network of interconnected sites at different energies. The resulting transport resonances will be broadened and separated from each other in energy. Furthermore, small changes in the structure can result in a large change in the transmission due to interference between the resonances.

It is important to note that the NEGF formalism in its simplest form shown here,

treats transport of electrons effectively as a single-particle problem. Contributions from phonon and electron-electron interactions are neglected, which for quantitative agreement with experiments should be included. Furthermore, the calculation of the Hamiltonian of the molecule or extended molecule (molecule and apex gold atoms), is an entire research field in itself. Here, we have used a very basic tight-binding model, which can be extended with for example electron-electron interactions (see chapter 3). Another often used approach is to calculate the Hamiltonian using density functional theory, which has the advantage that it starts from the actual atomic geometry of the system and takes electron-electron interaction into account.

2.3. THREE-TERMINAL TRANSPORT

In this section we will discuss features arising in three-terminal transport. In addition to what was previously discussed for two-terminal measurements, now a third electrode (gate) is added with which the electric potential of the molecule can be modified independently from the potentials of the electrodes contacting the molecule. This makes it possible to change the energy of the molecule with respect to the Fermi energy of the transport electrodes and map out transport features as a function of energy.

2.3.1. CONSTANT INTERACTION MODEL

A basic approach to describe three-terminal transport in molecules is the constant interaction model. The main assumption of this model is that the electric potential of the gate electrode shifts all orbitals of the molecule by the same amount and that the energy of the orbitals is independent of the number of electrons on the molecule. This is often not the case in molecular junctions, however, the model is still a useful starting point to extract quantitative information from the experimental measurements.

We consider a molecule with multiple orbitals, for example the two-site model of figure 2.5 but then extended to multiple sites. The electric potential on the molecule (V_m) is the sum of the net charge residing on the molecule $Q = -eN$ and the contribution from an external potential V_{ext}:

$$V_m = Q/C + V_{ext}, \tag{2.11}$$

where C is the sum of the capacitances ($C = C_L + C_R + C_g$) of the molecule with the left electrode (L), right electrode (R) and gate (g). The contribution from the external potential can be expressed as $V_{ext} = (C_L V_L + C_R V_R + C_g V_g)/C$. The total energy of the electrons on molecule is then given by:

$$U(N) = U_{ES}(N) + \sum_{p=1}^{N} \epsilon_p \text{ , where } U_{ES}(N) = \int_0^{-eN} V_m(Q)\,\mathrm{d}Q = \frac{(Ne)^2}{2C} - NeV_{ext}, \tag{2.12}$$

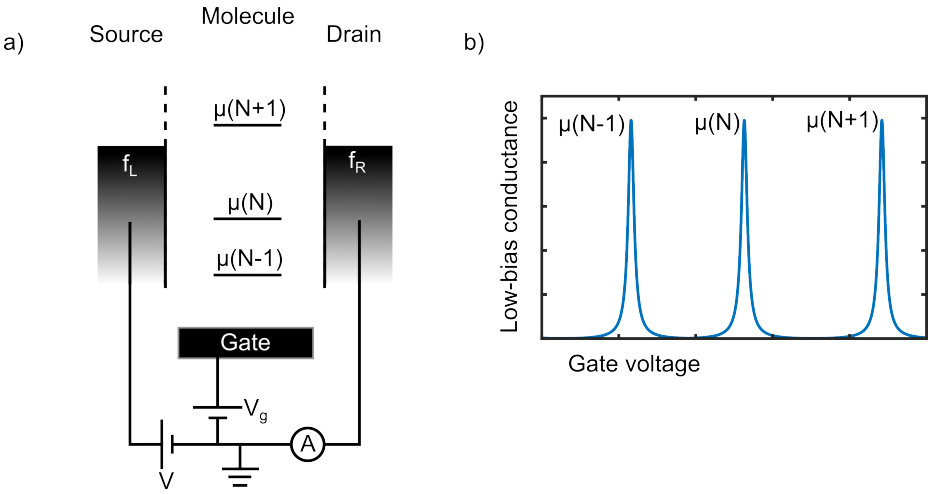

Figure 2.7: Three-terminal transport. a) Schematic of a three-terminal junction. The left and right electrodes are populated according to the Fermi distribution. The location of the chemical potential of the molecule is given by equation 2.13. b) Conductance peaks as a function of the gate voltage when μ is aligned with the Fermi energy of the electrodes.

where ϵ_p is the energy of orbital p on the molecule. The total energy of the electrons on the molecule consists of an electrostatic (U_{ES}) and a quantum mechanical ($\sum_{p=1}^{N}\epsilon_p$) contribution. The chemical potential is the change in energy when an electron is added to or removed from the system ($\mathrm{d}U/\mathrm{d}N$). It is essential in determining whether electrons can move through the molecule. The chemical potential of the molecule (μ) with a certain number of electrons (N) is given by:

$$\mu(N) = U(N) - U(N-1) = (N - \frac{1}{2})\frac{e^2}{C} - eV_{ext} + \epsilon_N. \tag{2.13}$$

A schematic of the chemical potentials of the molecule and the leads is shown in figure 2.7a. The chemical potentials of the left and right electrode are given by the Fermi distribution and can be shifted with respect to each other by applying a bias voltage. Current is measured at the right electrode and with another voltage source a gate voltage (V_g) can be applied to the gate electrode near the molecule to shift its chemical potentials.

When a molecular chemical potential is aligned with the left and right electrode, the low-bias conductance of the junction increases. While sweeping the gate voltage over a wider range a series of peaks (panel b) appears in the low-bias conductance. Each peak is for a chemical potential of the molecule aligning with the left and right electrode's chemical potentials. The distance between two consecutive peaks is the addition energy, $\Delta E(N)$, defined in equation 2.14.

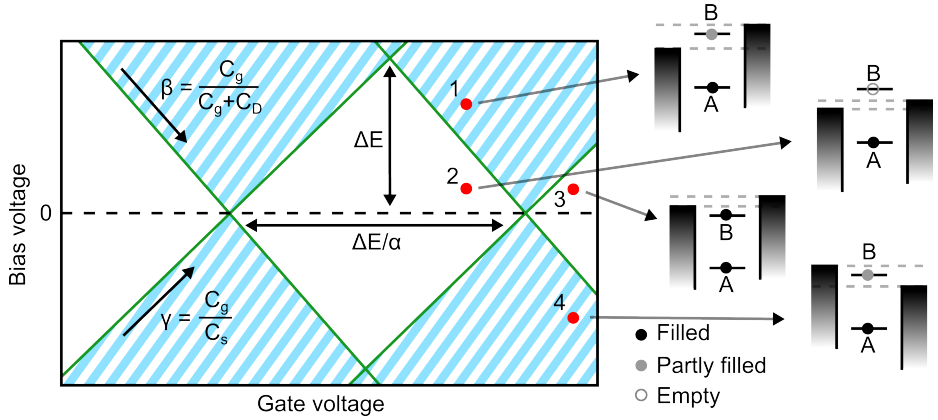

Figure 2.8: Differential conductance as a function of bias and gate voltage. A diamond like pattern is present with regions of off-resonant (white) and on-resonant (blue shaded area) transport. Note that in the blue shaded area the differential conductance is still of the same order as in the white area. A change of differential conductance is only observed at the green lines. The red dots show the locations of the selected configurations shown to the right of the differential conductance map.

$$\Delta E(N) = \mu(N+1) - \mu(N) = \frac{e^2}{C} + \epsilon_{N+1} - \epsilon_N. \tag{2.14}$$

It has an electrostatic contribution of the form $\frac{e^2}{C}$ and a quantum mechanical level spacing of $\epsilon_{N+1} - \epsilon_N$. The exact shape of the peaks was discussed in the previous section on non-equilibrium Green's function approach.

Measuring the differential conductance $\mathrm{d}I/\mathrm{d}V$ (this highlights features in transport better than when presenting the current) as a function of bias and gate voltage results in a diamond-like pattern as shown in figure 2.8. The green lines are the peaks in the differential conductance when a chemical potential enters the bias window defined by ($eV = \mu_L - \mu_R$), where μ_i is the chemical potential of the ith electrode. When there is no molecular chemical potential in the bias window, transport is off-resonant (white area). When the bias is increased or the gate shifts a chemical potential into the bias window, transport is on-resonant (blue shaded area). At zero-bias (dashed line) there are two points at which the green lines cross. These are the charge degeneracy points and correspond to the peaks in the low-bias differential conductance of figure 2.7b. The two degeneracy points are a certain gate voltage apart from each other which matches $V_g = \Delta E/\alpha$, where $\alpha = C_G/C$ the gate coupling; the potential felt by the molecule compared with the potential at the gate electrode. α can be estimated using two equivalent approaches. The first uses the slopes of the diamond edges: $1/\alpha = 1/\beta + 1/\gamma$, where β is the slope of the descending diamond edge and γ of the ascending edge. The second is the ratio of the height of the diamond ΔE, compared to its width $\Delta E/\alpha$.

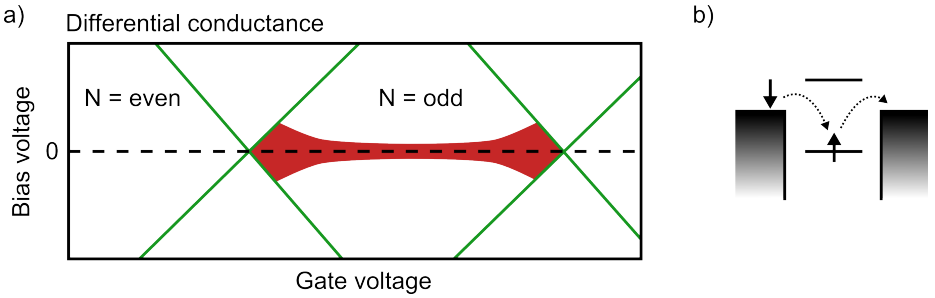

Figure 2.9: Kondo effect from a single electron spin. a) A peak in the differential conductance develops at zero-bias in the odd charge state. b) With a spin flip process an electron is transferred from the left to the right electrode.

At the right hand side of the differential conductance map, the chemical potentials are drawn for four configurations marked by the red dots. Starting from the top most dot (configuration 1), the top most chemical potential is in the bias window depicted by the region in between the dashed gray lines. Transport is resonant and electrons can move from the right to the left electrode. Moving down in the differential conductance map towards configuration 2, the bias voltage is lowered and the chemical potential now falls outside of the bias window. Transport is off-resonant and the top most state (open circle) is empty. By increasing the gate voltage, the top most state can be moved below the chemical potential of the electrodes and an electron is added to the molecule. This corresponds to configuration 3. From configuration 3 to 4 the bias voltage is reversed: the top most state falls into the bias window and transport is resonant again. However, now the electrons move from the left electrode to the right.

2.4. KONDO CORRELATIONS

When there is an odd number of electrons on the molecule, Kondo correlations can become important. This will show up as a peak in the differential conductance at zero bias in the off-resonant transport of the odd charge state (see figure 2.9a). The enhanced conductance at zero-bias is caused by many body-correlations which enhance elastic spin-flip processes via the unpaired spin as shown in figure 2.9b. The width of the zero bias peak is related to the strength of the many-body correlations and is captured in the parameter T_k, which is the Kondo temperature. Equation 2.15 shows the dependence of T_k on the coupling of the molecule to the electrodes (Γ) and the energy it costs to add an electron (ΔE):

$$\text{Peak width} \sim T_k \sim \sqrt{\Gamma \Delta E} \exp \frac{\pi \epsilon_0 (\epsilon_0 + \Delta E)}{\Gamma \Delta E}. \tag{2.15}$$

A larger coupling results in a larger T_k and this can be understood from Heisenberg's

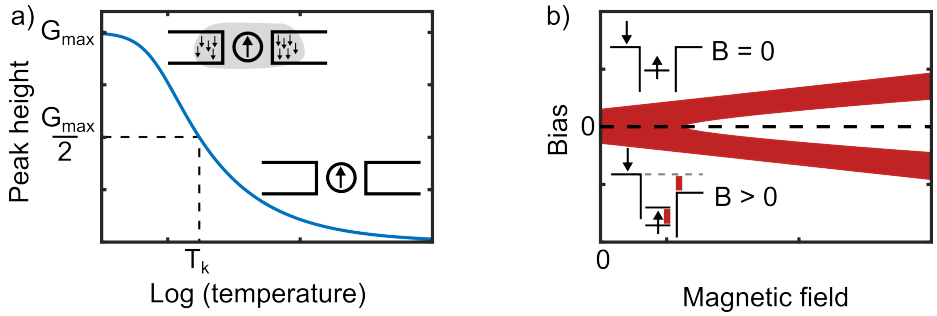

Figure 2.10: Temperature and magnetic-field dependence of the zero-bias differential conductance peak. a) Peak height versus temperature. It has a non-linear dependence characterized by T_k. Far above T_k correlations are not present, below it a screening cloud develops. b) Magnetic-field dependence of the zero-bias peak. The peak splits with increasing magnetic field and when the bias matches the splitting of the degenerate spin-1/2 state, the peak appears at this voltage as seen in the lower schematic.

uncertainty principle $\delta\tau\delta E \geq \hbar/2$. A larger coupling means a shorter residence time ($\Delta\tau$) of the electron on the molecule, therefore a higher energy uncertainty (ΔE) is possible. For well coupled systems correlations can thus even form if the unpaired electron on the molecule is located far away from the Fermi energy of the electrodes.

Figure 2.10 shows the temperature dependence of the peak maximum and the magnetic-field dependence of the zero-bias peak. The temperature dependence of the peak height (panel a)) is non-linear and is one of the signatures of Kondo correlations. The parameter determining the strength of the Kondo correlations, T_k, appears again. It is the temperature at which the peak height has half its maximum value. Far above T_k no correlations are present; far below this value a screening cloud of electrons with opposite spin is present on the electrodes due to the strong many-body correlations.

Applying a magnetic-field (figure 2.10b) will suppress the zero-bias peak due to splitting of the degenerate spin-1/2 state. Only on applying a bias voltage of the same energy as the splitting, the differential conductance peak reappears. The slope of the splitting is defined by the magnetic moment of the electron and therefore, ignoring orbital effects, has a g-factor of 2.

The above example is for Kondo-correlations with a single spin. It only occurs when an odd number of spins is present on the molecule and is a vital tool to determine the parity of the occupation of the molecule. Kondo correlations can also occur in systems with a higher spin, as will be seen further on in this thesis. Although more complex features occur in off-resonant transport, they do share the same general characteristics of the conductance peak depending on a magnetic field as well as the presence of strongly non-linear temperature dependence.

REFERENCES

[1] J. C. Cuevas and E. Scheer, *Molecular Electronics: An Introduction to Theory and Experiment* (World Scientific Publishing, 2010).

[2] J. M. Thijssen and H. S. J. Van der Zant, *Charge transport and single-electron effects in nanoscale systems,* Phys. Status Solidi B **245**, 1455 (2008).

[3] T. Ihn, *Semiconductor Nanostructures: Quantum states and Electronic Transport* (Oxford University Press, 2010).

[4] G. C. Solomon, D. Q. Andrews, T. Hansen, R. H. Goldsmith, M. R. Wasielewski, R. P. Van Duyne, and M. A. Ratner, *Understanding quantum interference in coherent molecular conduction,* J. Chem. Phys. **129**, 054701 (2008).

[5] R. Frisenda, *OPE3: a model system for single-molecule transport,* Ph.D. thesis, Delft University of Technology (2016).

[6] J. S. Seldenthuis, *Electrical and Mechanical Effects in Single-Molecule Junctions,* Ph.D. thesis, Delft University of Technology (2011).

[7] M. Grobis, I. Rau, R. Potok, and D. Goldhaber-Gordon, *Kondo effect in mesoscopic quantum dots,* Handbook of Magnetism and Advanced Magnetic Materials (2007).

[8] I. Mermin and N. David, *Solid State Physics* (Harcourt Brace College Publishers, 1976).

[9] B. J. van Wees, H. van Houten, C. W. J. Beenakker, J. G. Williamson, L. P. Kouwenhoven, D. van der Marel, and C. T. Foxon, *Quantized conductance of point contacts in a two-dimensional electron gas,* Phys. Rev. Lett. **60**, 848 (1988).

[10] R. A. Webb, S. Washburn, C. P. Umbach, and R. B. Laibowitz, *Observation of $\frac{h}{e}$ Aharonov-Bohm oscillations in normal-metal rings,* Phys. Rev. Lett. **54**, 2696 (1985).

3

ELECTRIC-FIELD CONTROL OF INTERFERING TRANSPORT PATHWAYS IN A SINGLE-MOLECULE ANTHRAQUINONE TRANSISTOR

We investigate electron transport through an anthraquinone-based single-molecule. With the use of an electric field induced by a gate electrode, the molecule is reduced resulting into a ten-fold increase in the off-resonant differential conductance. Theoretical calculations link the change in differential conductance to a reduction-induced change in conjugation, thereby lifting destructive interference of transport pathways.

This chapter has been published in Nano Letters **15**, 5569-5573 (2015) [1]. I would like to thank J.M. Thijssen for help with the calculations.

3.1. INTRODUCTION

Electric-field control by a gate electrode is a promising route to manipulate charge transport through single molecules[2]. It enables detailed spectroscopy as a function of bias and gate voltage, allowing the systematic study of electron transport through single-molecule junctions; examples of which are Coulomb blockade[2], the Kondo effect[3, 4], vibrational excitations [5, 6] and electronic excitations[7]. All these experiments can be essentially understood by considering transport channels through individual orbitals. In some molecules, however, transport may involve more than one orbital at the same time, possibly leading to interfering pathways[8, 9]; changing the occupancy can then induce dramatic changes in the conductance[10]. In quinone-type molecules, this phenomenon is traditionally understood as a change in the conjugation of the pi-electron system (see figure 3.1a). Transport experiments in which the occupancy is changed have been performed at room-temperature in solution using electro-chemical setups [11–13], however these lack the direct electric-field control which can be attained with a gate electrode in solid-state devices.

In this chapter we investigate the effect of the electric-field on charge transport through a molecule with an anthraquinone core (AQ). The molecule has spacers terminated by sulfur groups[14] for binding to gold electrodes. The neutral molecule is shown in figure 3.1a together with its first two reduced states. It is designed as a redox switch, where the neutral state is in a cross-conjugated form and the twice-reduced state has a linear conjugation. In van Dijk *et al.*[14] it is shown that these two reductions of AQ are reversible and change the electronic structure of the molecule. Furthermore, the occurrence of quantum interference in AQ and its functioning as a redox switch have been investigated theoretically[15, 16]. On the experimental side conducting force microscopy[17], eutectic Ga-In top contacting[18] and mechanically controlled break-junctions[19] have shown that AQ has a suppressed conductance, which is linked to its cross-conjugation. However, in-situ switching of the conjugation as a function of electric-field has not yet been reported. Here we study AQ in a solid-state three-terminal device and demonstrate electric-field switching of molecular conjugation.

3.2. MEASUREMENTS

To create three-terminal metal/molecule/metal junctions, gold wires are deposited on top of an oxidized aluminium gate; the result is shown in figure 3.1b. On a silicon chip 22 of such junctions are typically fabricated. A solution of dichloromethane with a concentration of 0.1 mM of AQ is then deposited on the chip. In this solution and at room-temperature, the gold wire is controllably thinned down by electromigration[20] until its resistance is about 5 KΩ. Subsequently, the gold wires are left to self-brake[21] until the resistance of the junction is between 100 KΩ and 1 MΩ; this takes one to two hours depending on the thickness of the gold wire. To prepare for cool-down, the sample space is pumped down, evaporating the dichloromethane. The chip is then

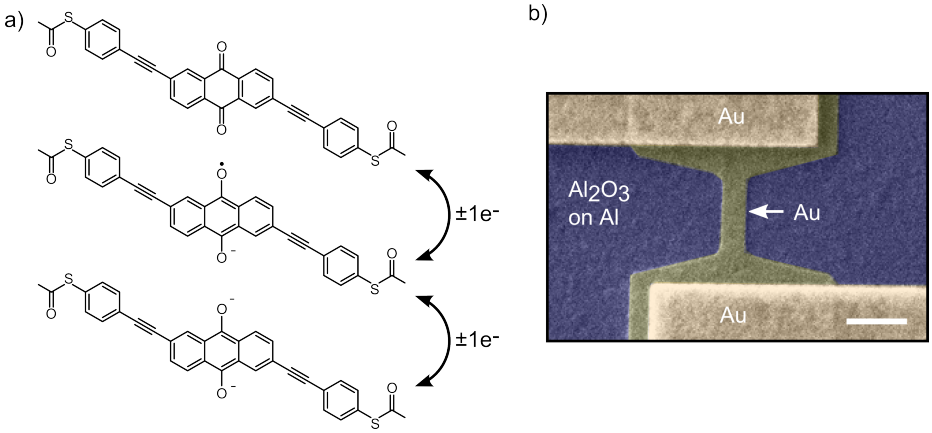

Figure 3.1: a) Anthraquinone with thiolated spacers. The neutral molecule can be reversibly reduced in two steps, thereby changing the conjugation from cross-conjugation (top) to linear conjugation (bottom). b) Scanning electron microscope image of a break junction on top of an aluminium gate electrode prior to electromigration; scale bar indicates 250 nm.

cooled to 4 K in a liquid helium dewar. Measurements are performed by applying a voltage on the gate electrode and across the source electrodes while measuring the current at the drain. The experimental system possesses a heater-resistor and a 1K pot, which makes temperature-dependent measurements possible.

In this chapter, we discuss five different junctions that show a pronounced charge-state dependence of the off-resonant differential conductance. Figure 3.2a shows the differential conductance map as a function of bias (V) and gate (V_g) voltage of one of the five junctions. In this sample (which we will call sample A from now on) two slanted lines cross at V_g = -2.1 V. The two red-coloured triangles originating from this crossing point indicate areas in which transport is dominated by resonant single electron tunnelling (SET). In the regions left and right of the vertical pair of triangles, transport is off-resonant involving higher-order co-tunnel processes. The regions of off-resonant transport left and right of the resonance differ in charge by one electron on the molecule; as denoted by the transition from N to N+1, where N is the excess charge on the molecule, with the most likely scenario N=0 (see also below). Comparing the differential conductance of the charge-states, it can be clearly seen that the level of differential conductance in the right charge-state is about an order of magnitude higher than that of the left charge-state.

The differential conductance as a function of gate voltage at zero bias is shown in figure 3.2b and clearly shows the difference in off-resonant differential conductance between the two charge-states. At gate voltages below V_g = -2.1 V the differential conductance is around G = 0.27 μS. Increasing the gate voltage above V_g = -2 V, the differential conductance increases to about G = 2.5 μS far from the resonance (see

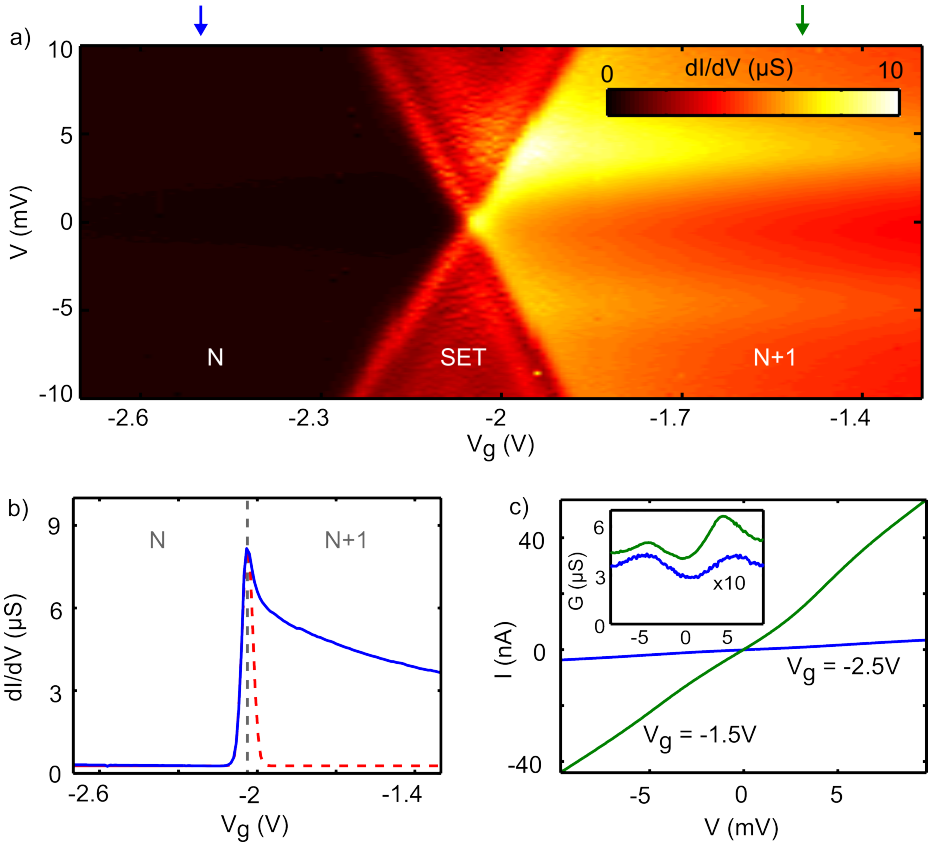

Figure 3.2: Bias and gate voltage dependent measurement of sample A at 2.9 K. a) Numerical derivative (dI/dV) of the current as a function of bias (V) and gate (V_g) voltage. Two charge-states are present (labeled N and N+1) and the on-resonant transport regime is indicated by the two red triangles (labeled SET). On the left the off-resonant differential conductance is low, as indicated by the black color. On the right, the red/yellow colors represents a much higher off-resonant differential conductance in the adjacent charge-state. The blue and green arrows indicate the location of the IV traces in panel c). b) Blue line: differential conductance versus gate voltage at V = 0 mV. The red dashed line is a Gaussian function with an electronic coupling, Γ, of 1.2 meV. c) Current versus bias voltage at the two different gate voltages shown by the arrows in panel a). The inset shows the corresponding differential conductance. The differential conductance of the trace at V_g = -2.5 V is multiplied by 10.

Sample	Differential conductance G(N) (μS)	Differential conductance G(N+1) (μS)	Differential conductance difference G(N+1)-G(N) (μS)
A	0.27	2.54	2.27
B	0.75	2.14	1.39
C	0.27	2.38	2.11
D	0.43	2.71	2.28
E	6.98	8.77	1.79

Table 3.1: Off-resonant low-bias differential conductance in the N and N+1 charge-state for five different samples. The last column shows the difference in differential conductance between the two charge-states. All values are in μS. The off-resonant differential conductance is determined by fitting the left and right side of the N to N+1 resonance with a Lorentzian (Gaussian for sample A) and determining the offset conductance. For Sample A the N+1 differential conductance was estimated by determining the lowest value it reaches in the N+1 state.

figure 3.8a in the appendix (section 3.4)). The peak near V_g = -2 V is due to resonant transport. It is striking to see that the resonance itself is strongly asymmetric, contrary from what would be expected from usual quantum dot theory[22, 23]. The left side of the resonance follows a Gaussian line-shape (red dashed line in fig 3.2b), but the right side deviates strongly from the Gaussian line-shape. For the other samples an asymmetry is also found, albeit less pronounced (see the appendix).

Figure 3.2c shows two current-voltage traces taken in the left and right charge-state (blue and green arrows in figure 3.2a). The inset shows that at any bias voltage the differential conductance increase is more than an order of magnitude. Figure 3.5a in the appendix shows that the above described features persist even at higher bias voltages up to 40 mV.

The inset of figure 3.2c also shows the presence of excitations of a few meV in the off-resonant transport regime of both charge-states (the one in the N charge-state is not visible with the contrast settings used to obtain figure 3.2a). This observation of excitations in both off-resonant transport regimes (N and N+1), combined with the fact that excitations with the same energy are present in the resonant transport regime, supports the conclusion that the features in figure 3.2 are from the same molecule (see figure 3.6 in the appendix). This is further strengthened by figure 3.5b in the appendix, which shows the emergence of a weak zero-bias peak in the right charge-state, indicative of Kondo physics associated with an unpaired electron[3, 4, 24]. It suggests that by going from the left to the right charge-state, a single electron is added to the system which changes the occupation from even to odd. Since it is unlikely that many electrons can be put on a small molecule, we assign the even occupation to the neutral state (N=0) and the odd occupation to the singly reduced state.

Four other samples have also been identified which show a charge-state dependent increase of off-resonant transport when comparing adjacent charge-states. All

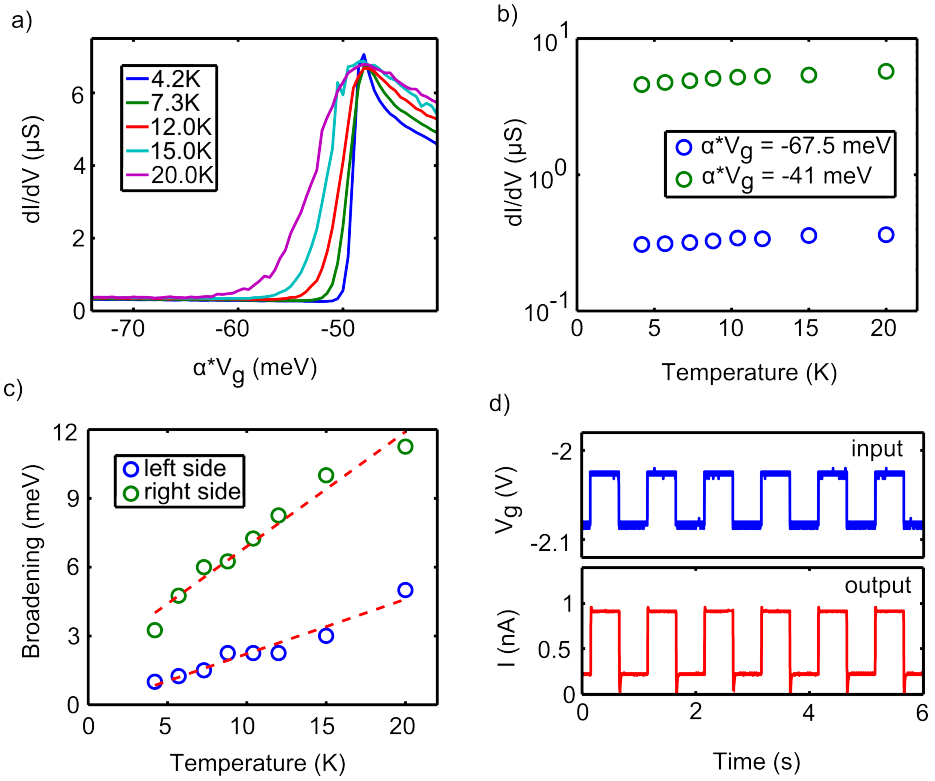

Figure 3.3: Temperature dependence and switching of sample A. a) Temperature dependence of the differential conductance versus gate voltage at V = 0 mV. Gate is multiplied with α = 25 mV/V, so that the x-axis represents energy scale in meV. b) Log-plot of the differential conductance as a function of temperature at two gate voltages. c) Broadening of the left and right side of the resonance as a function of temperature. Red dashed lines are linear fits to the data with broadening= $c_1 + c_2 * T$ where $c_1 = -0.006, c_2 = 0.01$ for the left side and $c_1 = 0.08, c_2 = 0.02$ for the right side. d) Conductance switching of the junction at 2.9 K. A square wave is applied on the gate electrode as input. The output is the source-drain current at V = 1 mV.

these samples, including sample A, are shown in figure 3.8 and 3.9 in the appendix. Table 3.1 lists the conductance in the left charge-state and adjacent charge-state to the right (N to N+1 transition) for these five samples. It can be seen that the conductance increase is approximately the same for all junctions.

To further investigate sample A, the temperature dependence of the differential conductance versus gate voltage at V = 0 mV is shown in figure 3.3a. The figure shows that the resonance widens as the temperature is increased whereas the off-resonant differential conductance remains almost the same. It should be noted that the asymmetric shape persists for all temperatures. Figure 3.3b compares the off-resonant differential conductance in the two charge-states, showing a slight increase with temper-

ature. This slight increase indicates that Kondo physics is not the main cause of the conduction increase in the right charge-state, as in that case a logarithmic decrease is expected. To quantify the widening of the resonance we have plotted in figure 3.3c the width of the left side at half maximum and the right side at 3/4th maximum of the resonance. The width on both sides of the resonance has a linear dependence with temperature. Linear dependence is expected when a life-time broadened resonance is temperature broadened by the Fermi function in the leads[23].

It is interesting to note that the redox-induced conductance switching can be performed reversibly at speeds limited by the RC time of the set-up. Figure 3.3d shows the result when changing the gate voltage in a square-wave fashion on the time scale of seconds. In this experiment, the square wave signal on the gate was centered around the resonance gate voltage, and as the lower panel shows, it results in a square wave output signal. Figure 3.11 in the appendix shows a 10 Hz sine wave modulating the current output of the junction.

3.3. DISCUSSION

The difference in conductance between the N and N+1 charge-states resembles the transmissions obtained from theoretical calculations on molecules providing two interfering pathways for electrons [9, 15, 25]. Quinone structures are examples of such structures[26]. Indeed, these calculations invariably show a significant increase of the conductance upon reduction, even in the off-resonant regime when Coulomb blockade can be significant[10].

We have performed GW calculations on the π-system of the central anthraquinone (AQ) and anthracene (AC) group using the Pariser-Par-Pople (PPP) model Hamiltonian with the Ohno parametrization[27]. The GW implementation in the GPAW code was used[28–30], with the parameters $U = 11$ eV and $t = -2.5$ eV for the PPP Hamiltonian and $V = -10$ eV for the oxygen[31, 32]. Figure 3.4 shows the calculated transmission through the AQ and AC groups.

The transmission of the AQ group (figure 3.4a) clearly shows an increase in the off-resonant conductance upon reduction from the N to N+1 charge-state, both on the linear (lower panel) and logarithmic scale (upper panel). In addition, two interference dips can be identified in the N=0 charge-state indicative of destructive quantum interference. Although it is often difficult to come to a quantitative agreement in the field of molecular electronics, it is interesting to note that the experimental charge-state dependent differential conductance increase of approximately $1 \sim 2\,\mu$S (table 3.1) is of the same order of magnitude as is present in the calculations (the increase in transmission is approximately T= 0.01, which corresponds to a conductance increase of $1\,\mu$S).

An important question is whether indeed the quinone-character is responsible for the observed behaviour. To verify this, we also calculated the transmission for anthracene (figure 3.4b). This molecule, which lacks the oxygen stub-structures characteristic for quinone, shows a small decrease in the transmission upon reduction and

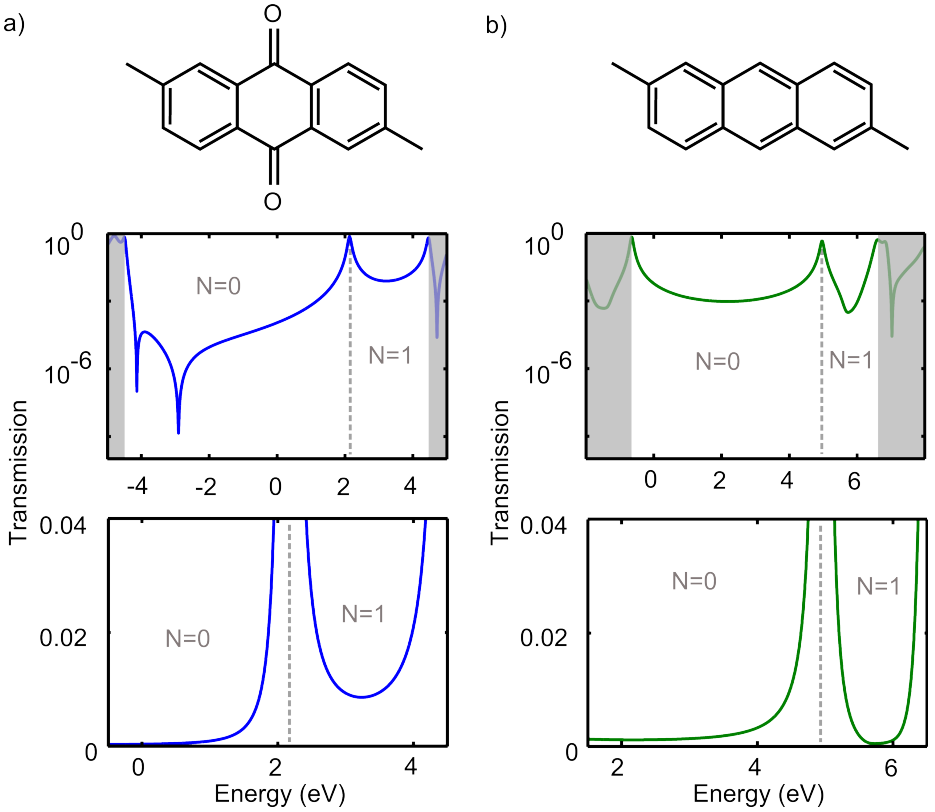

Figure 3.4: Transmission of the anthraquinone and anthracene group, calculated using the GW method with Ohno parametrization[27](parameters taken from Pedersen[32] and Roos and Skancke[31]) a) Transmission for the anthraquinone group. Top panel: Anthraquinone group, dashed lines are the entry and exit site for the transmission calculation. Middle panel: Transmission on a logarithmic scale. The N=0 and N=1 charge-states are identified and the dashed line marks the boundary between the charge-states i.e. it marks the position of the LUMO. The HOMO is visible at an energy of -4.5 eV. Bottom panel: Transmission on linear scale zoomed-in on the reduction (LUMO) peak. b) Transmission of the anthracene group. Top panel: Anthracene group, dashed lines are the entry and exit site for the transmission calculation. Middle panel: Transmission on a logarithmic scale. The N=0 and N=1 charge-states are identified and the dashed line marks the boundary between the charge-states i.e. it marks the position of the LUMO. The HOMO is visible at an energy of -0.7 eV. Bottom panel: Transmission on linear scale zoomed-in on the reduction (LUMO) peak.

lacks the quantum interference dip structure in the N=0 charge-state. This supports the conclusion that quantum interference is responsible for the charge-state dependent off-resonant differential conductance measured in the anthraquinone molecule.

Comparing the results for the device analysed in this paper and the four presented in the appendix shows that, in addition to the common feature of a conductance increase upon reduction, there is device-to-device variation. The explanation for such a variation can be found in the non-reproducibility of the coupling between molecules and electrodes, and in image charge effects [33]. Calculations incorporating these effects are shown in the appendix (figure 3.12).

To conclude, we have shown that when changing the electron occupation of an anthraquinone-based single-molecule junction the off-resonant differential conductance changes dramatically. This is accompanied with an asymmetric resonance between the two charge-states. Both effects are linked to an occupation dependent conjugation of anthraquinone; this is supported by GW calculations. This research thus realizes the in-situ change of conjugation in a solid-state single-molecule system and opens up the way to detailed experimental investigation of π-conjugation based transport phenomena and interfering transport pathways in single molecules.

3.4. APPENDIX

FURTHER INVESTIGATIONS OF SAMPLE A

Figure 3.5 further investigates sample A discussed extensively in the main article; it presents extended differential conductance maps in bias (a) and gate-voltage (b). Figure 3.5a again shows the resonance flanked by a low-conducting charge state on the left and a high-conducting charge-state on the right. It can be seen that at bias voltages up to at least 40 mV the charge-state dependent differential conductance is present. At high bias voltages noise starts to dominate the transport through the junction and for this reason we have not increased the bias voltage further.

Figure 3.5b shows a differential conductance trace at V_g = 3 V as a function of bias. The excitation can be identified as mentioned in the main text. Next to the excitation also a weak zero-bias peak appears. The inset shows that the weak zero-bias peak becomes visible when the contribution from the excitation decreases. We attribute the presence of this peak to the Kondo effect originating from odd occupancy of the molecule with an unpaired spin. The Kondo effect in conjunction with the observed differential conductance increase, suggests that the left charge-state is the neutral anthraquinone molecule and the right state the singly reduced one.

Figure 3.6 shows figure 3.2a from the main text. The resonance and excitations are annotated: the black dashed lines are the resonance, blue dashed lines are the excitations in the on-resonant regime and the green dashed lines are the excitations in the off-resonant regime. In figure 3.6b the color scale is changed as to show the presence of the excitation in the N charge-state. Both excitations in the N and N+1 charge state match with their respective excitation in the resonant transport regime.

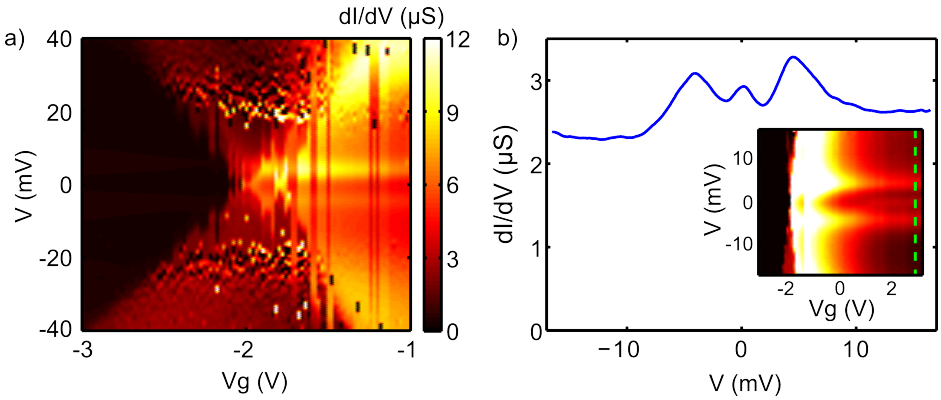

Figure 3.5: Extended differential conductance maps of sample A. a) Gate-bias map of the differential conductance for bias voltages up to 40 mV at 3.8 K. The resonance is visible in the middle centered around V_g = -2 V. To the left and right of it, the N (black) and N+1 (red/yellow) charge-state can be identified. b) Differential conductance trace as a function of bias voltage at V_g = 3 V and at 4.3 K. The inset shows the gate-bias map of which the single trace was taken (indicated by the green dashed line in the inset).

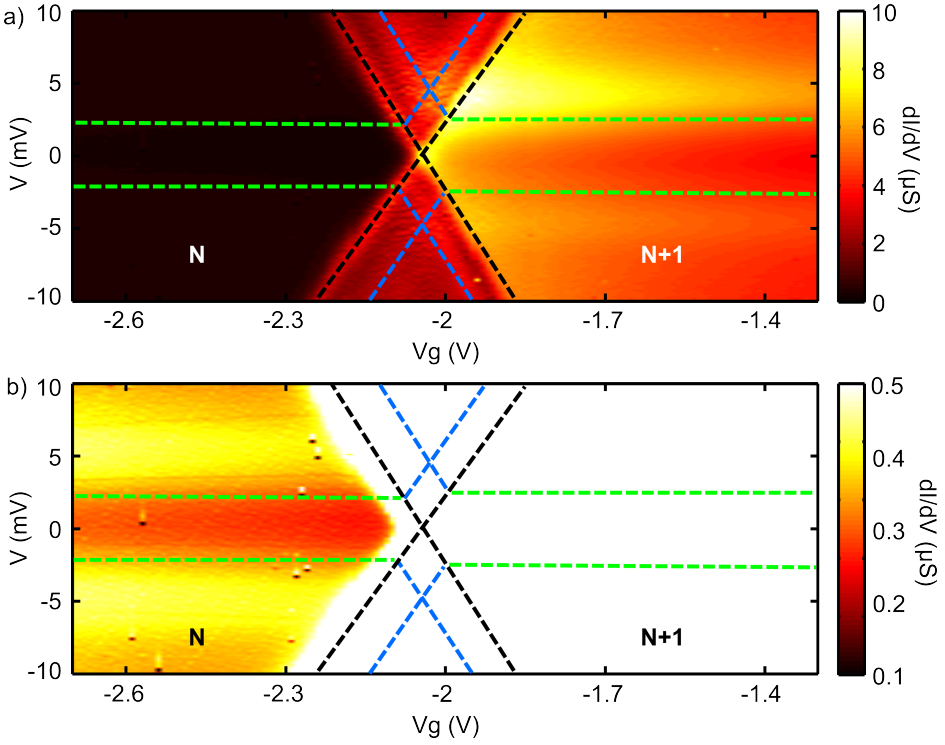

Figure 3.6: Bias and gate voltage dependent measurement of sample A at 2.9 K. a) Numerical derivative (dI/dV) of the current as a function of bias (V) and gate (V_g) voltage. Two charge-states are present (labelled N and N+1) divided by the resonant transport regime. The dashed black lines show the boundary between the resonant and off-resonant transport regime. The green dashed lines show the location of the off-resonant excitations. The blue dashed lines show the excitation in resonant regime. b) Same measurement as in panel a), however the contrast is increased to show the excitation in the N charge-state.

Care must be taken that the energy of the off-resonant excitations is not necessarily given by the location of the maximum, but rather by its onset due to possible non-equilibrium population effects[34]. The fact that both excitations in the N and N+1 charge state match with an excitation in the resonant transport regime support the conclusion that the features in sample A are from the same molecule.

The differential conductance and current of Sample A at finite bias are further investigated in figure 3.7. It is interesting to note that the differential conductance in the resonant transport region (red triangles) is smaller than in the right charge-state (N+1), as can be seen in figure 3.7a. Figure 3.7b further exemplifies this by showing the differential conductance at a bias of -8 mV. It can be seen that the differential conductance follows a step-like pattern, where the first step is around a gate voltage of -2.2 V and the second step is around -1.9 V. The two steps have approximately the

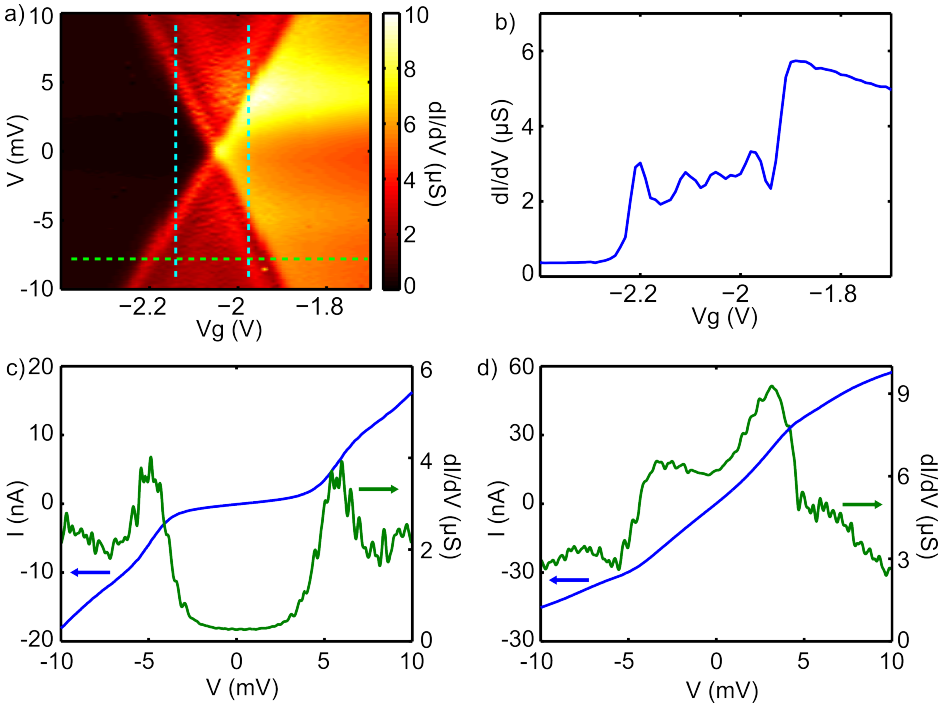

Figure 3.7: Current and differential conductance traces at finite bias and at 2.9 K. a) Differential conductance map of sample A. The dashed green line is panel b), the two light blue lines are, starting from left, panel c) and panel d) respectively. b) Differential conductance versus gate voltage at -8 mV bias. c) Current in blue and its differential conductance in green at a gate voltage of -2.14 V as function of bias. d) Current in blue and differential conductance in green at a gate voltage of -1.98 V as a function of bias.

same height. Figure 3.7c and 3.7d show IV's taken at gate voltages on the respective left and right side of the resonance. Here again it can be seen that the right charge-state is higher in differential conductance than the resonant transport region. The fact that the differential conductance in the resonant transport region is lower than in the right charge-state is only seen in sample A and is not expected from standard theory on coherent or non-coherent electron transport through quantum dots or molecules.

OTHER SAMPLES

We have observed charge-state dependent off-resonant differential conductance in five different junctions (in total 138 junctions were electromigrated), they are shown in figure 3.8 and figure 3.9. The left side of the figures show differential conductance traces at two bias voltages as a function of gate voltage. The right side of the figures show the differential conductance maps of all five samples. In the extended differential conductance trace of sample A (same sample as discussed in the main article) it

can be seen that a jump is present at V_g = -1 V. This jump is reproducibly found in all measurements of sample A and is attributed to an electrostatic switch in the environment (e.g. charge trap in the gate oxide). As in sample A, sample B and C both show two charge-states that can be accessed. From the differential conductance traces it can be seen that the differential conductance in the right charge-state is higher than in the left charge-state. The traces at V = +10 mV show that the increased differential conductance in the right charge-state persists at finite bias.

Sample D and E are different with respect to the other three samples discussed so far, as there are three charge-states accessible. Again an increase can be seen in the differential conductance when going from the left (N) to the right (N+1) charge-state. When going from the N+1 to the N+2 charge-state a further increase of the off-resonant differential conductance is present. In both samples a large zero-bias peak is present in the N+2 charge-state. Nevertheless at finite bias (green curves in the left panels) the differential conductance still shows a clear increase when compared to N+1 charge-state.

All five samples (A-E) show an off-resonant differential conductance increase when going from the N to N+1 charge-state. In all samples the N+1 charge-state displays a zero bias peak, which motivates the assignment of the N+1 charge-state to this state (i.e. odd occupancy). It is also clear that at finite bias the charge-state dependent off-resonant conductance is still present, thus showing that the zero-bias peak is not the main contribution to the increase of off-resonant conductance in the N+1 charge-state. However, apart from the similarities between the samples there are also differences in the differential conductance maps. For example: the partly disappearing resonance of sample B, the increased noise in the N+1 charge-state of sample C and the appearance of the N+2 charge-states in sample D and E. These differences are attributed to junction to junction variation of the specific spatial configuration of the electrodes and the molecule. These variations can result in a different molecule-lead coupling, a different gate coupling and image charge effects.

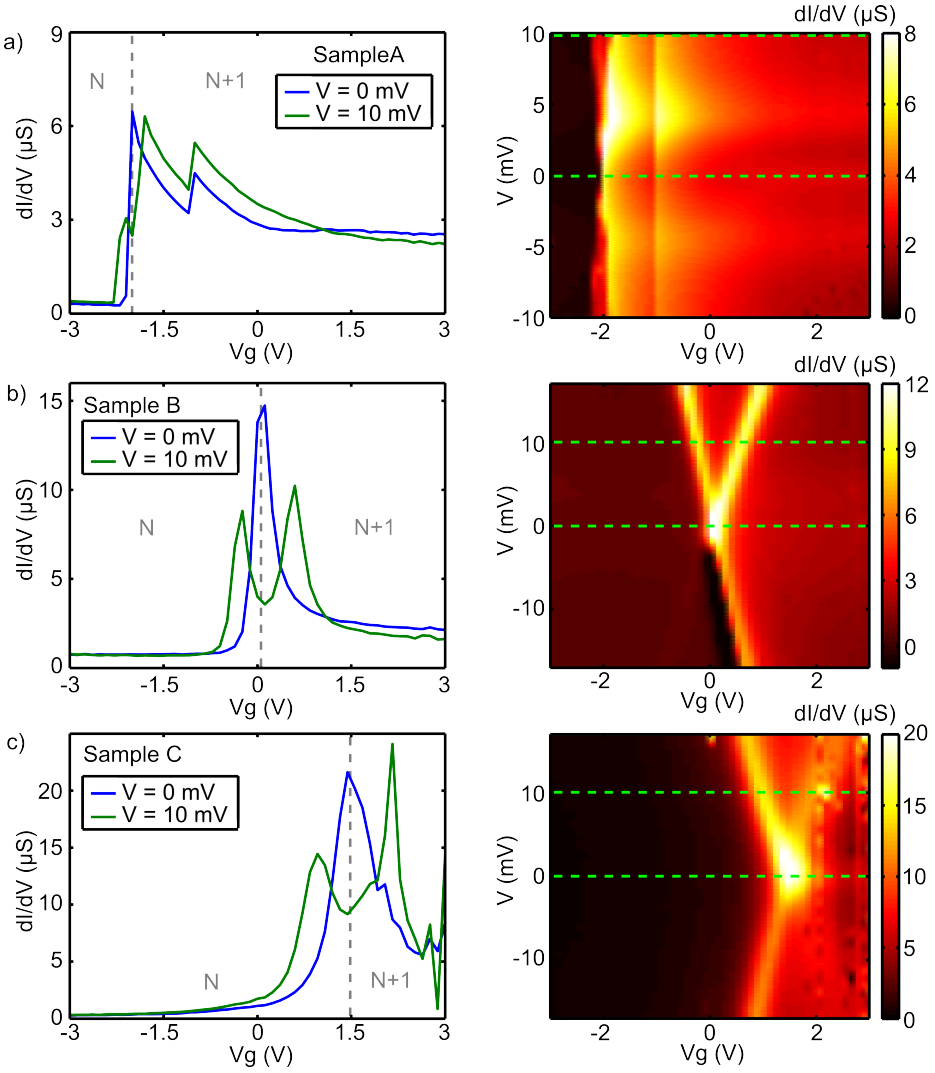

Figure 3.8: Differential conductance traces (left panels) for two bias voltages as a function of gate voltage; the corresponding differential conductance maps are shown next to them (right panels). In the left panels the charge-states are labelled with N and N+1. The vertical dashed lines show the positions of the zero-bias resonances, dividing the N and N+1 charge-states. Sample A was measured at 2.8 K; sample B and C were measured at 6 K.

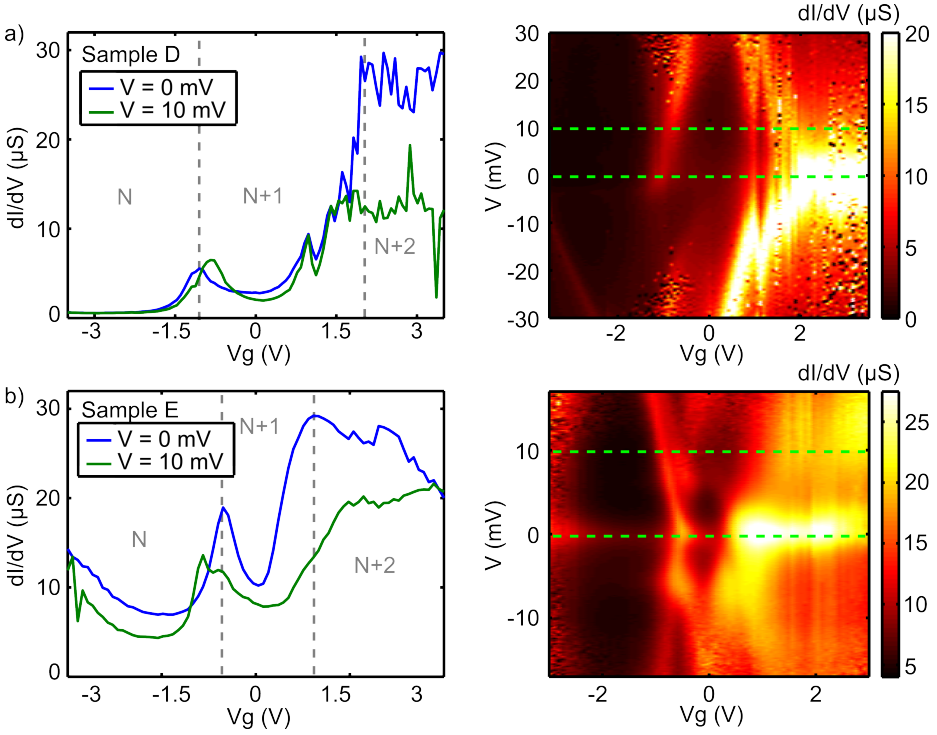

Figure 3.9: Differential conductance traces (left panels) for two bias voltages as a function of gate voltage; the corresponding differential conductance maps are shown next to them (right panels). In the left panels the charge-states are labelled with N, N+1, and N+2. The vertical dashed lines show the positions of the zero-bias resonances, dividing the N, N+1 and N+2 charge-states. Sample D was measured at 2.3 K; sample E at 3.8 K.

RESONANCE BROADENING AND ASYMMETRY

In figure 3.10 a comparison is made of the N to N+1 resonances as taken from figures 3.8 and 3.9. To compare the individual resonances the gate voltage is multiplied by the experimentally determined gate coupling (α) of each sample and the resonance maximum is aligned at zero. It can be clearly seen that all resonances display a degree of asymmetry around zero. When the width of the resonance is smaller the asymmetry appears more pronounced. This is clearly seen when comparing sample A, B and C. The asymmetry is quantified in table 3.2. The widths of the resonances have all been fitted to a Lorentzian line-shape, except for sample A where the broadening is of the same order as the thermal broadening at 2.3 K. This resulted in the use of a Gaussian to fit the left side of the line-shape. The right side of the resonance in sample A could not be fit by a Lorentzian nor a Gaussian.

Sample	**Broadening left side (meV)**	**Broadening right side (meV)**
A	1.2	-
B	2.2	3.9
C	5.9	10.7
D	19.1	16
E	8.1	8.9

Table 3.2: Comparison of the broadening of the left and right side of the N to N+1 resonance. For sample A a Gaussian line shape is used to determine the broadening. The data of samples B-E is fit to a Lorentzian line shape.

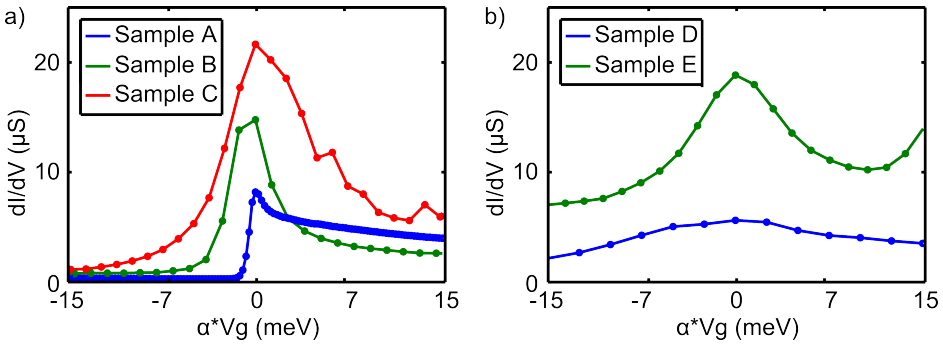

Figure 3.10: Differential conductance traces of all 5 samples at the N to N+1 resonance as a function of energy for V = 0 mV. The x-axis is scaled by the respective experimentally determined gate-coupling (α) of each sample and the maximum of the resonances are aligned at 0. a) Sample A, B and C with respective gate couplings α_A = 25 mV/V, α_B = 11 mV/V and α_C = 10.3 mV/V. b) Sample D and E with respective gate couplings α_D = 35.7 mV/V and α_E = 18.9 mV/V.

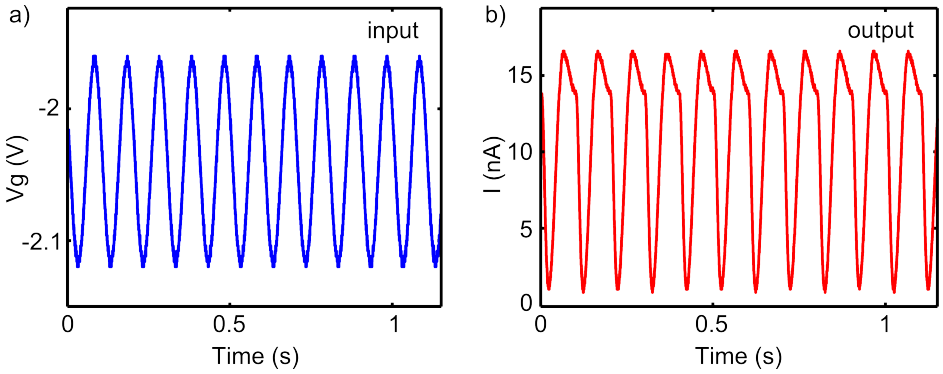

Figure 3.11: Current switching with a sine signal on the gate (input) at 2.9 K. a) Gate voltage input versus time. The signal is a 0.15 V peak-to-peak amplitude sine wave with a frequency of 10 Hz on top of a -2.03 V background. b) The current at the drain (output) at a bias voltage of 2.5 mV.

SINE WAVE MODULATION OF THE OFF-RESONANT CONDUCTANCE

Figure 3.11 shows the current of sample A at a fixed bias of 2.5 mV when a sine signal is applied to the gate electrode. The current varies at the same rate as the voltage on the gate electrode. When applying a sine signal, the absolute magnitude of $\frac{dV}{dt}$ at the gate is smaller than for a square wave signal. This means that the current contribution from the capacitance of the set-up ($I = C * \frac{dV}{dt}$) is smaller as well, making it possible to use higher frequencies on the input.

IMAGE CHARGES AND COUPLING STRENGTH

Figure 3.12 shows the transmission of the anthraquinone group calculated with a Pariser-Parr-Pople hamiltonian and the GW method as described in the main article, but for a different level broadening (Γ) and with image charges included. The image charge effect was included by modifying the relative dielectric permittivity (ϵ_D)[35] by a factor of 2. We note that the image charge effect reduces the HOMO-LUMO gap typically by a factor of 5 to 10 (see Kaasbjerg and Flensberg[36]) and shifts portions of the interference dips. It is clear that these variations change the magnitude of the conductance increase upon reduction as observed in the experiment.

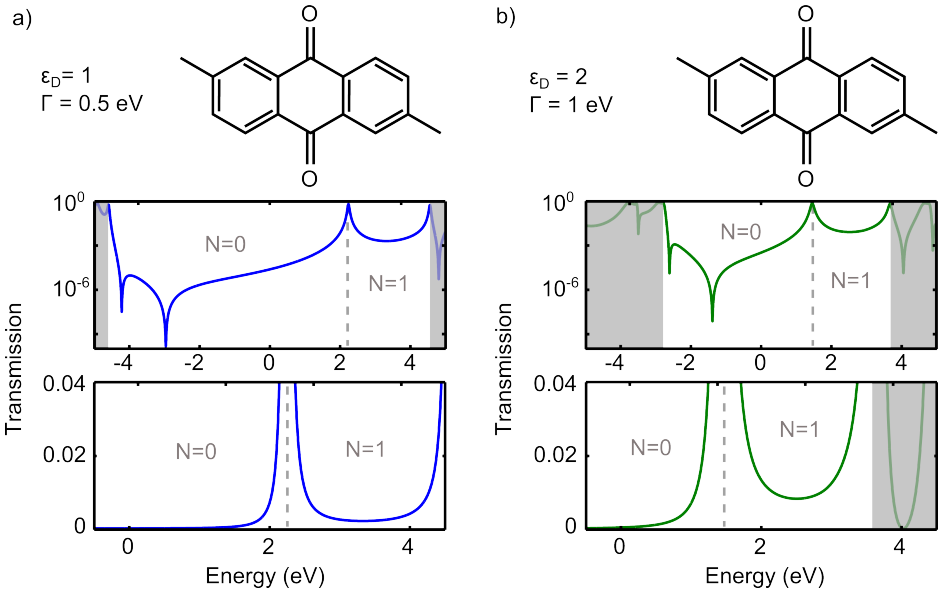

Figure 3.12: Calculated transmission for the anthraquinone group with different coupling and inclusion of image charges. a) Transmission of the anthraquinone group with reduced coupling as compared to the calculations in the main paper (Γ = 1 eV). The N and N+1 charge-states are identified and the dashed line marks the reduction peak. Top panel is on a logarithmic scale. Bottom panel is the transmission on a linear scale zooming-in on the reduction peak. b) Transmission of the anthraquinone group with image charges included. Top panel is on a logarithmic scale. Bottom panel is the transmission on a linear scale zoom-in on the reduction peak.

REFERENCES

[1] M. Koole, J. M. Thijssen, H. Valkenier, J. C. Hummelen, and H. S. J. van der Zant, *Electric-field control of interfering transport pathways in a single-molecule anthraquinone transistor,* Nano Lett. **15**, 5569 (2015).

[2] H. Park, J. Park, A. K. L. Lim, E. H. Anderson, A. P. Alivisatos, and P. L. McEuen, *Nanomechanical oscillations in a single-C60 transistor,* Nature **407**, 57 (2000).

[3] J. Park, A. N. Pasupathy, J. I. Goldsmith, C. Chang, Y. Yaish, J. R. Petta, M. Rinkoski, J. P. Sethna, H. D. Abruna, P. L. McEuen, and D. C. Ralph, *Coulomb blockade and the Kondo effect in single-atom transistors,* Nature **417**, 722 (2002).

[4] W. Liang, M. P. Shores, M. Bockrath, J. R. Long, and H. Park, *Kondo resonance in a single-molecule transistor,* Nature **417**, 725 (2002).

[5] L. H. Yu, Z. K. Keane, J. W. Ciszek, L. Cheng, M. P. Stewart, J. M. Tour, and D. Natelson, *Inelastic electron tunneling via molecular vibrations in single-molecule transistors,* Phys. Rev. Lett. **93**, 266802 (2004).

[6] E. A. Osorio, K. O'Neill, N. Stuhr-Hansen, O. F. Nielsen, T. Børnholm, and H. S. J. van der Zant, *Addition energies and vibrational fine structure measured in electromigrated single-molecule junctions based on an oligophenylenevinylene derivative,* Adv. Mater. **19**, 281 (2007).

[7] E. A. Osorio, K. O'Neill, M. Wegewijs, N. Stuhr-Hansen, J. Paaske, T. Børnholm, and H. S. J. van der Zant, *Electronic excitations of a single molecule contacted in a three-terminal configuration,* Nano Lett. **7**, 3336 (2007).

[8] P. Sautet and C. Joachim, *Electronic interference produced by a benzene embedded in a polyacetylene chain,* Chem. Phys. Lett. **153**, 511 (1988).

[9] G. C. Solomon, D. Q. Andrews, T. Hansen, R. H. Goldsmith, M. R. Wasielewski, R. P. Van Duyne, and M. A. Ratner, *Understanding quantum interference in coherent molecular conduction,* J. Chem. Phys. **129**, 054701 (2008).

[10] K. G. L. Pedersen, M. Strange, M. Leijnse, P. Hedegård, G. C. Solomon, and J. Paaske, *Quantum interference in off-resonant transport through single molecules,* Phys. Rev. B **90**, 125413 (2014).

[11] S. Tsoi, I. Griva, S. A. Trammell, A. S. Blum, J. M. Schnur, and N. Lebedev, *Electrochemically controlled conductance switching in a single molecule: Quinone-modified oligo(phenylene vinylene),* ACS Nano **2**, 1289 (2008).

[12] N. Darwish, I. Díez-Pérez, S. Guo, N. Tao, J. J. Gooding, and M. N. Paddon-Row, *Single molecular switches: Electrochemical gating of a single anthraquinone-based norbornylogous bridge molecule,* J. Phys. Chem. C. **116**, 21093 (2012).

[13] M. Baghernejad, X. Zhao, K. Baruël Ørnsø, M. Füeg, P. Moreno-García, A. V. Rudnev, V. Kaliginedi, S. Vesztergom, C. Huang, W. Hong, P. Broekmann, T. Wandlowski, K. S. Thygesen, and M. R. Bryce, *Electrochemical control of single-molecule conductance by Fermi-level tuning and conjugation switching,* J. Am. Chem. Soc. **136**, 17922 (2014).

[14] E. H. van Dijk, D. J. T. Myles, M. H. van der Veen, and J. C. Hummelen, *Synthesis and properties of an anthraquinone-based redox switch for molecular electronics,* Org. Lett. **8**, 2333 (2006).

[15] T. Markussen, J. Schiötz, and K. S. Thygesen, *Electrochemical control of quantum interference in anthraquinone-based molecular switches,* J. Chem. Phys. **132**, 224104 (2010).

[16] V. M. Garcia-Suarez, C. J. Lambert, D. Z. Manrique, and T. Wandlowski, *Redox control of thermopower and figure of merit in phase-coherent molecular wires,* Nanotechnology **25**, 205402 (2014).

[17] C. M. Guedon, H. Valkenier, T. Markussen, K. S. Thygesen, J. C. Hummelen, and S. J. van der Molen, *Observation of quantum interference in molecular charge transport,* Nat. Nano. **7**, 305 (2012).

[18] D. Fracasso, H. Valkenier, J. C. Hummelen, G. C. Solomon, and R. C. Chiechi, *Evidence for quantum interference in SAMs of arylethynylene thiolates in tunneling junctions with Eutectic Ga-In (EGaIn) top-contacts,* J. Am. Chem. Soc. **133**, 9556 (2011).

[19] V. Kaliginedi, P. Moreno-García, H. Valkenier, W. Hong, V. M. García-Suárez, P. Buiter, J. L. H. Otten, J. C. Hummelen, C. J. Lambert, and T. Wandlowski, *Correlations between molecular structure and single-junction conductance: A case study with oligo(phenylene-ethynylene)-type wires,* J. Am. Chem. Soc. **134**, 5262 (2012).

[20] D. R. Strachan, D. E. Smith, D. E. Johnston, T. H. Park, M. J. Therien, D. A. Bonnell, and A. T. Johnson, *Controlled fabrication of nanogaps in ambient environment for molecular electronics,* Appl. Phys. Lett. **86**, 043109 (2005).

[21] K. O'Neill, E. A. Osorio, and H. S. J. van der Zant, *Self-breaking in planar few-atom Au constrictions for nanometer-spaced electrodes,* Appl. Phys. Lett. **90**, 133109 (2007).

[22] C. W. J. Beenakker, *Theory of Coulomb-blockade oscillations in the conductance of a quantum dot,* Phys. Rev. B **44**, 1646 (1991).

[23] J. C. Cuevas and E. Scheer, *Molecular Electronics: An Introduction to Theory and Experiment* (World Scientific Publishing Company, 2010).

[24] D. Goldhaber-Gordon, H. Shtrikman, D. Mahalu, D. Abusch-Magder, U. Meirav, and M. A. Kastner, *Kondo effect in a single-electron transistor,* Nature **391**, 156 (1998).

[25] H. Valkenier, C. M. Guedon, T. Markussen, K. S. Thygesen, S. J. van der Molen, and J. C. Hummelen, *Cross-conjugation and quantum interference: a general correlation?* Phys. Chem. Chem. Phys. **16**, 653 (2014).

[26] M. Strange, J. S. Seldenthuis, C. J. O. Verzijl, J. M. Thijssen, and G. C. Solomon, *Interference enhanced thermoelectricity in quinoid type structures,* J. Chem. Phys. **142**, 084703 (2015).

[27] K. Ohno, *Some remarks on the Pariser-Parr-Pople method,* Theor. Chim. Acta **2**, 219 (1964).

[28] J. Enkovaara, C. Rostgaard, J. J. Mortensen, J. Chen, M. Dułak, L. Ferrighi, J. Gavnholt, C. Glinsvad, V. Haikola, H. A. Hansen, H. H. Kristoffersen, M. Kuisma, A. H. Larsen, L. Lehtovaara, M. Ljungberg, O. Lopez-Acevedo, P. G. Moses, J. Ojanen, T. Olsen, V. Petzold, N. A. Romero, J. Stausholm, M. Strange, G. A. Tritsaris, M. Vanin, M. Walter, B. Hammer, H. Häkkinen, G. K. H. Madsen, R. M. Nieminen, J. K. Nørskov, M. Puska, T. T. Rantala, J. Schiøtz, K. S. Thygesen, and K. W. Jacobsen, *Electronic structure calculations with GPAW: a real-space implementation of the projector augmented-wave method,* J. Phys. Condens. Mat. **22**, 253202 (2010).

[29] K. S. Thygesen and A. Rubio, *Conserving GW scheme for nonequilibrium quantum transport in molecular contacts,* Phys. Rev. B **77**, 115333 (2008).

[30] M. Strange, C. Rostgaard, H. Häkkinen, and K. S. Thygesen, *Self-consistent GW calculations of electronic transport in thiol- and amine-linked molecular junctions,* Phys. Rev. B **83**, 115108 (2011).

[31] B. Roos and P. N. Skancke, *Semi-empirical parameters in π-electron systems,* Acta Chem. Scand. **21**, 233 (1967).

[32] K. G. L. Pedersen, *Theoretical Investigations Regarding Single Molecules: Neoclassical Valence Bond Theory, Quantum Transport, Quantum Interference, Kondo Effect, and Electron Pumping,* Ph.D. thesis, University of Copenhagen (2013).

[33] H. Ishii, K. Sugiyama, E. Ito, and K. Seki, *Energy level alignment and interfacial electronic structures at organic/metal and organic/organic interfaces,* Adv. Mater. **11**, 605 (1999).

[34] G. Begemann, S. Koller, M. Grifoni, and J. Paaske, *Inelastic cotunneling in quantum dots and molecules with weakly broken degeneracies,* Phys. Rev. B **82**, 045316 (2010).

[35] G. Barcza, W. Barford, F. Gebhard, and O. Legeza, *Excited states in polydiacetylene chains: A density matrix renormalization group study,* Phys. Rev. B **87**, 245116 (2013).

[36] K. Kaasbjerg and K. Flensberg, *Strong polarization-induced reduction of addition energies in single-molecule nanojunctions,* Nano Lett. **8**, 3809 (2008).

4

SPIN EXCITATIONS IN AN ALL-ORGANIC DOUBLE QUANTUM DOT MOLECULE

We realize a strongly coupled double quantum dot in a single all-organic molecule by introducing a non-conjugated bridge in between two identical conjugated moieties. Spin-1/2 Kondo and Kondo-enhanced low-energy excitations for respectively the odd and even electron occupation are observed in off-resonant transport. The ground state in the even occupation can be the singlet or the triplet state varying between samples. This observation suggests that both anti-ferromagnetic and ferromagnetic interactions between spins are of the same order of magnitude.

This chapter has been published in Physical Review B **94**, 165414 (2016) [1].

4.1. INTRODUCTION

Electron transport through double quantum dots made it possible to investigate new avenues of physics, such as the study of Kondo effects beyond the single-impurity Anderson model[2] and the realization of qubits[3]. Experimental systems encompass coupled semiconductor[4], graphene[5] and carbon nanotube[6] quantum dots and quantum dots built from atom pairs[7]. For single molecules, electron transport through an organic double quantum dot (DQD) molecule has not been studied to the same extend despite the fact that the energy scales of its electronic states are generally larger than in its counterparts, therefore relaxing the requirements for millikelvin temperatures for operation. Furthermore, the use of organic atoms like carbon and oxygen is expected to result in small spin-orbit coupling and no net nuclear spins on the molecules. This suggest that an all organic DQD molecule can potentially be a model system for the study of spin interactions that can be chemically tuned.[8]

To study transport in an organic DQD molecule, we use a 9,10-dihydroanthracene core with acetyl-protected sulfur anchoring groups connected by spacers[9](see figure 4.1a; named AH from now on). The conjugation of AH is broken due to the sp^3 hybridization of the two carbon atoms in the center of the 9,10-dihydroanthracene core. This results in AH being made up of two conjugated halves (dark green in figure 4.1a) connected by a non-conjugated bridge (red in figure 4.1a). This peculiar electronic structure results in a decreased conductance[10] and a higher energy UV-VIS absorption threshold[11] compared to the fully conjugated version of the molecule. The electronic structure of AH also results in negative differential conductance in electron transport[12], which is explained by a two-level model formed by the broken conjugation. Past research has thus shown that the broken conjugation influences the electronic structure and transport, suggesting that it may be regarded as a molecular DQD. In this paper, we explore this possibility by using low-temperature transport spectroscopy measurements in a three-terminal configuration.

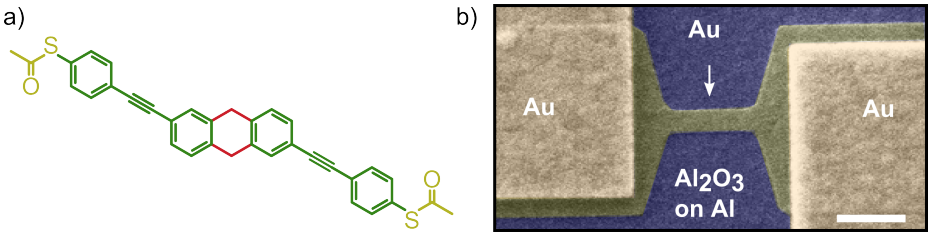

Figure 4.1: Molecule and setup. a) 9,10-dihydroanthracene (AH) with thiolated spacers. The dark green parts are the conjugated halves and the red colored part in the middle is the non-conjugated bridge. The yellowish colored parts at the end of the molecule are the anchoring groups. b) False-colored scanning electron microscopy image of a junction before electromigration. The purple area is the aluminum oxide surrounding the aluminum gate electrode underneath it. The darker yellow area is the 10 nm thick gold nanowire. Yellow areas correspond to the thicker leads, which are connected to wire bond pads. The white bar at the bottom has a length of 250 nm.

4.2. MEASUREMENTS

To form a gold-molecule-gold junction, we employ three-terminal electromigration junctions (figure 4.1b). A silicon/silicon oxide substrate is used, on top of which an aluminum gate is deposited by e-beam evaporation. Under a pure oxygen atmosphere, the aluminum is oxidized to create an electrically insulating layer surrounding the gate terminal. On top of the gate a 12 nm thick, 100 nm wide gold nanowire is subsequently deposited, which is connected with 100 nm thick Au leads to bond pads. To create the nano-gap the thin wire is controllably electromigrated [13] at room-temperature in a solution of dichloromethane with 0.5 mM AH to a resistance of the order of 5 KΩ. After this the wire is let to self-brake [14] to avoid the formation of spurious gold nano-particles when opening a gap in the wire to form the junction. When junction resistances are of the order of 1 MΩ, the sample chamber is pumped and cooled to cryogenic temperatures. The three-terminal geometry of these junctions makes it possible to measure the current (I) as a function of bias (V) and gate (V_g) voltages. Furthermore, with the help of a 1K-pot, heater resistor and a superconducting magnet, temperature and magnetic-field dependent measurements can be performed.

Figure 4.2a shows a differential conductance map of a junction (S1) prepared as described above. A single-electron tunneling (SET) regime is present around $V_g = 1$ V, marked by the dashed lines. The SET edges of the left charge state are visible; the edges of the right charge state are, however, suppressed. We first focus on the left charge state in figure 4.2a. It shows a pronounced gate-dependent zero-bias peak. The peak splits as a function of magnetic field and its height decays exponentially as a function of temperature (see in the appendix (section 4.4)). This behavior suggests spin-1/2 Kondo physics to be the origin of the zero-bias peak; the g-factor determined from the magnetic field dependent data is $g \sim 2.6$, which matches with values observed for single molecules[15]. The presence of a spin-1/2 Kondo peak indicates an uneven electron occupation for the left charge state.

When the gate voltage in figure 4.2a is increased past $V_g = 1$ V, an electron is added to the molecule. Instead of a zero-bias peak, a broader peak appears with a suppression around zero bias. Figure 4.3a shows the temperature dependence of this feature. With increasing temperature the suppression is lifted and a single broad peak remains above $T = 5$ K. Increasing the temperature even further results in a decrease in the height of the broad peak. This is seen more clearly in figure 4.3b, which shows the zero-bias conductance at $V_g = 3$ V as a function of temperature. This temperature dependence resembles a two-stage Kondo process[16], which can be caused by the full screening of a triplet[17] or a nearly degenerate singlet/triplet state[18]. These scenario's are further supported by the fact that in this charge state there should be an even number of electrons on the molecule, considering the odd occupation of the adjacent charge state to the left.

The magnetic field dependence in figure 4.3c shows that the suppression is lifted as a function of increasing magnetic field. This observation matches a singlet ground

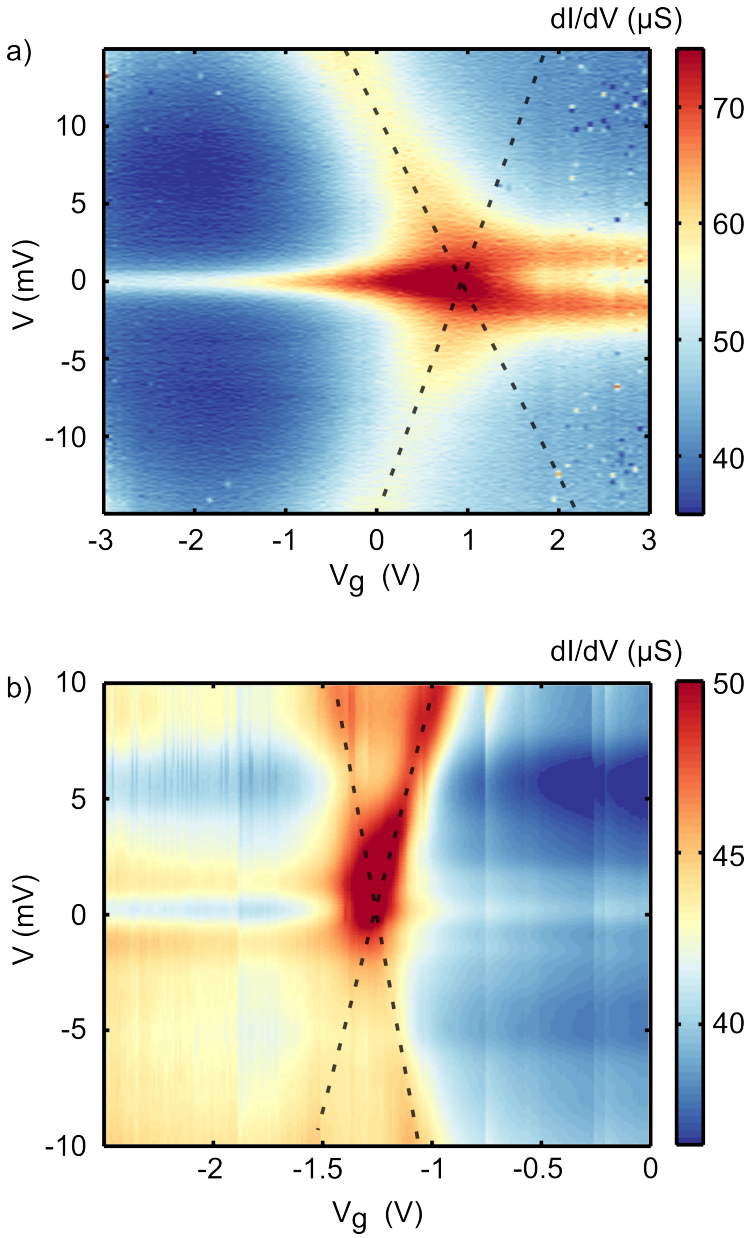

Figure 4.2: Differential conductance map as a function of bias (V) and gate (V_g) voltage of electromigration junction S1 (a) (T = 2.0 K) and junction S2 (b) (T = 2.0 K). Dashed lines show the SET edges. In a) a zero-bias peak is present in the left charge state and an excitation at a few meV in the right charge state. In b) a weak zero-bias peak (white line, see figure 4.10 in the appendix for a linecut) is present in the right charge state and an excitation of a few meV in the left one.

state ($S = 0$), because in case of a triplet ground state the excited states would move up in energy when increasing the magnetic field. Taking all information together, we assign the feature in the right charge state to two spins that interact anti-ferro magnetically; the ground state is a singlet and the peak at finite bias in dI/dV is caused by the singlet to triplet excitation. Using a Heisenberg hamiltonian $\mathbf{H} = -J\mathbf{S_1} \cdot \mathbf{S_2}$, the exchange coupling (J) can be determined from the figure, $J = -0.7$ meV. It is also interesting to note that when the suppression is lifted (when the singlet and triplet state are brought into degeneracy), the peak full width half maximum (FWHM) is larger than the spin-1/2 Kondo FWHM in the adjacent charge state at the same temperature. This matches other observations where a Kondo resonance caused by a singlet-triplet degeneracy has a larger FWHM than the one of the spin-1/2 Kondo[19].

Figure 4.2b shows another sample (S2) which has two charge states separated by a SET regime around $V_g = -1.3$ V (marked by the dashed lines). However, in this sample a zero-bias peak is present in the right charge state. Temperature and magnetic field dependent data point again to a spin-1/2 Kondo origin and thus suggest an uneven occupation of the molecule in this charge state (see appendix). Going to the left charge state by removing an electron from the molecule results in the appearance of a low-bias excitation. Figure 4.3d and e show the temperature dependence and figure 4.3f shows the magnetic-field dependence of this low-bias feature. A strong dependence on temperature is seen, suggesting Kondo correlations to play a role. Furthermore, the magnetic field dependence shows that the excitation energy shifts outwards to higher energies with increasing magnetic field. The presence of an even number of electrons on the molecule and the magnetic field and temperature dependences suggest a triplet ($S = 1$) ground state with a Kondo enhanced excitation to the singlet state (the exchange coupling J is +0.5 meV and ferro-magnetic)[19]. Sample S2 therefore has two differences compared to sample S1; the ground state in the even charge state is a triplet instead of a singlet state and the spin-1/2 Kondo effect is found to the right of an even charge state with low-bias features instead of to the left of such a state.

The pattern of spin-1/2 Kondo physics in one charge state and a low-bias feature due to the excitation between the singlet and triplet in a neighboring charge state has been seen in eight samples (see appendix). Table 4.1 shows the addition energy (U_{add}), the level broadening of the SET edge (Γ), the magnitude and sign of the exchange coupling (J) of the eight samples (for an overview of all parameters used in this text see the appendix). It can be seen that the addition energies are relatively small compared to those of molecules in gas phase. This may in part be due to the small energy difference between the HOMO and HOMO-1 (see discussion), but renormalization of the energy levels (image charge effects associated with the gate and electrodes) may also play a role[20–22]. The level broadening is smaller than the addition energy, but still of the same order explaining why Kondo correlations can be seen in the measurements. The magnitude of the coupling between the spins ($|J|$) ranges from approximately degenerate up to 5 meV. The sign of J has been determined for

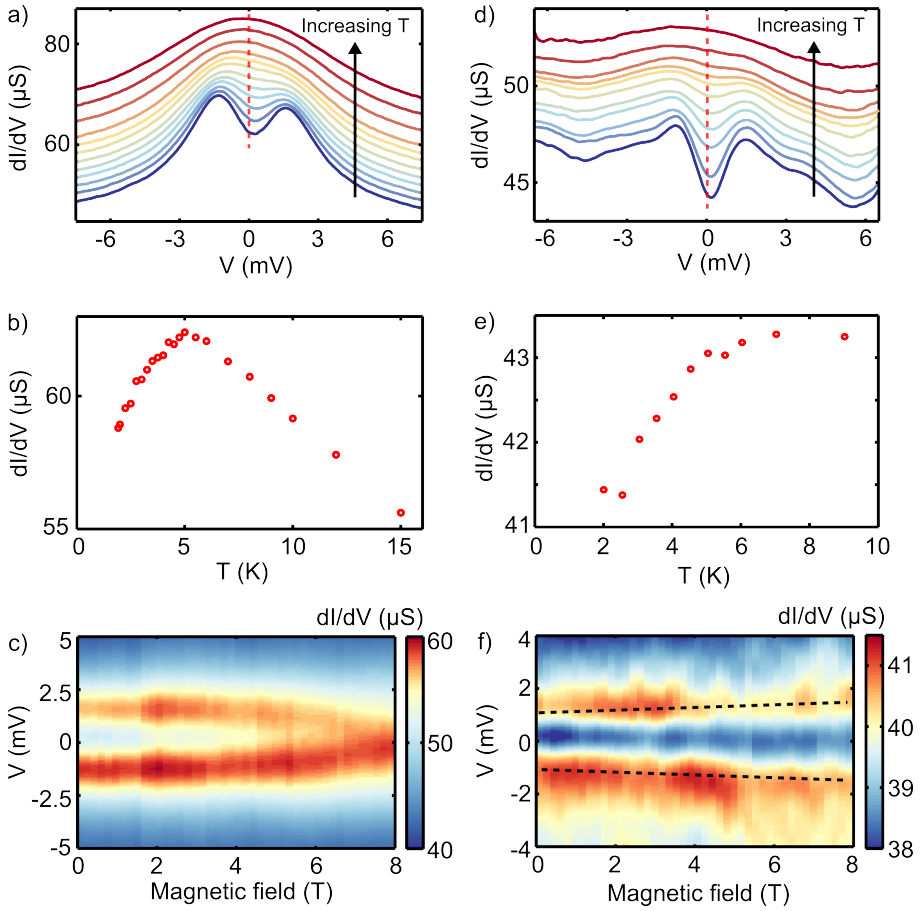

Figure 4.3: Temperature and magnetic field dependence of low-bias features in the even charge state for sample S1 (a,b,c) and S2 (d,e,f). a) Temperature dependence of the differential conductance at $V_g = 3\ V$. The individual curves are taken at a temperature of 1.9, 2.5, 3.0, 3.5, 4.0, 4.5, 5.0, 5.5, 6.0, 7.0, 8.0 and 9.0 K and are off-set from each other. The red dashed line is the zero-bias conductance plotted in panel b). b) Zero-bias conductance as a function of temperature. c) Magnetic-field dependence of the low-bias feature in the right charge state ($V_g = 3$ V, $T = 2$ K). d,e,f) show the same measurements as a,b,c) with curves taken at 1.95, 2.5, 3.0, 3.5, 4.0, 4.5, 5.0, 5.5, 6.0, 7.0 and 9.0 K for sample S2. In d,e) $V_g = -1.9$ V and in f) $T = 2$ K, $V_g = -1.9$ V.

Table 4.1: Parameters extracted from the differential conductance maps (see also the appendix). Some values could not be determined; in those cases a upper or lower limit is given. U_{add} is the addition energy of the specified charge state with an estimated error of ±5 meV, Γ is the level broadening (±2 meV) and $|J|$ the magnitude of the exchange coupling (±0.2 meV). The last column displays the character of the coupling between the two spins, which can be anti-ferromagnetic (AF), ferromagnetic (F), degenerate (degen.) or not determined (not det.) due to the absence of magnetic field dependent data.

	U_{add} (meV)	Γ (meV)	|J| (meV)	coupling
S1	49 (N=-1)	11	0.7	AF
S2	>63 (N=-2)	5.5	0.5	F
S3	50 (N=-2)	9	1.4	not det.
S4	73 (N=-2)	5	3	not det.
S5	37 (N=-2)	8	1.2	not det.
S6	58 (N=-2)	10	<0.2	degen.
S7	>53 (N=-1)	18	<0.5	degen.
S8	>50 (N=-2)	40	3.5	not det.

2 samples (S1 and S2, anti-ferromagnetic and ferro-magnetic respectively). Furthermore for sample S6 and S7 the singlet and triplet states are approximately degenerate (see figure 4.10 in the appendix). For 4 samples magnetic field data has not been recorded, so the sign of J could not be determined.

4.3. DISCUSSION

The observation of low-bias features in a charge state with an even occupation suggests that the singlet to triplet energy difference for the two highest lying electrons is small. For molecules this may seem counter intuitive due to their small size, however, when inspecting the density functional calculations (DFT)[12] of the orbitals of AH (figure 4.4a) it can be seen that the HOMO and HOMO-1 are nearly degenerate in energy. Analogous to the prototypical hydrogen molecule, these nearly degenerate orbitals are formed by the hybridization of both conjugated halves of AH and thus show symmetric and anti-symmetric orbital wave-functions. The level splitting (ΔE) of the HOMO and HOMO-1 is of the order of 10 to 50 meV, depending on the geometry of the molecule (see the supplementary information of Perrin *et al.* [12]), which is significantly smaller than in fully conjugated molecules. The level splitting gives an estimate for the internal coupling (τ) between the two conjugated halves of the molecule by using $\tau = \Delta E/2$. This results in the coupling between the conjugated moieties to be between 5 to 25 meV.

We attribute the features in the measurements to the sequential oxidation of AH from a N = -1 occupation down to N = -3 occupation (where N is the difference in electrons with the neutrally charged molecule). Oxidation of AH is supported by DFT calculations which predict the Fermi energy to lie close to the HOMO orbital. Furthermore, multiple reduction of AH is unlikely as the LUMO and LUMO+1 are not

close in energy. This leads us to the following features in transport (figure 4.4b) and the electronic states (figure 4.4c) as a function of electron occupation of the HOMO and HOMO-1 in AH. In the N = -3 state, a single unpaired electron is present in the HOMO-1, which results in spin-1/2 Kondo in transport. Adding an electron results in the formation of a singlet or triplet state. Depending on the ground state, the excitation visible in the N = -2 charge state is the triplet or singlet respectively (this will be discussed further on). Addition of a second electron results in a pair of electrons in the HOMO-1 and a free unpaired spin in the HOMO; spin-1/2 Kondo reappears. No samples were measured that showed the three consecutive charge states shown in figure 4.4b, however, all eight samples show the N = -2 charge state. Next to the N = -2 charge state samples S1, S3, S7 and S8 show the N = -3 state and samples S2, S5 and S6 show the N = -1 charge state.

The fact that both the singlet and triplet ground states are observed at $B = 0$ T, indicates that the ferromagnetic J_F and anti-ferromagnetic J_{AF} terms contribute almost equally to the total exchange coupling $J = J_F - J_{AF}$. To first order[23], J_F is governed by the Coulomb exchange and J_{AF} by the kinetic exchange. The kinetic exchange can be approximated by the Hubbard model, for $t < U$, $J_{AF} = 4t^2/U$, where U is the on-site Coulomb interaction and t is the inter-site hopping. Using the addition energy as an approximation for the on-site Coulomb interaction $U \approx \Delta E = 40 - 80$ meV and using $t \approx \tau = 10$ meV as calculated from DFT, one finds $J_{AF} = 5 - 10$ meV. A singlet ground state can thus be explained by considering only this term. However, the appearance of the triplet ground state suggests that the Coulomb exchange should also be taken into account. This can be intuitively understood from the fact that AH is approximately 2 nm long, much smaller than for other double quantum dot implementations. Therefore, electrons are closer together thereby increasing Coulomb effects and promoting ferromagnetic coupling (Hund's rule).

Further indications for a nearly degenerate HOMO and HOMO-1 can be seen in the off-resonant transport in the N = -1 and N = -3 charge states of S2 and S7 respectively. Here, in addition to the spin-1/2 Kondo resonance, low-bias excitations are visible. These can be related to the excitation of an electron from the HOMO-1 to the HOMO[24]. In both samples the excitation energy changes as a function of gate voltage; a possible mechanism for this could be differential gating[25] of the two conjugated halves of AH that form the HOMO and HOMO-1. If AH is situated asymmetrically in between the electrodes, the left conjugated half of AH can exhibit a slightly different gate coupling than the right conjugated half. It would thus modify the energy splitting (ΔE) between the HOMO and HOMO-1, leading to low-lying gate dependent excitations as observed in the experiment.

The delocalization and splitting of the HOMO and HOMO-1 and the observation of Kondo effects, suggest that the measurements show a DQD that has a strong internal coupling (τ) and is well coupled to the leads (Γ). To further probe the spin states in AH and study spin relaxation mechanisms, it is beneficial to significantly lower Γ and τ so that the spins on the two halves are localized more. This has been done in

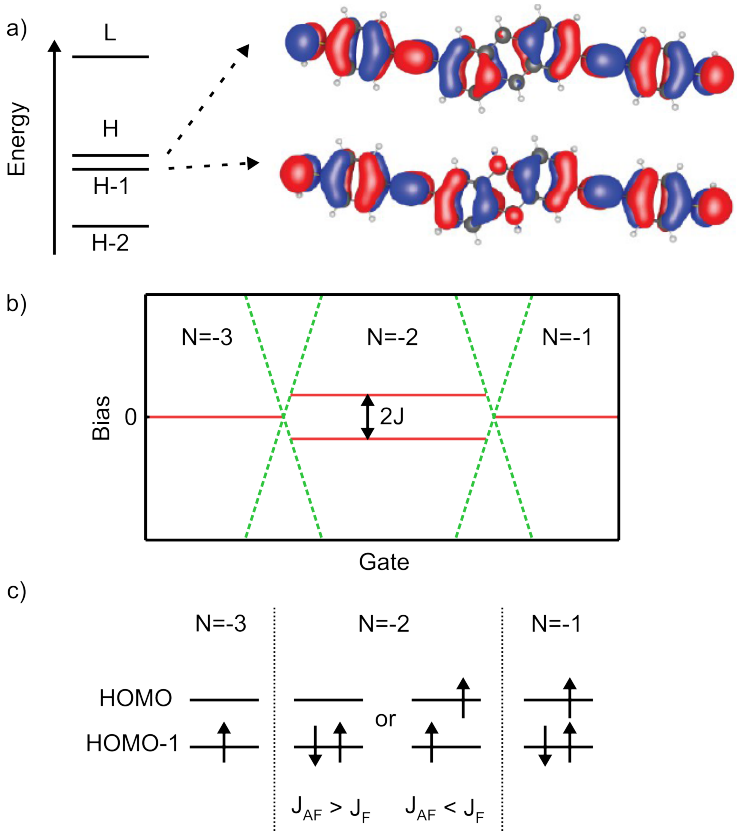

Figure 4.4: a) Energy spectrum of the AH molecular orbitals (not to scale); L stand for lowest unoccupied molecular orbital (LUMO) and H for highest occupied molecular orbital (HOMO). The isosurface of the nearly degenerate HOMO and HOMO-1 are shown next to it. It can be seen that the HOMO-1 is symmetric whereas the HOMO is anti-symmetric with respect to the molecule. b) Schematic of the transport features in AH at low temperature and $B = 0$ T. Green dashed lines are Coulomb edges; red lines represent higher-order transport features in the Coulomb blockade region, i.e, zero-bias peaks associated with $S = 1/2$ Kondo or inelastic tunneling excitations at finite bias. c) Orbital filling of the nearly degenerate HOMO and HOMO-1. In the N = -2 charge state two ground states are possible depending on the exchange coupling.

semiconductor[26] and carbon nanotube[27] DQD's, where with Pauli spin blockade the spin dynamics and relaxation mechanisms have been studied. This localization can be achieved by using chemical synthesis to decrease the coupling to the leads[28] or the intramolecular coupling of the molecular DQD by using for example a larger non-conjugated bridge[8] or a rotation of the two halves[29].

In conclusion, we have shown transport spectroscopy of a strongly coupled double quantum dot molecule formed within a molecule with a non-conjugated bridge in the middle. A pattern of consecutive charge states has been identified which shows spin-1/2 Kondo, singlet-triplet states, spin-1/2 Kondo as a function of increasing electron occupation. This pattern can be explained with the formation of a pair of nearly degenerate orbitals due to the broken conjugation. In the even charge state, transport features are observed which indicate the presence of singlet and triplet states. The spin ground state varies from sample to sample, indicating that the anti-ferromagnetic and ferromagnetic interactions are of the same order of magnitude in AH. This suggests that Coulomb exchange plays a significant role as can be expected from a double quantum dot the size of a single molecule.

4.4. APPENDIX

LIST OF PARAMETERS USED IN THE MAIN TEXT

Table 4.2 lists the parameters used in the main text. The following two parameters are used to describe the properties of the molecule (in this case AH).
ΔE **(level splitting)**: The energy difference between the HOMO and HOMO-1 orbital is calculated (with DFT) to be of the order of 10-50 meV. The level splitting is related to the internal coupling (τ), by $\Delta E = 2\tau$. A stronger internal coupling results in a larger level splitting between the HOMO and HOMO-1.
τ **(internal coupling)**: Coupling (electron transfer) between the two conjugated halves of AH. Their coupling to each other results in the delocalized HOMO and HOMO-1 orbitals, analogous to the bonding and anti-bonding orbitals of the hydrogen molecule. As already described τ is related to the level splitting of the HOMO and HOMO-1 by $\tau = \Delta E/2$.

The following parameters are used to describe electron transport through the molecular junction.
Γ **(level broadening)**: Caused by electronic coupling of the molecule to the source and drain electrodes. Can be determined from the full width half maximum of the SET edge in a differential conductance map. Gives information about the broadening of the molecular orbitals on the molecule and the residence time of an electron on the molecule.
U_{add} **(addition energy)**: The energy needed to add an electron from the leads onto the molecule. It has a quantum mechanical component in form of the level splitting and an electrostatic component in form of the charging energy. It can be deduced from the height and width of the off-resonant transport diamonds in the differential conductance maps.

Parameters related to model hamiltonians used in the main text.
J **(Exchange coupling)**: Defined by the Heisenberg hamiltonian $\mathbf{H} = -J\mathbf{S_1} \cdot \mathbf{S_2}$. The magnitude and sign of J describe the interaction strength between two spins $\mathbf{S_1}$ and $\mathbf{S_2}$. $J > 0$ represents a ferromagnetic exchange and $J < 0$ an anti-ferromagnetic exchange.
U **(On-site interaction)**: Energy needed to place two electrons on the same site in the Hubbard model. To first order it can be related to the electrostatic component of the addition energy $U_{add} \approx U$.
t **(Hopping)**: Used in the Hubbard model as the kinetic energy. Determines the magnitude of electron transfer between two sites. To first order it can be approximated by the internal coupling $\tau \approx t$.

KONDO EFFECT SAMPLE S1

The left charge state of figure 4.2a in the main text shows a zero bias peak (ZBP). This ZBP is further investigated in figure 4.5. Panel a) shows the evolution of the ZBP as

Symbol	Definition	Used to describe:
ΔE	level splitting	molecule
τ	internal coupling	
Γ	level broadening	molecular junction
U_{add}	addition energy	
J	exchange coupling	model hamiltonians
U	on-site interaction	
t	hopping	

Table 4.2: List of parameters used in the main text. Further explanation is given in the text. The units of all listed parameters is energy.

a function of magnetic field. The peak splits when a magnetic field is applied, with a splitting of $\Delta V = 2.4$ mV at B = 8 T. Assuming S = 1/2 this results in a g-factor of $g = \Delta V/2\mu_B B = 2.6$, which is comparable to other spin-1/2 Kondo systems found in molecules. Figure 4.5b and c show the evolution of the ZBP as a function of temperature. The peak broadens considerably as a function of increasing temperature and the peak height falls off non-linearly. Both observations are signatures of a spin-1/2 Kondo system. It is clear from the inset of 4.5c that the saturation limit ($T \ll T_k$) has not yet been reached, therefore fitting an empirical line-shape to the evolution of the peak height is difficult and a wide range of Kondo temperatures match the curve. Fits show a range of Kondo temperatures between 0.1 and 4 K following the data points. The final panel (4.5d) investigates the evolution of the peak width as a function of gate voltage. The full width at half maximum (FWHM) is determined for the ZBP at each gate voltage in the left charge state of figure 4.2a in the main text. The following formula was used to convert the FWHM of the ZBP to a Kondo temperature:

$$k_b T_k = \sqrt{(FWHM/2)^2 - (\pi k_b T)^2} \tag{4.1}$$

The red data points in figure 4.5d represent these temperatures. The blue line in the panel is a fit to the data using:

$$k_b T_K \approx \sqrt{\Gamma U_{add}} \exp(\pi \epsilon_0 (\epsilon_0 + U_{add})/(2\Gamma U_{add})) \tag{4.2}$$

It relates the location of the chemical potential (ϵ_0) to the Kondo temperature (T_k) as a function of the addition energy. The fit follows the data points nicely and assuming that at $V_g = 1$ V there is a charge degeneracy point (as suggested in the main text) results in an estimation of $U_{add} = 53$ meV and $\Gamma = 16$ meV. The coupling matches the coupling found in the main text.

KONDO EFFECT SAMPLE S2

The peak in the right charge state of figure 4.2b is further investigated in figure 4.6. Panel a) shows the magnetic field dependence of the differential conductance around

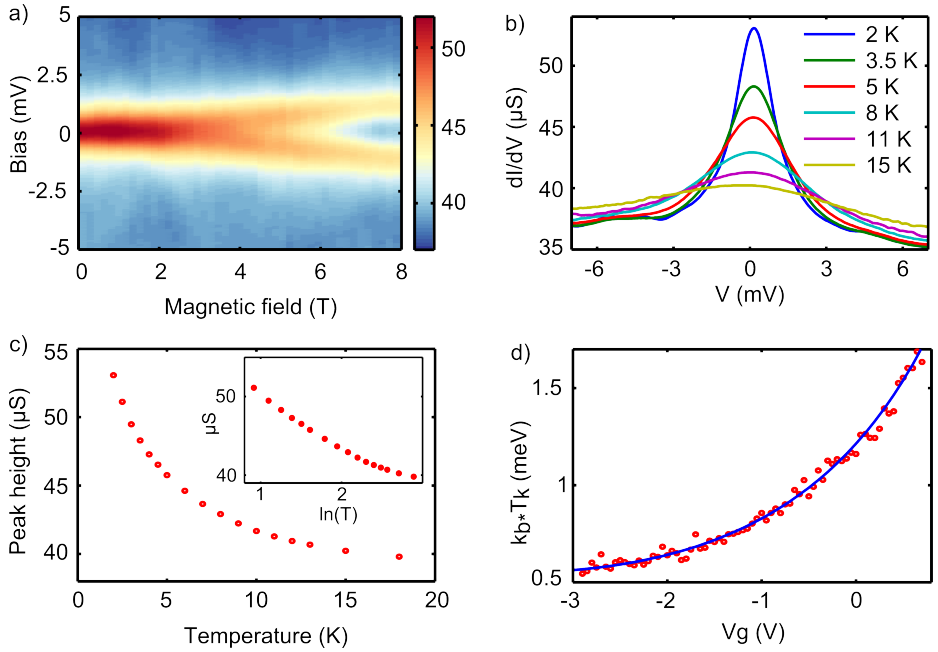

Figure 4.5: Investigation of the zero-bias peak of sample S1 (figure 4.2a in main text). a) Differential conductance map of the magnetic field dependence of the ZBP at $V_g = -2.5$ V, $T = 2$ K. b) Temperature dependence of the ZBP at $V_g = -2$ V. c) Peak height of the ZBP as a function of temperature on a linear scale. Inset shows the peak height dependence versus natural log of the temperature. d) Evolution of Kondo temperature determined with equation 4.1 plotted versus gate voltage. The red dots are data points and the blue line is a fit to equation 4.2.

zero bias. As a function of increasing magnetic field the zero-bias peak starts to split. At $B = 8$ T the splitting is $\Delta V = 2.96$ meV; assuming the origin of ZBP to be from a spin-1/2 Kondo, a g-factor of $g = \Delta V / 2\mu_B B = 3.2$ can be determined. Panel b) shows the temperature dependence of the differential conductance traces. With increasing temperature, the height of the ZBP decreases. The decrease is exponential-like as can be seen in panel c) where the peak maximum is plotted against the temperature. The inset shows the peak maximum as a function of ln(T). In this plot the data points show an approximately straight line, suggesting an exponential relationship between the peak height of the ZBP and temperature. The splitting of the ZBP as a function of magnetic field and the exponential decrease of the peak height, are consistent with a spin-1/2 Kondo system.

EXCITATION SAMPLE S2

Figure 4.7 shows the magnetic field dependence of the left charge state of sample S2. In the left panel a differential conductance map is shown of the magnetic field

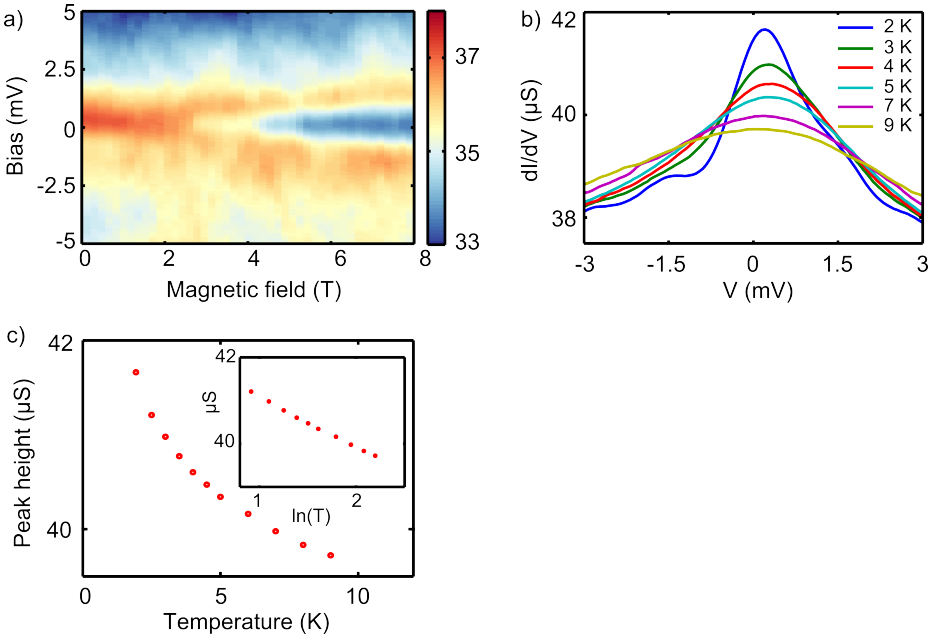

Figure 4.6: Investigation of the zero-bias peak of sample S2 (figure 4.2b in main text) in the main text. a) Differential conductance map of the magnetic field dependence of the ZBP at $V_g = 1.2\ V$, $T = 2\ K$. b) Temperature dependence of the ZBP peak at $V_g = 0.25\ V$. c) Peak height of the ZBP as a function of temperature on a linear scale. Inset shows the height dependence versus the natural log of temperature.

dependence of the low-bias excitation. The dots show the location of the minimum conduction as a function of magnetic field. For each magnetic field value the crosses mark the excitation energy defined as the inflexion point of the excitation. The difference between the minimum (dots) and excitation energy (crosses) is shown in the right panel for both positive and negative bias. The excitation energy clearly increases with increasing magnetic field. Performing a linear fit to the positive and negative excitation energies (black dashed lines), results in a magnetic field dependence of $\Delta E/B \approx 30$ μeV/T for positive bias and $\Delta E/B \approx 50$ μeV/T for negative bias.

STATISTICS

In total 132 junctions were electromigrated to form a gap. Of these, 40 % showed current-voltage traces (IV's), in which the conductance varies with gate voltage. Of these 53 junctions, 12 showed two or more charge states. 8 of the 12 junctions also exhibited a pattern of a zero-bias peak in one charge state and a broader peak with or without a suppression in the charge state next to it. These 8 junctions display transport features consistent with a double quantum dot. This suggests that AH acting as a double quantum dot is not related to a rare geometric (electronic) configuration in

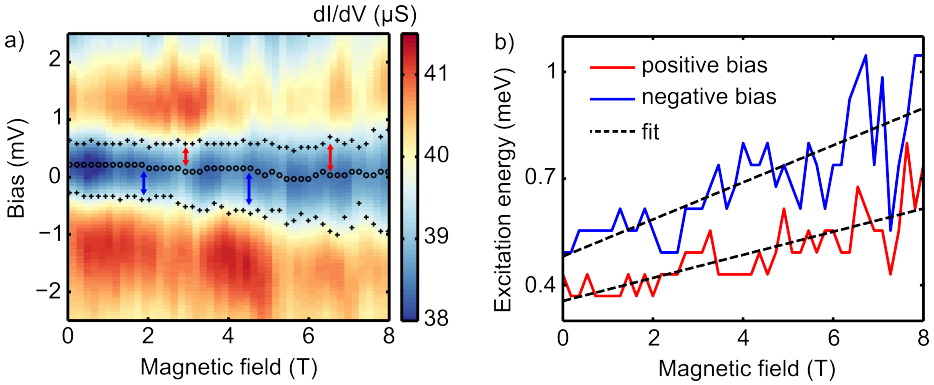

Figure 4.7: Investigation of the excitations in the even charge state of sample S2. a) Differential conductance map ($V_g = -1.4$ V, $T = 2$ K) as a function of magnetic field. The dots are at the minimum in conductance; the crosses at the inflection point for the negative and positive bias excitation. b) Red and blue lines are the excitation energy as a function of magnetic field (the difference as marked by the arrows in a)). The dashed black lines are linear fits to the excitation energies.

between the electrodes, but is an inherent property of AH. This is further supported upon considering that the statistics also takes into account junctions with AH either coupled too strongly or too weakly to be in the Kondo regime ($\Gamma \lesssim U$) to identify the low-bias features in the off-resonant transport. It also takes into account situations when the gate coupling is too low to observe multiple charge states.

CONDUCTANCE MAPS S3 TO S8

The samples showing DQD transport features are numbered S1 to S8. S1 and S2 are discussed in the main text; S3 to S8 are shown in figure 4.8. The zero-bias peaks have been identified as spin-1/2 Kondo using temperature and magnetic-field dependent measurements (except for S3, S4, S5 and S8, where the magnet was not available). In the charge state to the right a broad peak with or without a suppression is observed for samples S1, S3, S7, S8. In samples S2, S5 and S6, the charge state to the left has a broad peak with or without a suppression. In sample S4, the zero-bias peaks are not visible.

Comparing individual traces in figure 4.9 shows that the exact shape of the low-bias feature in the even occupation (4.9a) differs from sample to sample. The two main parameters that determine the line-shape are the singlet-triplet energy difference J and the FWHM of the singlet-triplet Kondo. When J is significantly smaller than the FWHM, one single peak is present. This can be seen in samples S6 and S7. It can also be seen that in S6 and S7 the spin-1/2 Kondo feature in the traces in the odd occupation charge state (4.9b) is slightly narrower than in the even charge state. When J increases a dip appears (with increasing J for S1, S2, S5, S3, S9) due to the singlet and triplet state not being degenerate any more.

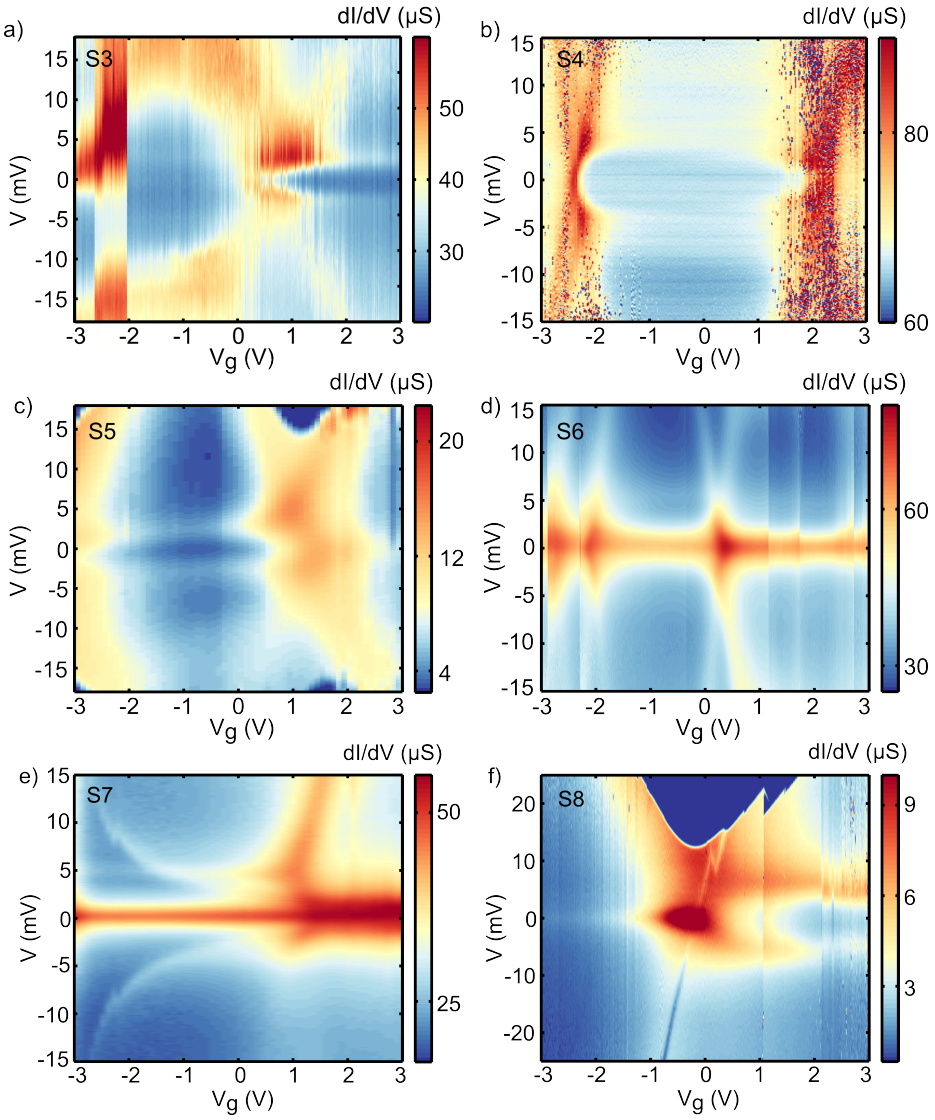

Figure 4.8: Differential conductance maps as a function of gate and bias voltage for six different samples. The measurement were taken at S3 ($T = 4$ K), S4 ($T = 2.4$ K), S5 ($T = 4.1$ K), S6 ($T = 2$ K), S7 ($T = 2$ K) and S8 ($T = 5$ K)

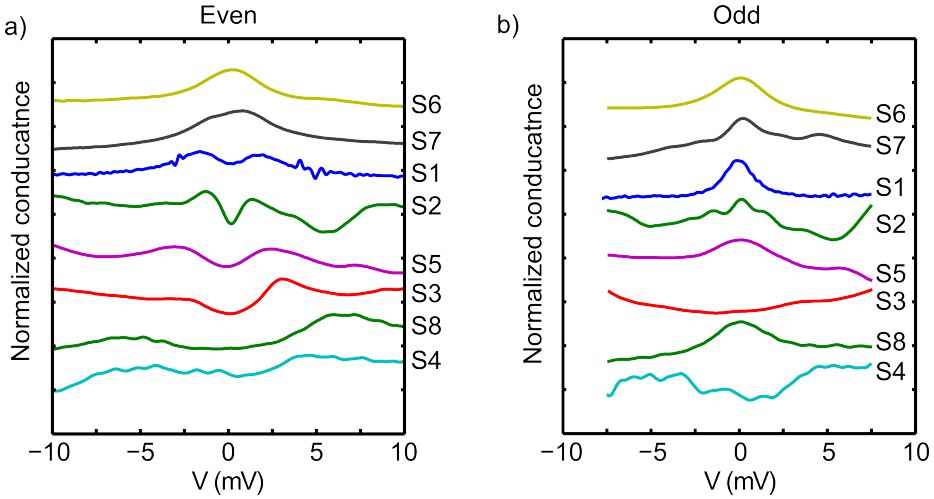

Figure 4.9: Selected differential conductance traces as a function of bias of all samples. a) Traces in the N=-2 charge state. The traces are taken at the maximum separation of singlet-triplet transition, except for S7 where it is taken at the maximum gate voltage. b) Traces in the N=-1 or N=-3 charge state. Traces are taken 10 meV away from the charge degeneracy point.

MAGNETIC FIELD DEPENDENCE OF S1, S2, S6 AND S7

For samples S1, S2, S6 and S7 the magnetic field dependence of the low-bias features in off-resonant transport are shown in figure 4.10. Each panel shows two magnetic-field dependent data plots. Each plot is from a different charge state. In the odd charge state a single peak is present at $B = 0$ T. When the magnetic field is increased, the peak height decreases and splits in two, as is expected for a system showing spin-1/2 Kondo.

Moving to the other charge state (for S1 and S7 this is adding an electron, for S2 and S6 an electron is removed) results in a low-bias feature with a different line-shape. S1 and S2 show a broad peak with a suppression, S6 and S7 show one broad peak. When applying a magnetic field the line-shapes evolve depending on the sample. For S1 the suppression is lifted and the peak narrows. For S2 the suppression gets slightly wider. In S6 the broad peaks gets even broader and S7 shows negligible evolution as a function of magnetic field.

The trends in these even charge states can be explained by a near singlet-triplet degeneracy. As already described in the main text, the magnetic field dependence of S1 can be explained with a spin-singlet ground state and an excited triplet state that lowers in energy as a function of increasing B-field. In sample S2 the ground state is the triplet state, with an excitation to the singlet state. This would explain the widening of the suppression with increasing magnetic field. In sample S6 the singlet and triplet state are nearly degenerate resulting in the absence of excitations at finite

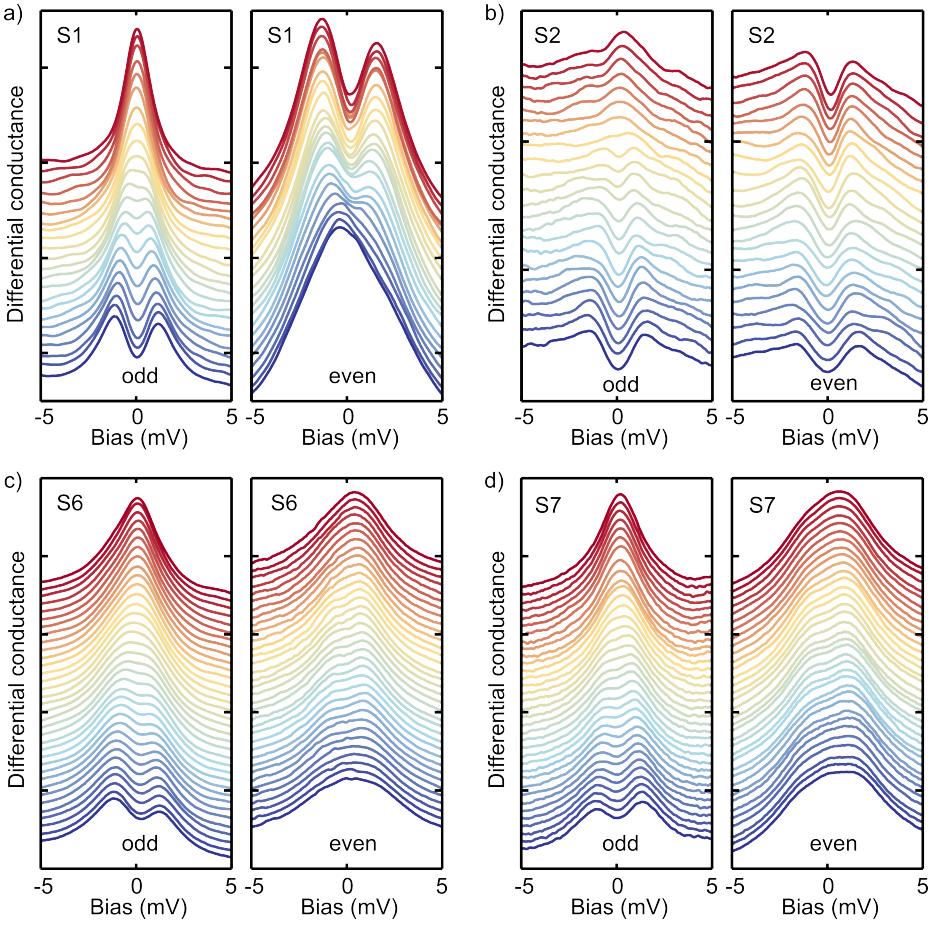

Figure 4.10: Differential conductance traces as a function of magnetic field for samples a) S1 (odd (V_g = −2.5 V, T = 2 K), even (V_g = 3 V, T = 2 K)), b) S2 (odd (V_g = 1.2 V, T = 2 K), even (V_g = −1.4 V, T = 2 K)), c) S6 (odd (V_g = 2.1 V, T = 2 K), even (V_g = −0.7 V, T = 2 K)), d) S7 (odd (V_g = −1.8 V, T = 2 K), even (V_g = 3 V, T = 2 K)). The red traces are for B = 0 T, moving down, the magnetic field increases linearly until B = 8 T for the blue trace. The charge state is noted at the bottom of each panel.

bias. The resulting peak is broader than the peak in the odd charge state. Applying a magnetic field broadens the peak, consistent with a degenerate singlet-triplet moving to a triplet ground state. Sample S7 does not show a clear evolution of the low-bias peak, however, it is clear that it does not behave as a spin-1/2 Kondo peak and that it is broader than the spin-1/2 peak in the odd charge state.

The measurements thus show that it is not necessarily clear what the spin ground-state of dihydroanthracene is in the even charge state. Signatures for both singlet and triplet ground state are seen as well as cases which are consistent with a singlet-triplet degeneracy.

REFERENCES

[1] M. Koole, J. C. Hummelen, and H. S. J. van der Zant, *Spin excitations in an all-organic double quantum dot molecule,* Phys. Rev. B **94**, 165414 (2016).

[2] H. Jeong, A. M. Chang, and M. R. Melloch, *The Kondo effect in an artificial quantum dot molecule,* Science **293**, 2221 (2001).

[3] R. Hanson, L. P. Kouwenhoven, J. R. Petta, S. Tarucha, and L. M. K. Vandersypen, *Spins in few-electron quantum dots,* Rev. Mod. Phys. **79**, 1217 (2007).

[4] W. G. van der Wiel, S. De Franceschi, J. M. Elzerman, T. Fujisawa, S. Tarucha, and L. P. Kouwenhoven, *Electron transport through double quantum dots,* Rev. Mod. Phys. **75**, 1 (2002).

[5] F. Molitor, S. Dröscher, J. Güttinger, A. Jacobsen, C. Stampfer, T. Ihn, and K. Ensslin, *Transport through graphene double dots,* Appl. Phys. Lett. **94**, 222107 (2009).

[6] N. Mason, M. J. Biercuk, and C. M. Marcus, *Local gate control of a carbon nanotube double quantum dot,* Science **303**, 655 (2004).

[7] B. Roche, E. Dupont-Ferrier, B. Voisin, M. Cobian, X. Jehl, R. Wacquez, M. Vinet, Y.-M. Niquet, and M. Sanquer, *Detection of a large valley-orbit splitting in silicon with two-donor spectroscopy,* Phys. Rev. Lett. **108**, 206812 (2012).

[8] C. A. Mujica-Martinez, P. Nalbach, and M. Thorwart, *Organic π-conjugated copolymers as molecular charge qubits,* Phys. Rev. Lett. **111**, 016802 (2013).

[9] D. Fracasso, H. Valkenier, J. C. Hummelen, G. C. Solomon, and R. C. Chiechi, *Evidence for quantum interference in SAMs of arylethynylene thiolates in tunneling junctions with Eutectic Ga-In (EGaIn) top-contacts,* J. Am. Chem. Soc. **133**, 9556 (2011).

[10] V. Kaliginedi, P. Moreno-García, H. Valkenier, W. Hong, V. M. García-Suárez, P. Buiter, J. L. H. Otten, J. C. Hummelen, C. J. Lambert, and T. Wandlowski, *Correlations between molecular structure and single-junction conductance: A case study with oligo(phenylene-ethynylene)-type wires,* J. Am. Chem. Soc. **134**, 5262 (2012).

[11] H. Valkenier, *Molecular Conductance: Synthesis, Self-Assembly, and Electrical Characterization of π-Conjugated Wires and Switches*, Ph.D. thesis, University of Groningen (2011).

[12] M. L. Perrin, R. Frisenda, M. Koole, J. S. Seldenthuis, G. A. Celis, H. Valkenier, J. C. Hummelen, N. Renaud, F. C. Grozema, J. M. Thijssen, D. Dulić, and H. S. J. van der Zant, *Large negative differential conductance in single-molecule break junctions,* Nat. Nano. **9**, 830 (2014).

[13] D. R. Strachan, D. E. Smith, D. E. Johnston, T.-H. Park, M. J. Therien, D. A. Bonnell, and A. T. Johnson, *Controlled fabrication of nanogaps in ambient environment for molecular electronics,* Appl. Phys. Lett. **86**, 043109 (2005).

[14] K. O'Neill, E. A. Osorio, and H. S. J. van der Zant, *Self-breaking in planar few-atom Au constrictions for nanometer-spaced electrodes,* Appl. Phys. Lett. **90**, 133109 (2007).

[15] L. Liu, K. Yang, Y. Jiang, B. Song, W. Xiao, S. Song, S. Du, M. Ouyang, W. A. Hofer, A. H. Castro Neto, and H.-J. Gao, *Revealing the atomic site-dependent g factor within a single magnetic molecule via the extended Kondo effect,* Phys. Rev. Lett. **114**, 126601 (2015).

[16] W. G. van der Wiel, S. De Franceschi, J. M. Elzerman, S. Tarucha, L. P. Kouwenhoven, J. Motohisa, F. Nakajima, and T. Fukui, *Two-stage Kondo effect in a quantum dot at a high magnetic field,* Phys. Rev. Lett. **88**, 126803 (2002).

[17] M. Pustilnik and L. I. Glazman, *Kondo effect in real quantum dots,* Phys. Rev. Lett. **87**, 216601 (2001).

[18] W. Hofstetter and H. Schoeller, *Quantum phase transition in a multilevel dot,* Phys. Rev. Lett. **88**, 016803 (2001).

[19] S. Sasaki, S. De Franceschi, J. M. Elzerman, W. G. van der Wiel, M. Eto, S. Tarucha, and L. P. Kouwenhoven, *Kondo effect in an integer-spin quantum dot,* Nature **405**, 764 (2000).

[20] K. Kaasbjerg and K. Flensberg, *Strong polarization-induced reduction of addition energies in single-molecule nanojunctions,* Nano Lett. **8**, 3809 (2008).

[21] M. L. Perrin, C. J. O. Verzijl, C. A. Martin, A. J. Shaikh, R. Eelkema, J. H. van Esch, J. M. van Ruitenbeek, J. M. Thijssen, H. S. J. van der Zant, and D. Dulić, *Large tunable image-charge effects in single-molecule junctions,* Nat. Nano. **8**, 282 (2013).

[22] S. Kubatkin, A. Danilov, M. Hjort, J. Cornil, J.-L. Bredas, N. Stuhr-Hansen, P. Hedegård, and T. Bjornholm, *Single-electron transistor of a single organic molecule with access to several redox states,* Nature **425**, 698 (2003).

[23] J.-P. Launey and M. Verdaguer, *Electrons in Molecules: From Basic Principles to Molecular Electronics* (Oxford University Press, 2014).

[24] G. Begemann, S. Koller, M. Grifoni, and J. Paaske, *Inelastic cotunneling in quantum dots and molecules with weakly broken degeneracies,* Phys. Rev. B **82**, 045316 (2010).

[25] E. A. Osorio, K. Moth-Poulsen, H. S. J. van der Zant, J. Paaske, P. Hedegård, K. Flensberg, J. Bendix, and T. Bjornholm, *Electrical manipulation of spin states in a single electrostatically gated transition-metal complex,* Nano Lett. **10**, 105 (2010).

[26] K. Ono, D. G. Austing, Y. Tokura, and S. Tarucha, *Current rectification by Pauli exclusion in a weakly coupled double quantum dot system,* Science **297**, 1313 (2002).

[27] H. O. H. Churchill, A. J. Bestwick, J. W. Harlow, F. Kuemmeth, D. Marcos, C. H. Stwertka, S. K. Watson, and C. M. Marcus, *Electron-nuclear interaction in* ^{13}C *nanotube double quantum dots,* Nat Phys **5**, 321 (2009).

[28] A. Danilov, S. Kubatkin, S. Kafanov, P. Hedegård, N. Stuhr-Hansen, K. Moth-Poulsen, and T. Bjørnholm, *Electronic transport in single molecule junctions: Control of the molecule-electrode coupling through intramolecular tunneling barriers,* Nano Lett. **8**, 1 (2008).

[29] L. Venkataraman, J. E. Klare, C. Nuckolls, M. S. Hybertsen, and M. L. Steigerwald, *Dependence of single-molecule junction conductance on molecular conformation,* Nature **442**, 904 (2006).

5

UNPAIRED SPINS IN π-EXTENDED TETRATHIAFULVALENE

A π-extended tetrathiafulvalene is studied in a three-terminal electromigration junction. Low-bias features are observed in off-resonant transport that point to the interaction of two unpaired spins. The low-bias features show strong gate dependence. These features can be explained by density functional calculations on the +2 charge state of the molecule. The calculations show a pair of nearly degenerate orbitals with a dissimilar spatial distribution which promotes differential gating.

We want to thank M.A. Herranz and N. Martín for the opportunity to measure the π-extended tetrathiafulvalene molecule.

5.1. INTRODUCTION

Quantum interference (QI) in charge transport through organic molecules has attracted significant attention due to its promise in applications regarding switching[1–4] or thermopower[5, 6]. Although quantum interference effects can be shown to occur in simple model systems[7], it has been challenging to understand how they will be present in realistic systems. Experimentally, it has proven to be difficult to extract the transport features associated with QI in charge transport through organic molecules. Self-assembled monolayers have shown effects of QI as changes in the curvature of the current voltage traces[8, 9]. Furthermore, destructive interference can lead to a difference in conductance in experiments comparing molecules with and without QI[10, 11]. However, both approaches lack the ability to shift the Fermi energy and explore the transmission as function of energy. This can be achieved in single-molecule electromigration[12] and electrochemical[13, 14] approaches, but apart from a conductance difference between two states the expected region of suppressed conductance has not yet been observed as a function of Fermi energy.

In the linear, off-resonant conductance regime multiple transport channels may contribute to the conductance of a junction that consists of a molecule placed in between metallic electrodes. Contributions to the total conduction consist of transport through the π-system, the σ-system[15], inelastic contributions[16] and when unpaired spins are present, Kondo correlations. These factors can mask the archetypal logarithmic destructive interference dip in off-resonant transport predicted in the π-system making it less pronounced and therefore difficult to distinguish in an experiment. In this chapter we explore the approach to enhance the probability to identify and characterize the quantum interference dip by using Kondo correlations[17].

For this purpose we use a molecule with a π-extended tetrathiafulvalene core[18] (see figure 5.1, named exTTF in the rest of this chapter). It consists of an anthracene backbone with on both ends spacers with an acetyl capped sulfur anchoring group. On the 9,10 position of the anthracene, two subgroups are connected forming an

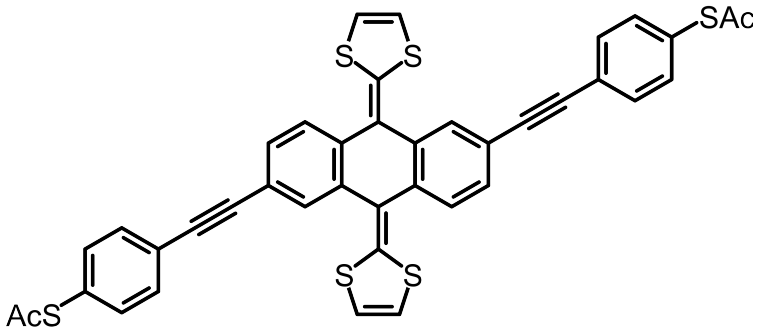

Figure 5.1: Structure of the molecule with a π-extended tetrathiafulvalene core. The sulfur groups used for anchoring are capped by acetyl groups (Ac).

π-extended tetrathiafulvalene. Charge transport measurements and calculations on exTTF have been performed[18]. Scanning probe based mechanical-breakjunction measurements show a very low conductance which could be caused by quantum interference due to the anthraquinone like core. Other molecules[19] containing TTF subgroups have shown to form Kondo correlations in transport when investigated with electromigration junctions. Therefore, a combination of the TTF subgroups with the anthraquinone like core in exTTF can be a good starting point to investigate the interplay between quantum interference and Kondo correlations.

To investigate charge transport through exTTF a solution of dichloromethane with 0.5 mM of exTTF was deposited on three-terminal electromigration junctions[20]. The electromigration junctions consist of an Au gate electrode covered with 5 nm of atomic layer deposition deposited aluminum oxide. On top of this oxide a 12 nm thick Au nanowire is deposited, which is connected to 100 nm thick Au bond pads. Feedback controlled electromigration[21] is performed on the Au nanowire at room temperature in the solution containing exTTF. When the junction resistance is below 5 KΩ, the electromigration is stopped and the wire is let to self-break[22] for approximately half an hour. After this, the sample space is pumped to low pressures and cooled down to cryogenic temperatures. The system possesses a superconducting magnet and heater-resistor for temperature and magnetic field dependent measurements as a function of applied bias (V) and gate (V_g) voltage.

The statistics of junction formation is discussed in the appendix (section 5.5). In the rest of this chapter we focus on a junction that switched between two distinctive configurations. The switching was reversible and uncontrollably induced by a temperature increase, bias- or gate-voltage. To discern between the two configurations in the text, we call them "state A" and "state B".

5.2. MEASUREMENTS OF STATE A

Figure 5.2a shows a differential conductance map of the junction in state A. The conductance varies from 50 μS up to 80 μS. Around zero-bias the differential conductance increases significantly, forming a peak-like structure over the entire gate range. The shape of the zero-bias structure changes as a function of gate voltage. This is seen more clearly in figure 5.2b, which shows the differential conductance at 11 different gate voltages. The traces are offset from each other. At negative gate voltage (lower traces) two peaks are present around zero-bias. Increasing the gate voltage (moving up in figure 5.2b) the suppression disappears and a single peak remains. The transition between these two different line-shapes occurs near zero gate voltage. The evolution of the height of the zero-bias feature is shown in figure 5.2c. The zero-bias differential conductance is represented by the black line. It first decreases with increasing gate voltage, reaches a minimum around $V_g = -2$ V and then rises and levels out for positive gate voltages. The dip in peak height cannot simply be attributed to the zero-bias peak moving to finite bias when making the gate voltage more negative. The red line in figure 5.2c represents the maximum differential conductance between

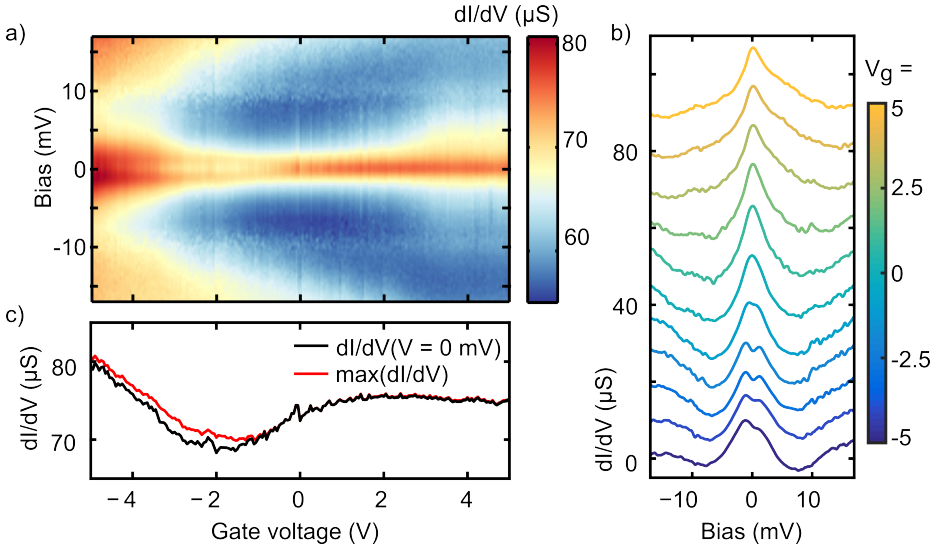

Figure 5.2: Differential conductance as a function of gate voltage for the junction in state A ($T = 2$ K, $B = 0$ T). a) Differential conductance map. b) Differential conductance traces at different gate voltages. The traces are offset from each other on the y-axis. c) Zero-bias differential conductance (black) and maximum of differential conductance within ±5 mV bias window (red) as a function of gate voltage.

±5 mV bias as a function of gate voltage. It shows a similar conductance suppression in the negative gate-voltage region.

To further study the zero-bias features of state A their dependence on magnetic field is shown in figure 5.3. Panel a) shows a differential conductance map of state A taken at $B = 8$ T. The map resembles that of the one measured at $B = 0$ T, however, the zero-bias features have changed. The two-peak structure at negative gate voltage and $B = 0$ T has merged into a single peak. At positive gate voltages the single peak has broadened. This can be seen more clearly in panel b), which shows the individual traces. Two distinct peaks start to develop for positive gate voltage, signifying a splitting. Again as at $B = 0$ T, there is a transition from a single to a two-peak structure as a function of gate voltage. Panel c) shows the magnetic field dependence of the second derivative of the current at selected gate voltages. For negative gate voltages there is a merging of the peaks, while at positive gate voltages the single peak splits. Moreover, for negative gate voltage the maximum of the second derivative seems to split as a function of magnetic field. One part shifts inward to form the peak at zero-bias, while the other is independent of magnetic field (green marks in the first three plots). The exact bias voltage at which this feature is present, depends on the gate voltage. This can also be seen in the map of the second derivative in panel a). Here (marked by the green ticks), a feature is visible that shifts inwards (i.e. to lower energies) with increasing gate voltage, matching the values of the marked excitations in the plots of

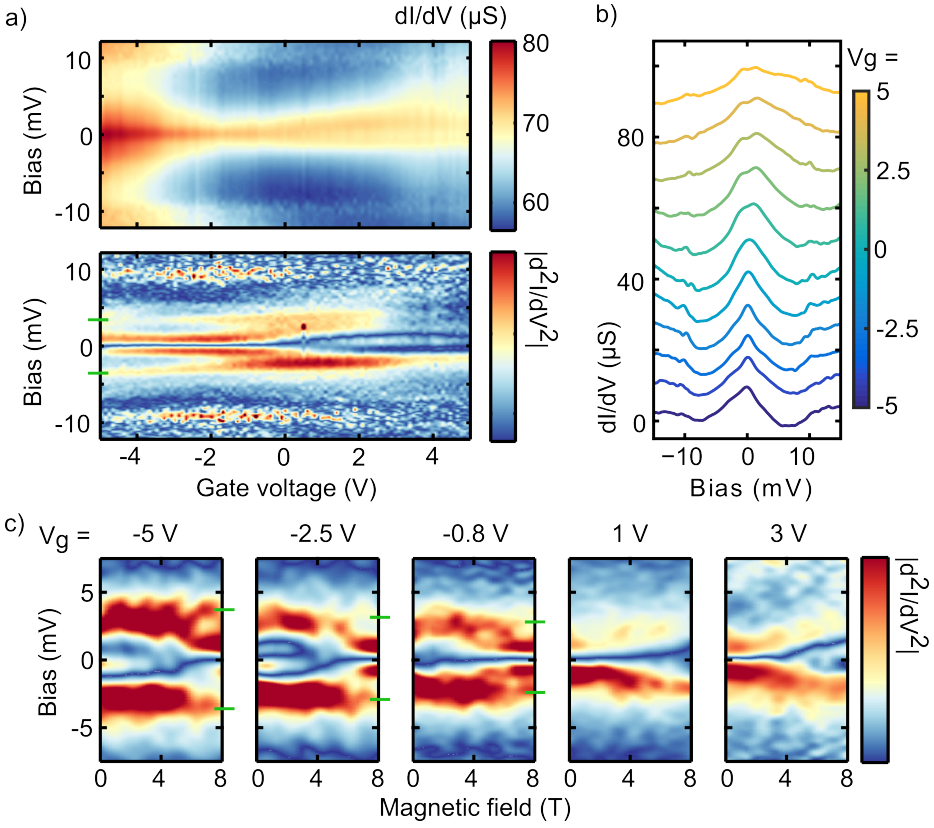

Figure 5.3: Magnetic field dependence of the differential conductance of state A ($T = 2$ K). a) Upper panel: Differential conductance map at $B = 8$ T. Lower panel: Derivative of the differential conductance to highlight the presence of a low-lying excitation indicated by the green ticks. b) Differential conductance traces at different gate voltages at $B = 8$ T. The traces are offset from each other. c) Derivative of the differential conductance traces as a function of magnetic field. The gate voltage at which each magnetic field dependence is taken is indicated at the top of the respective panel. With green markers the magnetic field independent excitation is shown; it is not visible for the two panels on the right hand side recorded at a positive gate voltage.

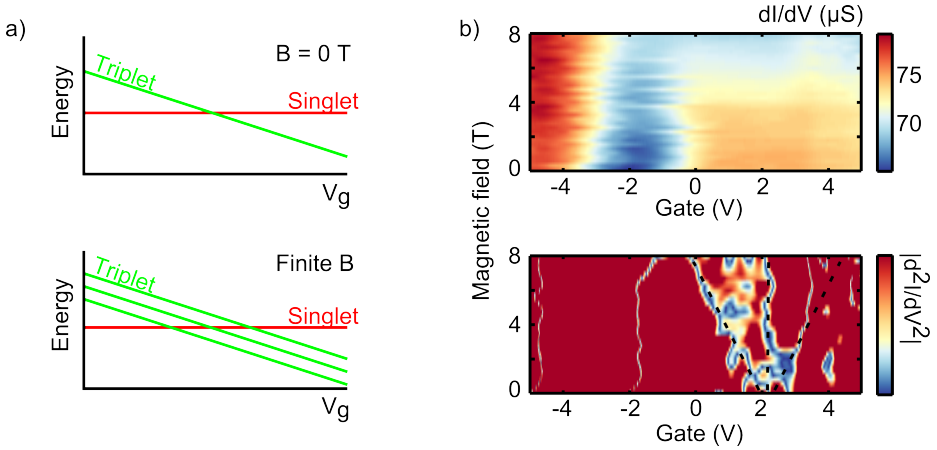

Figure 5.4: Gate induced singlet-triplet transition ($T = 2$ K). a) Schematic of the energy levels of the singlet and triplet states as a function of gate voltage for $B = 0$ T (top) and at a finite magnetic field (bottom). b) Map of the zero-bias conductance versus magnetic field (top). Below is the magnetic field dependence of the derivative of the differential conductance versus gate voltage to highlight minima and maxima.

5

panel c).

The fact that the shape of the zero-bias feature and its magnetic-field dependence changes as a function of gate voltage suggests that a gate-induced change of the magnetic ground state occurs. The measurements therefore may thus suggest a gate mediated singlet to triplet transition[23, 24]. As is schematically shown in figure 5.4a, at negative gate voltage the ground state is a singlet with a nearby triplet state. Due to the singlet-triplet energy difference being comparable to the width of the Kondo correlations it results in a two-stage Kondo line-shape[25]. Applying a magnetic field splits the higher lying triplet state and the dip in the two-stage Kondo line-shape is lifted by the $S = 1, m = -1$ triplet becoming degenerate with the singlet. The $S = 1, m = 0$ state is independent of magnetic field as is seen in the data, while the $S = 1, m = 1$ state is not observed. Apparently by increasing the gate voltage the singlet-triplet energy difference decreases until the singlet and triplet state are degenerate resulting in an enhancement of the differential conductance[26]. Increasing the gate voltage even further results in a triplet ground state that exhibits an under-screened spin-1 Kondo[27]. Although shoulders seem to appear at large positive gate voltage in figure 5.2b, it seems that the width of the Kondo zero-bias peak is still larger than the singlet-triplet energy difference.

The above description of the system is further supported by the measurements in panel b) in figure 5.4. Here, the zero-bias conductance as a function of magnetic field is shown. At negative gate voltage, increasing the magnetic field results in an increase of the differential conductance as the singlet and the $S = 1, m = -1$ triplet state are brought closer together. At positive gate voltage the intensity of the zero-bias conduc-

tance decreases due to the splitting of the spin-1 Kondo peak. Taking the derivative of the zero-bias conductance with respect to the gate voltage gives information about the presence of conductance minima and maxima as a function of gate voltage. This is shown in the bottom panel in b); at $V_g = -2$ V a line represents a minimum in the differential conductance as a function of gate. At higher gate voltage a more complex pattern is observed, where three lines may be discerned. One shifting downwards in gate with increasing magnetic field, one staying constant and a third one shifting upwards. However, due to switching of the sample it does not pass $V_g = 3.5$ V. The splitting of the peak as a function of magnetic field can be explained with the scheme presented in figure 5.4a. Assuming that the triplet state is Zeeman split with $g = 2$, the effective gating of the singlet-triplet energy difference can be deduced to be 0,46 mV/V. This value matches with the slope of the excitation in the lower panel of figure 5.3a.

5.3. MEASUREMENTS OF STATE B

As previously noted, the junction switched reversibly but uncontrollably between two configurations. The conductance map in the second configuration, which we will call "state B", is shown in figure 5.5. Panel a) shows the differential conductance map. Again as in "state A" the conductance of the junction is high; an increase in conductance is observed at negative gate voltage and low-bias features are visible across the entire gate range. However, upon a closer inspection the zero-bias features differ from the features in state A. In state B, over the entire gate voltage range a single peak is present (see figure 5.5b). Alongside the zero-bias peak, peaks are present at a finite bias voltage, the position of which shift as a function of gate voltage. The height of the zero-bias peak is shown in figure 5.5c. It is non-monotonic, showing a minimum at $V_g = 2$ V and a kink around $V_g = -1$ V.

The magnetic field and temperature dependence of the conductance are shown in figure 5.6. Panel a) compares the differential conductance traces at $B = 0$ T (blue) with those recorded at $B = 8$ T (red) for 4 different gate voltages. For each gate voltage, the zero-bias peak height decreases and the peaks split when $B = 8$ T is applied. The exact shape of the split peak depends on the gate voltage. There is a tendency for the finite bias peaks to shift inwards, however, this can also be due to an overlap of the zero-bias peak shifting outwards due to the splitting. As can be seen in figure 5.6b, the splitting is present over the entire gate range.

In figure 5.6, panel c) shows the height of the zero-bias peak as a function of temperature (logarithmic scale) for selected gate voltages. At all gate voltages the peak height decreases with increasing temperature, although the exact temperature dependence varies among the curves. For example, the curve at $V_g = 0$ V is steeper than the one at $V_g = 1.5$ V and the curvature at $V_g = -1.5$ V is different from the one recorded at $V_g = 3$ V.

Although a zero-bias peak is present over the entire gate range in state B, its exact shape, magnetic-field and temperature dependence varies with gate voltage. To

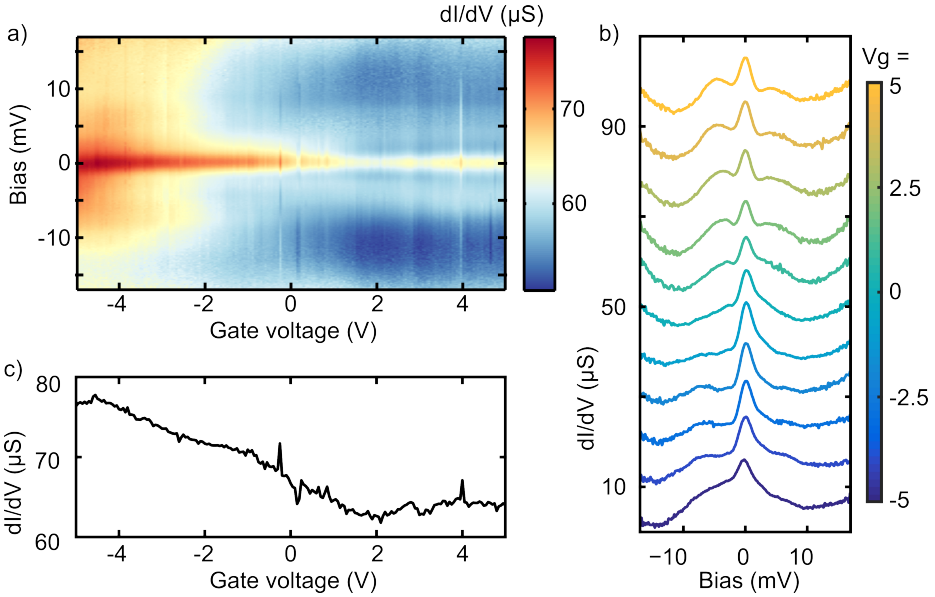

Figure 5.5: Gate dependence of the differential conductance of state B ($T = 2$ K, $B = 0$ T). a) Differential conductance map. b) Differential conductance traces as function of gate voltage. Traces are offset from each other. c) Zero-bias conductance as a function of gate voltage. Contrary to state A, for all gate voltages the conductance maximum is at zero bias.

characterize this in more detail, figure 5.7 shows as a function of gate voltage for four panels: a) the height of the zero-bias peak at $B = 0$ T (blue) and $B = 8$ T (black), b) the location of the zero-bias peak(s) at $B = 0$ T (blue) and $B = 8$ T (black) and the location of the finite bias peaks at $B = 0$ T (red), c) the estimated width of the zero-bias peak (see the appendix) and d) the curvature (yellow) and decrease (orange) of the zero-bias peak height as a function of temperature. The curvature is determined by fitting a second order polynomial to the dependence of the zero-bias peak height with logarithmic temperature and noting the quadratic coefficient for the fit. The conductance decrease is determined by taking the difference between the zero-bias peak height at the lowest measured temperature ($T = 2$ K) and the highest temperature ($T = 10$ K).

In general, three regimes can be identified as a function of gate voltage (marked by the dashed lines). The first one is from $V_g = -5$ V to $V_g = -1$ V. Here the ZBP height decreases with increasing gate voltage, the finite bias peaks stay constant in energy and the estimated width of the ZBP decreases. In the last panel there is a small increase of the conductance drop, but after that it stays constant up to $V_g = -1$ V and the quadratic coefficient fluctuates around zero. Meaning, a linear decrease in zero-bias peak height as a function of logarithmic temperature. From $V_g = -1$ V to $V_g = 1$ V an accelerated decrease of the ZBP with respect to gate voltage is visible

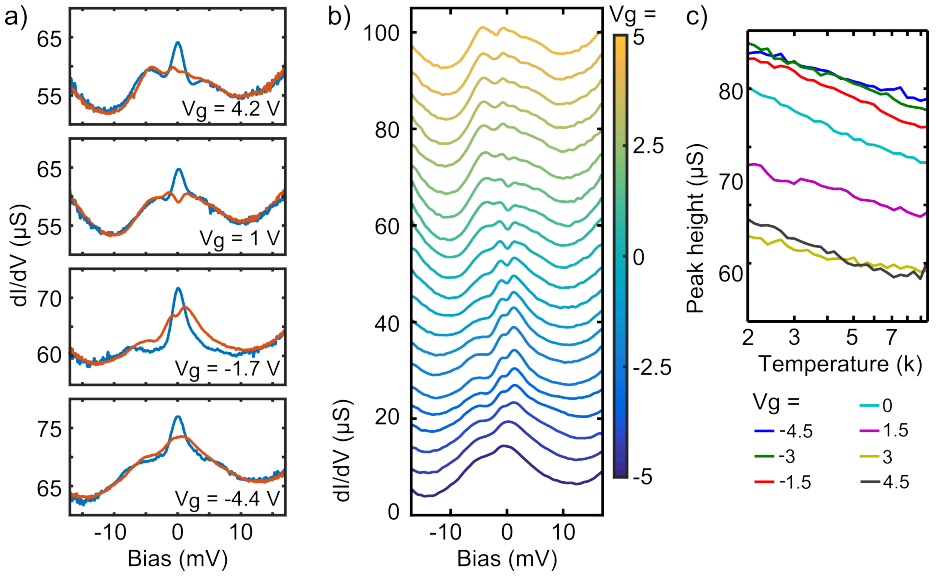

Figure 5.6: Magnetic field and temperature dependence of the differential conductance in state B. a) Differential conductance traces at different gate voltages for $B = 0$ T (blue) and $B = 8$ T (red) ($T = 2$ K). b) Differential conductance traces at various gate voltages taken at $B = 8$ T ($T = 2$ K). For clarity, the traces are offset from each other. c) Temperature dependence of the zero-bias peak height for different gate voltages ($B = 0$ T). The temperature, on the x-axis, is on a logarithmic scale.

while the finite bias peaks and magnetic field splitting start to increase. The estimated width of the ZBP also increases. Furthermore, the conductance drop decreases and the quadratic coefficient becomes negative. In the regime from $V_g = 1$ V to $V_g = 3$ V (when $V_g > 3$ V the junction starts to switch) the ZBP peak height starts to increase again. At the same time the finite bias peaks shift to higher energies and the magnetic field splitting decreases. The width of the ZBP also decreases. The conductance drop slowly increases again and the quadratic coefficient is positive.

Both state A and B show conductance features near zero-bias which are magnetic field dependent, furthermore state B also shows a decrease of conductance as a function of temperature (due to switching, temperature dependence on state A could not be measured). These observations suggest Kondo correlations to be present, which means that there should be unpaired spins on the molecule. We already suggested that the conductance features of state A resemble those of a singlet to triplet transition, mediated by the electric field from the gate electrode. This would mean 2 unpaired spins are present in the junction. This interpretation can be extended to state B by comparing the conductance features at positive gate voltage to experimental[23] and theoretical[28] calculations. The zero-bias peak can be interpreted as originating from under-screened spin-1 Kondo physics, with the peaks at finite bias originating

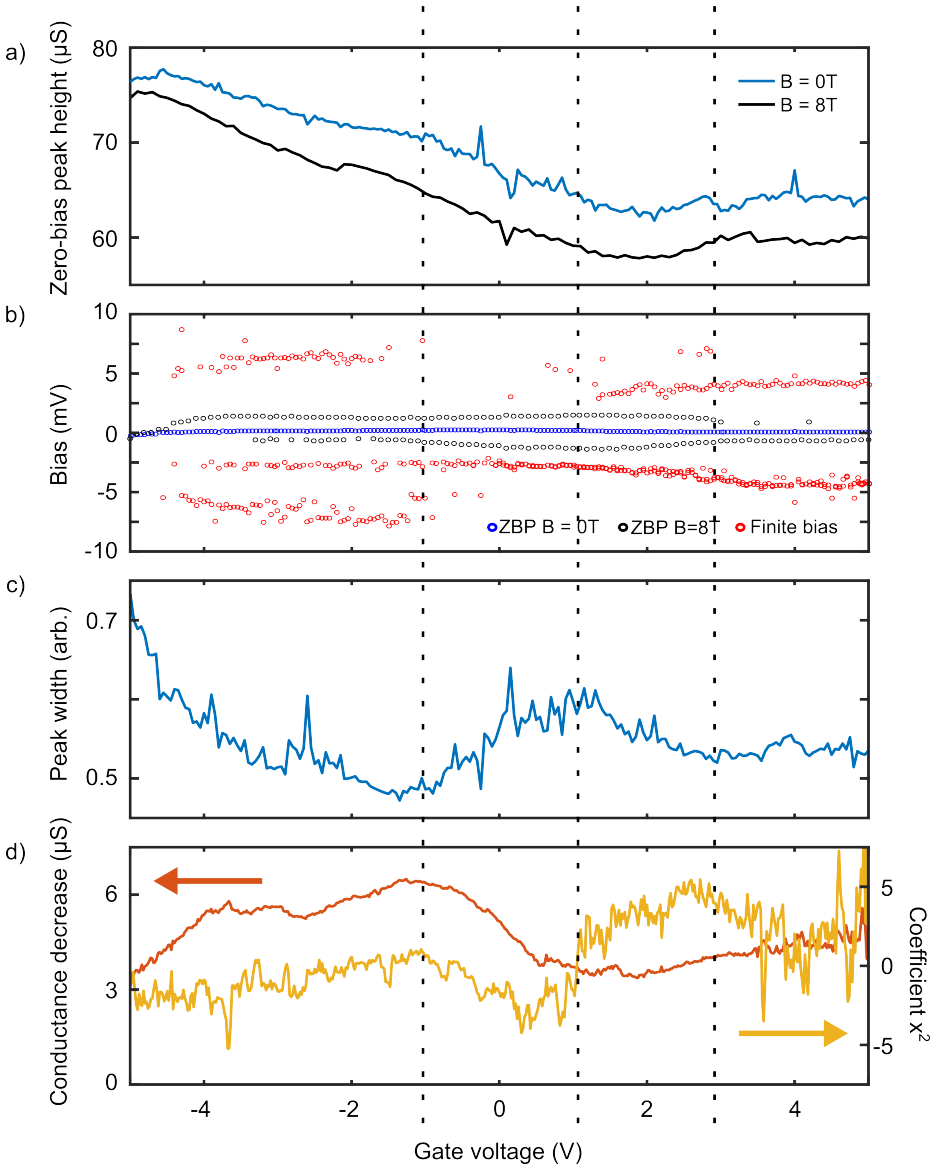

Figure 5.7: Characterization of the zero-bias peak of state B as a function of gate voltage. a) The zero-bias peak height for $B = 0$ T (blue) and $B = 8$ T (black) ($T = 2$ K). b) The locations of the zero-bias peak (blue), split zero-bias peaks at $B = 8$ T (black) and the finite bias peaks at $B = 0$ T (red) ($T = 2$ K). c) Estimated width of the zero-bias peak (see the appendix) ($T = 2$ K, $B = 0$ T). d) Quadratic coefficient of a second order linear fit to the logarithmic temperature dependence ($B = 0$ T) of the zero-bias peak height (yellow). Decrease in zero-bias peak height when increasing temperature from $T = 2$ K to $T = 10$ K (orange).

from the singlet state. The shifting of the finite bias peaks again suggests gate tunability of the singlet-triplet energy difference, consistent with the observations in state A.

5.4. DISCUSSION

In gas phase all spins are paired in the exTTF molecule raising the question why in transport we observe transport features originating from two unpaired spins. In literature two unpaired spins in molecules can either originate from organic radicals[29] or metal-ion containing molecules[30]. If this is not the case (as is the case in exTTF), nearly degenerate orbitals[12, 23] and/or the formation of new electrode mediated states[31] may result in unpaired electrons. Figure 5.8 shows a density functional calculation (DFT) of exTTF in the neutral and the +2 charge state. It can be seen that the geometry changes between the two charge states[32]. In the neutral state (figure 5.8a) the TTF groups are angled upwards, but are still relatively planar with the anthracene core. In the +2 charge state (figure 5.8b) the TTF groups rotate and are nearly perpendicular to the anthracene core. This change in geometry has an impact on the electronic structure of the molecule. For the neutral molecule a large HOMO-LUMO gap ($\approx$ 1.7 eV) is present. Both the HOMO and the LUMO orbital are localized on the anthracene core and the TTF side groups, with relatively little weight on the sulfur anchoring groups. The situation is different for the charged molecule. The HOMO-LUMO gap is now small ($\approx$ 40 meV, HOMO-1 to HOMO $\approx$ 250 meV, LUMO to LUMO+1 $\approx$ 280 meV), leading to a pair of nearly degenerate orbitals. The HOMO is delocalized along the backbone, with little weight on the TTF groups and significant weight on the anchoring groups. The LUMO is mostly present on the TTF groups with a small part on the anchoring groups.

For a low-energy triplet state to be present on exTTF, there needs to be an orbital freedom to circumvent the Pauli exclusion principle. As the neutral charge state does not have an orbital close-by the HOMO, it is unlikely for a triplet state to form. The +2 charge state on the other hand does have the orbital freedom to form a triplet state. What is also striking is the high conductivity of the junction, which is often associated with a large overlap of the frontier orbitals with the sulfur anchoring groups. This is the case for the +2 charge state and not for the neutral state. Taking these arguments together, the measurements suggests that an exTTF molecule in the +2 charge state could be a viable explanation for the appearance of the singlet-triplet features in transport.

The peculiar electronic structure of the +2 charge state of exTTF, can also give a possible explanation for the electric-field dependence of the singlet-triplet energy difference. The HOMO and the LUMO differ significantly in their spatial shape, with the LUMO being localized on the center of the molecule and the HOMO on the anchoring groups. Considering that in a three-terminal junction with a nano-gap the electric potential from the gate can be non-linear due to screening by the metallic electrodes[33] (see chapter 7 for further explanation), the gating efficiency of the HOMO and LUMO

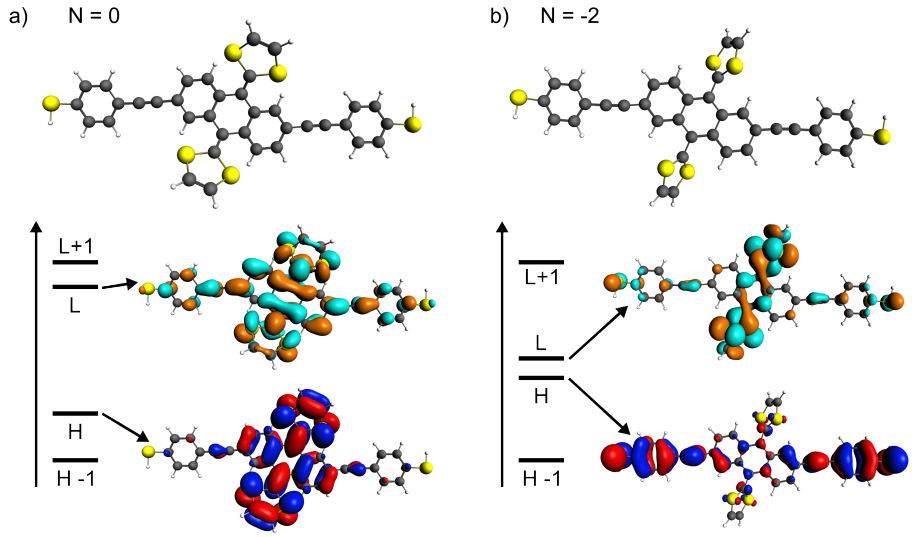

Figure 5.8: DFT calculations of the exTTF molecule in the neutral and +2 charge state. H stands for HOMO and L for LUMO. a) Top panel: geometry of the molecule in the neutral charge state. Lower panel: schematic of the orbital energies and the orbital wavefunction of the HOMO (red-blue) en LUMO (orange-green) orbitals. b) same as in a), but for the +2 charge state of exTTF.

can be different. The energy of the HOMO-LUMO gap is then tunable by the gate voltage and therefore also the singlet-triplet energy difference[24].

It is interesting to compare exTTF to other single-molecule junctions[23, 24] that show a singlet-triplet energy difference that can be tuned by a gate electrode. For the three different molecular junctions, the estimated gate coupling of the resonances (α) and the gate coupling of the singlet-triplet energy difference (α_J) is shown in table 5.1. Both C_{60} and the Mn-complex have a higher singlet-triplet gating than exTTF. However, this value does not take into account the electric potential present at the molecule. Effectiveness of the gate electrode is captured in the gate coupling (α) and one should take this into account when comparing the values. To compare the three systems it is thus insightful to calculate the ratio of the coupling to the resonances to the singlet-triplet coupling, as shown in the last column of table 5.1. For exTTF, the table shows that the singlet-triplet splitting is an order of magnitude more sensitive to the gate electrode than the other two systems. A possible explanation for this could be the strong spatial separation of the nearly degenerate orbitals, as discussed in the previous paragraph.

A thorough discussion of the exact shape and evolution of the transport features at low-bias as a function of gate, are beyond the scope of this chapter. The underlying model should incorporate two-unpaired interacting spins that form a singlet and triplet state, whose energy difference can be tuned by a gate. For both state A

Table 5.1: Table comparing coupling values from different single-molecule experiments. Mn-complex parameters are from [24] and C_{60} from [23]. Values for C_{60} and Mn-complex are estimated from figures with a ±20% uncertainty. Estimation of α for exTTF is discussed in the appendix.

System	**Singlet-triplet (α_J) mV/V**	**Gate (α) mV/V**	**Ratio (α_J/α)**
exTTF	0.5	1.5	0.33
Mn-complex	1.25	40	0.03
C_{60}	5	110	0.05

and B the singlet-triplet energy difference is of the same order as the Kondo energy scale. To accurately investigate the transport features in this regime, elaborate theoretical calculations need to be performed. These could improve our understanding of the observed features: the suppression of the zero-bias conductance, the apparent non-linear behavior of the singlet-triplet energy difference and the unusual temperature dependence and shape of the under-screened spin-1 Kondo peak as a function of gate voltage. This would make it possible to understand if quantum interference effects also play a role in the transport measurements.

To conclude, we have measured an exTTF molecule in a three-terminal electromigration junction. One junction showed gate-dependent singlet-triplet features. The experiments are explained by the exTTF molecule being in a +2 charge state, which possesses a pair of degenerate orbitals. The gate dependence is linked to the fact that the wavefunctions of the degenerate orbitals are located at different positions in the molecule, promoting differential gating. This research could be a starting point for molecules which have, by design, degenerate but spatially distinctive orbital wavefunctions to promote gate dependent singlet-triplet states. This could be useful in investigating novel Kondo effects involving multiple unpaired spins.

5.5. APPENDIX

STATISTICS ON JUNCTION FORMATION

In total 105 Au nanowires have been successfully electromigrated. As shown in figure 5.9a, 41 % of all junctions showed gate-dependent charge transport. Approximately 26 % of the junctions showing gate modulated charge transport also showed zero-bias features.

Apart from the junction discussed in the main text, the remainder of the junctions showing a zero-bias peak showed no finite bias features. The height and width of the zero-bias peak varies from sample to sample. The nature of the gate dependence of the peak height is shown in figure 5.9b. Negative stands for an increase in the ZBP height towards negative gate voltage while positive stands for an increase in height towards the positive gate voltage. In total 7 junctions with a zero-bias peak show an increase of the zero-bias peak height when applying a positive gate.

ESTIMATING THE WIDTH OF THE ZERO-BIAS PEAK

The appearance of peaks at finite bias and the dependence of the background on gate voltage, make it difficult to use a Lorentzian or Gaussian peak shape to determine the width of the zero-bias peak. To try to circumvent this problem, we estimate the width of the zero-bias peak from a fit to the curvature of the peak maximum only. A second order Taylor expansion for both a Lorentzian and Gaussian peak around it maximum results respectively in:

$$f(x) = a + b\frac{(c/2)^2}{x^2 + (c/2)^2} \rightarrow f(x)_{x=0} = a + b - \frac{4b}{c^2}x^2, \tag{5.1}$$

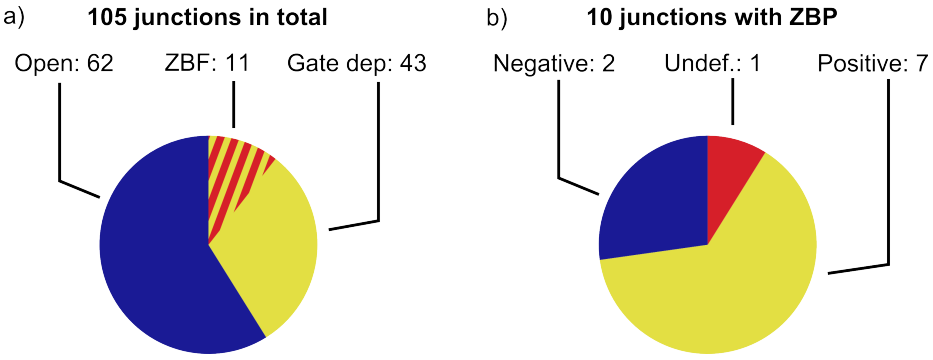

Figure 5.9: a) Statistics of successfully electromigrated nanowires. Open means no gate dependence of current. Junction with a gate dependence are labelled as gate dependent. Of these some show zero-bias features; these are labeled as ZBF. b) 10 junctions show a zero-bias peak. These have been characterized by the peak height increasing towards negative or positive gate voltage. One junction showed no dependence of the zero-bias peak height.

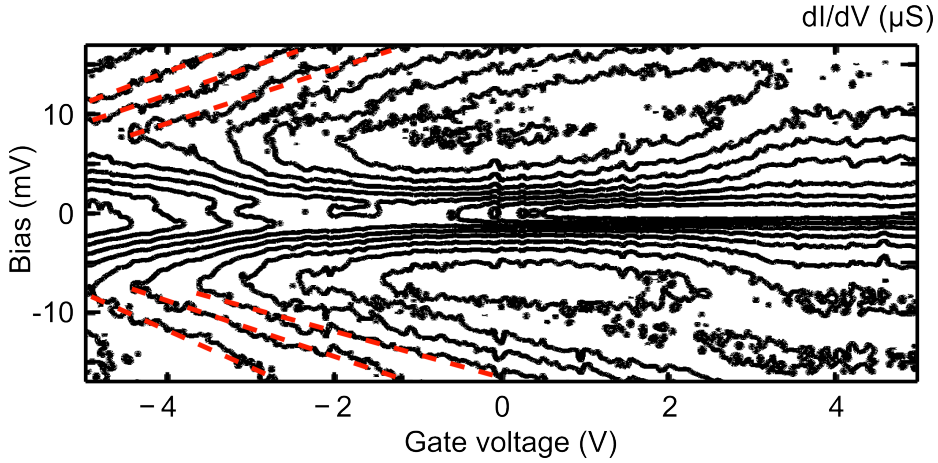

Figure 5.10: Contour plot of the differntial conductance map of state A shown in figure 5.2. The black lines are the contour lines. The red lines are linear fits to the contour lines.

$$g(x) = a + be^{\frac{4\ln 2x^2}{c^2}} \rightarrow g(x)_{x=0} = a + b - \frac{4\ln 2b}{c^2}x^2. \tag{5.2}$$

Both expansions show that the full width half maximum (c) is only present in the quadratic term. If we fit the peak maximum in the experimental data with a second order polynomial ($h(x) = \alpha_0 + \alpha_1 x + \alpha_2 x^2$), then $\alpha_2 = -\beta c^2/b$ with $\beta = 4$ in the Lorentzian case and $\beta = 4ln(2)$ in the Gaussian case. Assuming the change in height of the zero-bias peak (b) is not too large as a function of gate, the relation $c \sim \sqrt{1/\alpha_2}$ gives us an estimate of the width of the zero-bias peak.

ESTIMATING THE GATE COUPLING OF THE RESONANCES (α)

To get an accurate value for the gate coupling of the resonances (α), a charge degeneracy point needs to be present in the differential conductance map. However, in the measurements of state A or B this is not the case. To get a rough estimate for the gate coupling of the resonances for state A, we applied a linear fit to the equipotential lines of the conductance map of figure 5.2, see figure 5.10. From this we get an average gate coupling α of 1.5 mV/V.

REFERENCES

[1] R. Baer and D. Neuhauser, *Phase coherent electronics: A molecular switch based on quantum interference,* J. Am. Chem. Soc. **124**, 4200 (2002).

[2] R. Stadler, M. Forshaw, and C. Joachim, *Modulation of electron transmission for molecular data storage,* Nanotechnology **14**, 138 (2003).

[3] E. H. van Dijk, D. J. T. Myles, M. H. van der Veen, and J. C. Hummelen, *Synthesis and properties of an anthraquinone-based redox switch for molecular electronics,* Org. Lett. **8**, 2333 (2006).

[4] D. Q. Andrews, G. C. Solomon, R. P. Van Duyne, and M. A. Ratner, *Single molecule electronics: Increasing dynamic range and switching speed using cross-conjugated species,* J. Am. Chem. Soc. **130**, 17309 (2008).

[5] J. P. Bergfield and C. A. Stafford, *Thermoelectric signatures of coherent transport in single-molecule heterojunctions,* Nano Lett. **9**, 3072 (2009).

[6] C. M. Finch, V. M. García-Suárez, and C. J. Lambert, *Giant thermopower and figure of merit in single-molecule devices,* Phys. Rev. B **79**, 033405 (2009).

[7] G. C. Solomon, D. Q. Andrews, T. Hansen, R. H. Goldsmith, M. R. Wasielewski, R. P. Van Duyne, and M. A. Ratner, *Understanding quantum interference in coherent molecular conduction,* J. Chem. Phys. **129**, 054701 (2008).

[8] C. M. Guedon, H. Valkenier, T. Markussen, K. S. Thygesen, J. C. Hummelen, and S. J. van der Molen, *Observation of quantum interference in molecular charge transport,* Nat. Nano. **7**, 305 (2012).

[9] V. Rabache, J. Chaste, P. Petit, M. L. Della Rocca, P. Martin, J.-C. Lacroix, R. L. McCreery, and P. Lafarge, *Direct observation of large quantum interference effect in anthraquinone solid-state junctions,* J. Am. Chem. Soc. **135**, 10218 (2013).

[10] V. Kaliginedi, P. Moreno-García, H. Valkenier, W. Hong, V. M. García-Suárez, P. Buiter, J. L. H. Otten, J. C. Hummelen, C. J. Lambert, and T. Wandlowski, *Correlations between molecular structure and single-junction conductance: A case study with oligo(phenylene-ethynylene)-type wires,* J. Am. Chem. Soc. **134**, 5262 (2012).

[11] C. R. Arroyo, S. Tarkuc, R. Frisenda, J. S. Seldenthuis, C. H. M. Woerde, R. Eelkema, F. C. Grozema, and H. S. J. van der Zant, *Signatures of quantum interference effects on charge transport through a single benzene ring,* Angew. Chem. **125**, 3234 (2013).

[12] M. Koole, J. M. Thijssen, H. Valkenier, J. C. Hummelen, and H. S. J. van der Zant, *Electric-field control of interfering transport pathways in a single-molecule anthraquinone transistor,* Nano Lett. **15**, 5569 (2015).

[13] S. Tsoi, I. Griva, S. A. Trammell, A. S. Blum, J. M. Schnur, and N. Lebedev, *Electrochemically controlled conductance switching in a single molecule: Quinone-modified oligo(phenylene vinylene),* ACS Nano **2**, 1289 (2008).

[14] M. Baghernejad, X. Zhao, K. Baruël Ørnsø, M. Füeg, P. Moreno-García, A. V. Rudnev, V. Kaliginedi, S. Vesztergom, C. Huang, W. Hong, P. Broekmann, T. Wandlowski, K. S. Thygesen, and M. R. Bryce, *Electrochemical control of single-molecule conductance by Fermi-level tuning and conjugation switching,* J. Am. Chem. Soc. **136**, 17922 (2014).

[15] G. C. Solomon, D. Q. Andrews, R. P. Van Duyne, and M. A. Ratner, *Electron transport through conjugated molecules: When the π system only tells part of the story,* ChemPhysChem **10**, 257 (2009).

[16] T. Markussen and K. S. Thygesen, *Temperature effects on quantum interference in molecular junctions,* Phys. Rev. B **89**, 085420 (2014).

[17] A. K. Mitchel, K. G. L. Pedersen, P. Hedegård, and J. Paaske, *Kondo blockade due to quantum interference in single-molecule junctions,* unpublished (2016).

[18] R. García, M. A. Herranz, E. Leary, M. T. González, G. R. Bollinger, M. Bürkle, L. A. Zotti, Y. Asai, F. Pauly, J. C. Cuevas, N. Agrait, and N. Martin, *Single-molecule conductance of a chemically modified, π-extended tetrathiafulvalene and its charge-transfer complex with F4TCNQ,* Beilstein J. Org. Chem. **11**, 1068 (2015).

[19] M. Mansø, M. Koole, M. Mulder, I. J. Olavarria-Contreras, C. L. Andersen, M. Jevric, S. L. Broman, A. Kadziola, O. Hammerich, H. S. J. van der Zant, and M. B. Nielsen, *Synthesis and single-molecule conductances of neutral and cationic indenofluorene-extended tetrathiafulvalenes: Kondo effect molecules,* J. Org. Chem. **81**, 8406 (2016).

[20] H. Park, A. K. L. Lim, A. P. Alivisatos, J. Park, and P. L. McEuen, *Fabrication of metallic electrodes with nanometer separation by electromigration,* Appl. Phys. Lett. **75**, 301 (1999).

[21] D. R. Strachan, D. E. Smith, D. E. Johnston, T.-H. Park, M. J. Therien, D. A. Bonnell, and A. T. Johnson, *Controlled fabrication of nanogaps in ambient environment for molecular electronics,* Appl. Phys. Lett. **86**, 043109 (2005).

[22] K. O'Neill, E. A. Osorio, and H. S. J. van der Zant, *Self-breaking in planar few-atom Au constrictions for nanometer-spaced electrodes,* Appl. Phys. Lett. **90**, 133109 (2007).

[23] N. Roch, S. Florens, V. Bouchiat, W. Wernsdorfer, and F. Balestro, *Quantum phase transition in a single-molecule quantum dot,* Nature **453**, 633 (2008).

[24] E. A. Osorio, K. Moth-Poulsen, H. S. J. van der Zant, J. Paaske, P. Hedegård, K. Flensberg, J. Bendix, and T. Bjørnholm, *Electrical manipulation of spin states in a single electrostatically gated transition-metal complex,* Nano Lett. **10**, 105 (2010).

[25] W. Hofstetter and G. Zarand, *Singlet–triplet transition in lateral quantum dots: A numerical renormalization group study,* Phys. Rev. B **69**, 235301 (2004).

[26] S. Sasaki, S. De Franceschi, J. M. Elzerman, W. G. van der Wiel, M. Eto, S. Tarucha, and L. P. Kouwenhoven, *Kondo effect in an integer-spin quantum dot,* Nature **405**, 764 (2000).

[27] S. Florens, A. Freyn, N. Roch, W. Wernsdorfer, F. Balestro, P. Roura-Bas, and A. A. Aligia, *Universal transport signatures in two-electron molecular quantum dots: gate-tunable Hund's rule, underscreened Kondo effect and quantum phase transitions,* J. Phys. Condens. Mat. **23**, 243202 (2011).

[28] P. Roura Bas and A. A. Aligia, *Nonequilibrium transport through a singlet-triplet anderson impurity,* Phys. Rev. B **80**, 035308 (2009).

[29] R. Gaudenzi, E. Burzurí, D. Reta, I. d. P. R. Moreira, S. T. Bromley, C. Rovira, J. Veciana, and H. S. J. van der Zant, *Exchange coupling inversion in a high-spin organic triradical molecule,* Nano Lett. **16**, 2066 (2016).

[30] J. J. Parks, A. R. Champagne, T. A. Costi, W. W. Shum, A. N. Pasupathy, E. Neuscamman, S. Flores-Torres, P. S. Cornaglia, A. A. Aligia, C. A. Balseiro, G. K.-L. Chan, H. D. Abruña, and D. C. Ralph, *Mechanical control of spin states in spin-1 molecules and the underscreened Kondo effect,* Science **328**, 1370 (2010).

[31] J. Fock, M. Leijnse, K. Jennum, A. S. Zyazin, J. Paaske, P. Hedegård, M. Brøndsted Nielsen, and H. S. J. van der Zant, *Manipulation of organic polyradicals in a single-molecule transistor,* Phys. Rev. B **86**, 235403 (2012).

[32] N. Martín, L. Sánchez, M. n. Herranz, B. Illescas, and D. M. Guldi, *Electronic communication in tetrathiafulvalene TTF / C_{60} systems: Toward molecular solar energy conversion materials?* Acc. Chem. Res. **40**, 1015 (2007).

[33] S. S. Datta, D. R. Strachan, and A. T. C. Johnson, *Gate coupling to nanoscale electronics,* Phys. Rev. B **79**, 205404 (2009).

6

CHARGE TRANSPORT THROUGH CONJUGATED AZOMETHINE-BASED SINGLE MOLECULES

The single-molecule conductance of a 3-ring, conjugated azomethine was studied using the mechanically controlled breakjunction technique. Charge transport properties are found to be comparable to vinyl-based analogues; findings are supported with density functional calculations. The simple preparation and good transport properties make azomethine-based molecules an attractive class for use in polymer and single-molecule organic electronics.

This chapter has been published in Organic Electronics **34**, 38-41 (2016) [1]. I would like to thank R. Frisenda for help with measurements, M.L. Perrin for help with the calculations and M.L. Petrus for the synthesis.

6.1. INTRODUCTION

Organic molecules have received great attention over the last two decades for their application in organic electronics such as organic light emitting diodes (OLED), organic field effect transistors (OFET), organic photovoltaics (OPV), sensors and electrochromic devices[2–5]. The synthesis of these conjugated materials generally involves transition metal catalyzed carbon-carbon coupling reactions such as Suzuki-, Stille- and Kumada-coupling[6]. However, these chemistries require stringent reaction conditions, expensive catalysts and extensive product purification[7]. The restrictive synthetic accessibility results in high costs thereby making large-scale production of these materials difficult[8, 9].

Schiff-base condensation chemistry offers a low-cost alternative route to conjugated materials. In this reaction an azomethine bond (–CH=N–, also referred to as imine) is formed on condensation of an amine with an aldehyde. This chemistry offers an attractive alternative to carbon-carbon coupling reactions since the reaction can be performed at near ambient conditions, requires no expensive catalysts, and has water as the only by-product, making purification straightforward[10]. In contrast to aliphatic azomethines[11], conjugated azomethines are very stable against photoisomerization and also exhibit a high stability towards hydrolysis and reduction[12, 13].

Conjugated azomethine-based polymers and small-molecules have shown promising performance as polymer-[14–17], small-molecule-[10, 18] and perovskite-based[19] photovoltaics, OLEDs [20], OFETs[21] and electrochromic devices[22, 23]. In particular the low molar mass azomethines have shown good performances as a hole conducting material in bulk heterojunction devices[24], and azomethines have been able to compete with state-of-the-art materials in a hole transporting layer in perovskite solar cells[19]. However, despite the good device performance, only very little is known about charge transport in these molecules[21, 24]. Bulk measurements have shown relatively low mobilities, but it is unclear which mechanisms contribute to the low mobility.

In this work, the single-molecule conductance of an azomethine-based molecule is studied to get a better insight in its charge transport properties. The general perception is that the azomethine bond is isoelectronic to the vinyl-bond (–CH=CH–)[25], which is widely used in polymer and single-molecule organic electronics. However, the single-molecule conductance through a molecule containing azomethine bonds has not yet been studied. We performed conductance measurements of a conjugated azomethine-based single molecule using a mechanically controlled break junction (MCBJ). Our findings show that replacing the all-carbon vinyl bonds with azomethine bonds does not compromise the conductance in this class of molecules and that the azomethine-bond thus does not limit the conductance along the backbone of the molecule.

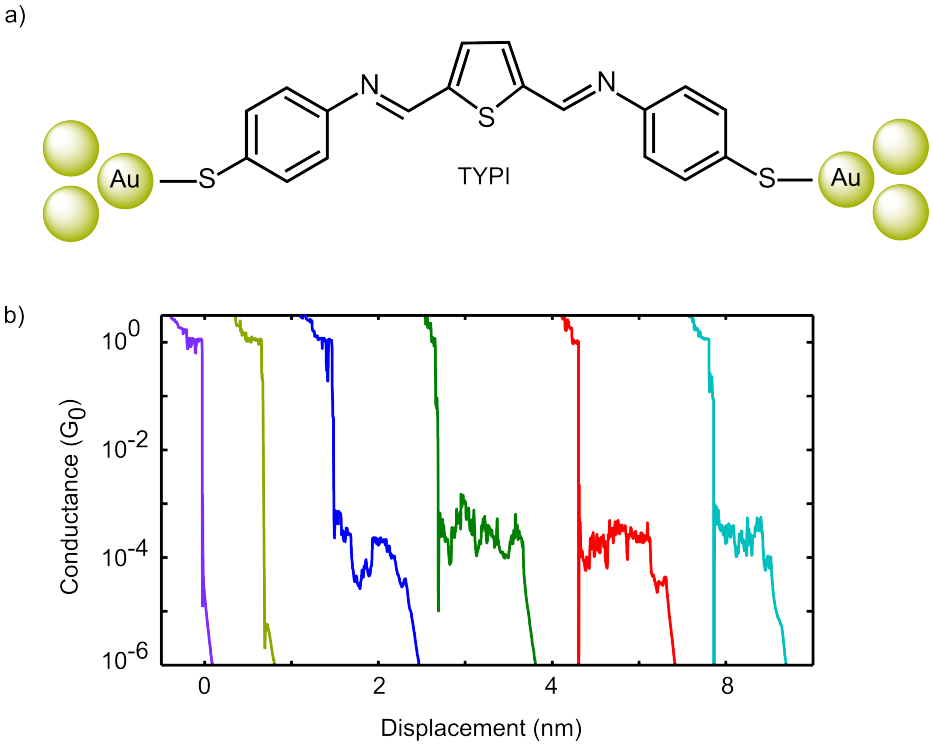

Figure 6.1: a) TYPI structure between gold electrodes. b) Individual breaking traces measured in the presence of TYPI. The bias voltage is 100 mV and the electrodes are withdrawn at a speed of 5 nm/s. The traces are offset along the x-axis for clarity. The conductance is plotted on a logarithmic scale.

6.2. MEASUREMENTS

As a model compound for studying the conductance of the azomethine-bond, a symmetric azomethine, containing a thiophene and two phenyl rings was synthesized (thiophene-2,5-diylbis(N-phenylmethanimine), named TYPI from now on. See appendix for synthesis and characterisation). At the para-position, the phenyl rings are functionalized with thiol groups, which act as the anchor to the gold electrodes (figure 6.1a). To characterize the conductance of TYPI a MCBJ set-up was used[26]. TYPI was dissolved in dichloromethane at a concentration of 0.5 mM. The solution was drop cast on the MCBJ, after which the gold wire was repeatedly broken and fused at a rate of 20 cycles per minute (corresponding to an electrode displacement speed of 5 nm/s). The measurements were performed in ambient conditions at a fixed bias voltage of 100 mV.

When breaking the gold wire in the presence of TYPI we observe conductance traces as shown in figure 6.1b. The conductance traces are measured as a function of

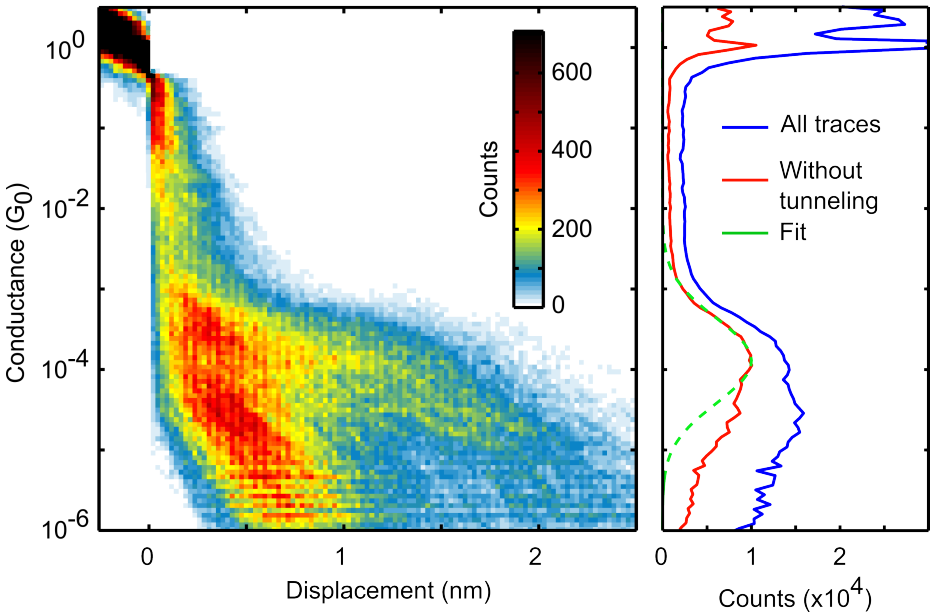

Figure 6.2: Conductance histograms of all breaking traces. Traces are aligned at 0.5 G_0. Left panel: Conductance-displacement histogram build from 2361 breaking traces like the ones shown in figure 6.1b. The traces are binned logarithmically along the conductance (y) axis with 16 bins/decade and linearly binned along the displacement (x) axis with 40 bins/nm. Right panel: Conductance histogram. The blue line is built by summing the histogram in the left panel along the displacement axis. Red line is constructed by excluding tunneling traces. Green dashed line is a Gaussian fit used to extract the most probable conductance value.

electrode separation (nm). Above conductance values of 1 G_0 (the conductance quantum of 77 µS) the traces show decreasing steps and at approximately 1 G_0 a sharp drop is observed, which is caused by the rupture of the last gold few-atom connection[27]. After this point the conductance quickly drops to around $10^{-3}/10^{-4}$ G_0, due to the snap back of the gold apex atoms in the electrodes. Below 10^{-3} G_0 two different types of traces can be identified. The first one is an exponential decay of the conductance (linear dependence in a log-plot) to the noise level of the setup (below 10^{-6} G_0), which is characteristic of an empty junction where transport is through direct tunneling (the first two traces in figure 6.1b). The second type of trace that can be identified, is the appearance of plateau-like features below 10^{-3} G_0. These plateaus persist up to 1.5 nm of stretching and show conductance fluctuations around 10^{-4} G_0. The traces with this kind of conductance-length dependence are assigned to the successful formation of a gold-molecule-gold junction[28]. After stretching for a certain distance, which is related to the length of the molecule, the conductance drops to the noise level due to breaking of the gold-molecule-gold junction.

To determine the most probable conductance of the metal-molecule-metal junction we recorded 2361 consecutive traces, from which we build a conductance histogram. Figure 6.2 shows the conductance histograms built from all traces (without data selection). The zero of displacement of each trace is chosen at the point of rupture of the gold wire (first data point below 0.5 G_0). In the two-dimensional histogram (left side of figure 6.2) a high-count region is visible above 1 G_0, which we assign to transport through the gold wire. Below 1 G_0 one can distinguish two regions of high counts. The first region drops exponentially (straight on a logarithmic scale) from 10^{-4} G_0 to the noise level extending for about 0.5-1 nm. The second region stays constant around 10^{-4} G_0 and extends up to 1.5 nm. We assign the first region to through space tunneling between the electrodes and the second region to transport through the gold-molecule-gold junctions. This second region only appears when the molecule is drop cast on the sample and is not observed in clean samples (as can be seen in the figure 6.4 in the appendix). In addition, the length of the second region approximately matches the length of a single TYPI molecule, which is 1.85 nm in DFT calculations. To extract the mean conductance of the molecular junctions we plot the 1-D conductance histogram, as shown in the right panel of figure 6.2. The blue line is a histogram of the conductance including all traces, while the red line is a histogram with the tunneling region removed (further details in the appendix). Using a Gaussian function (green dashed line) to fit the conductance distribution without tunneling, we obtain $(1.3 \pm 0.4) \cdot 10^{-4}$ G_0 as most probable conduction value for TYPI.

To comment on the measured conductance value of TYPI, we compare it to the single-molecule conductance of the well-studied oligo(p-phenylene vinylene) trimer (OPV3)(figure 6.3b). This molecule has approximately the same length (1.92 nm compared to 1.85 nm of TYPI) and the same basic electronic structure, which consist of three conjugated rings connected with sp^2 hybridized linkers. The conductance of OPV3 with thiol anchoring groups lies between $1 \cdot 10^{-4}$ G_0 and $2 \cdot 10^{-4}$ G_0 for MCBJ setups[29, 30]. Comparing the conductance values of both TYPI and OPV3 shows that a thiophene ring with azomethine linkers has a comparable charge transport efficiency as a benzene ring with vinyl linking.

6.3. DISCUSSION

To further investigate the charge transport characteristics of TYPI, we performed density functional theory (DFT) calculations, combined with the Green's function (NEGF) formalism to obtain ground-state electronic structures and transmissions for TYPI, OPV3 and OPA3 (oligo(p-phenylene azomethine) trimer). For details concerning the calculations, see the appendix. OPA3 is included in the calculations to differentiate between the effect that the thiophene core and azomethine bond may have on transport.

Figure 6.3a-c show the isosurface of the Au-hybridized highest occupied molecular orbitals (HOMO) of TYPI, OPV3 and OPA3, respectively. It can be clearly seen that the HOMO's of all molecules have a π-character and closely resemble each other,

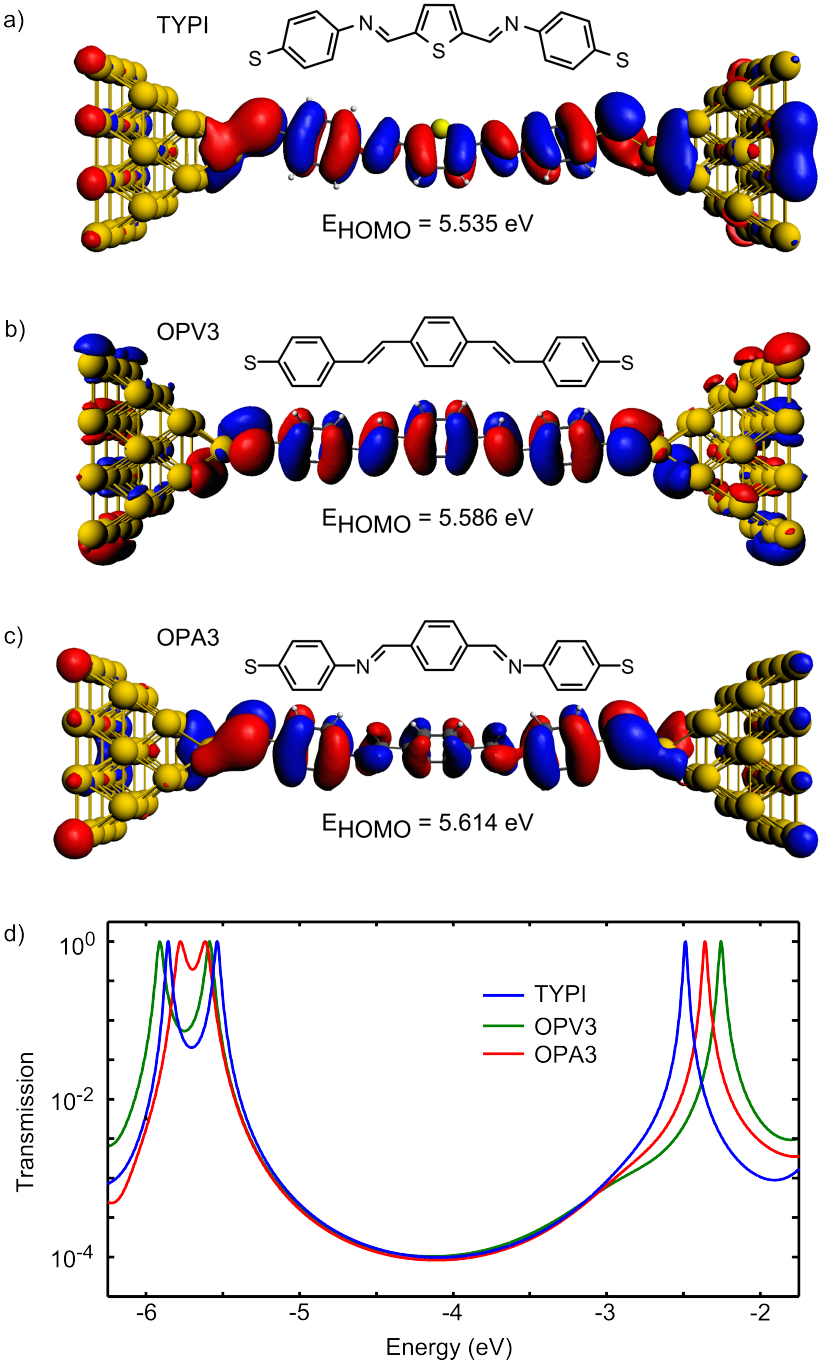

Figure 6.3: DFT + Σ calculations for TYPI, OPV3 and OPA3. a),b),c) Structure and hybridized HOMO orbital of respectively TYPI, OPV3 and OPA3. The energy of the HOMO is displayed underneath. d) Transmission as function of energy around the HOMO-LUMO gap for all three metal-molecule-metal junctions.

both in shape and in energy. They extend from one sulphur atom to the other and hybridize well with the gold atoms, as can be seen by the finite density around the gold-sulphur bond and their extension throughout the entire gold electrodes. The similar electronic structure is further supported by the transmission calculations, which show similar broadening of the HOMO's indicating comparable hybridization of the molecules with the gold electrodes. Furthermore, the HOMO-LUMO gap is of comparable size, 3.1 eV for TYPI, 3.3 eV for OPV3 and 3.3 eV for OPA3.

The calculated transmission of the three molecules is shown in figure 6.3d, where peaks in the transmission originate from resonant charge transport through molecular orbitals. Based on their energy, the overlapping peaks just below -5.5 eV can be identified, as the HOMO's of TYPI, OPV3 and OPA3. Focusing on the transmission in the region around the Fermi energy, which our calculations predict to be around -4.8 eV, we see that for all molecules transport is dominated by the HOMO. This is expected for thiol anchoring groups[31, 32]. Moreover, in the same energy range, the transmissions follow each other closely which is a result of the similar energy of the HOMO's and their broadening. This supports the conclusion drawn from the measurements, which is that the thiophene core with azomethine linker units has a comparable conductance to the benzene core with vinyl linking units.

The comparable conductance between OPA3 and TYPI in the calculations shows that inclusion of a thiophene core does not mask any potential negative effects the azomethine bond can have on the conductance as compared to the vinyl-linked analogue. This is further supported by comparing the transport through thiophene and phenyl units[33] which shows that despite conformational variations the conductance is approximately the same. This motivates the conclusion that the azomethine bond is of comparable conductance as a vinyl bond. The relatively poor charge mobilities that are reported for azomethines in the bulk are therefore considered to be the result of an unfavorable morphology and are not the result of a limited conductance of the azomethine bond.

In conclusion, an azomethine-based low molar mass molecule was synthesized and the conductance through single molecules was measured using a mechanically controlled break junction. The conductance was determined to be $(1.3 \pm 0.4) \cdot 10^{-4}$ G_0, which is comparable to reported values for OPV3, a vinyl-based analogue. This, in turn, shows that the azomethine bond exhibits good electrical conductance, making it a useful linker for the preparation of conjugated materials for electronic applications. Moreover, we believe that the simple chemistry combined with the good charge transporting properties make azomethine-based materials ideal candidates for various optoelectronic applications.

6.4. APPENDIX

BARE GOLD JUNCTIONS

Figure 6.4 shows the 2-D and 1-D conductance histogram of bare gold junctions, so before the TYPI dissolved in dichloromethane was drop cast. The conductance decreases gradually to around 1 G_0. Whereafter it jumps down to around 10^{-4} G_0, due to rupture of the last few atom contact and consecutive snapback of the electrodes. After rupture the conductance exponentially decreases to the noise level.

CONDUCTANCE HISTOGRAMS WITHOUT TUNNELING

Figure 6.5 shows the 2-D and 1-D conductance histogram of the junction with the solution drop cast (figure 6.2), however with the conductance traces identified as tunneling removed from the data set. All conductance traces that dropped from 10^{-1} G_0 to 10^{-5} G_0 in less then 1 nm electrode displacement have been identified as tunneling conductance traces and have been removed from the data set. The 2-D histogram clearly shows a region of high count that decreases slowly as function of electrode displacement, indicating that through space tunneling is not the main contribution to

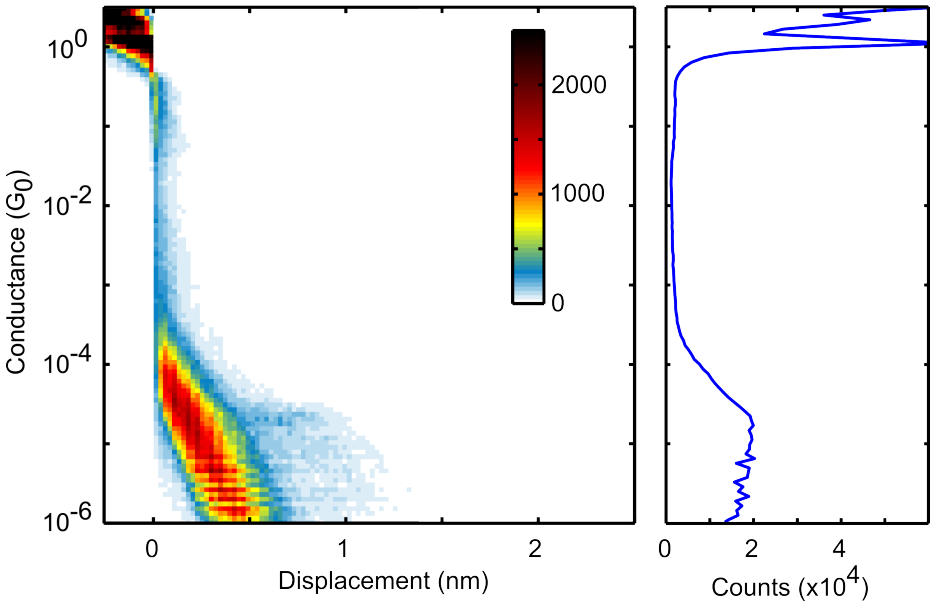

Figure 6.4: Conductance histograms of all breaking traces from a junction before deposition of the solution with molecules. All traces are aligned at 0.5 G_0. (Left Panel) Conductance-displacement histogram built from 4995 traces. The traces are binned logarithmic along the conductance (y) axis with 16 bins/decade and linearly binned along the displacement (x) axis with 40 bins/nm. Right panel) Conductance histogram, blue line is built by summing the histogram in the left panel along the displacement axis.

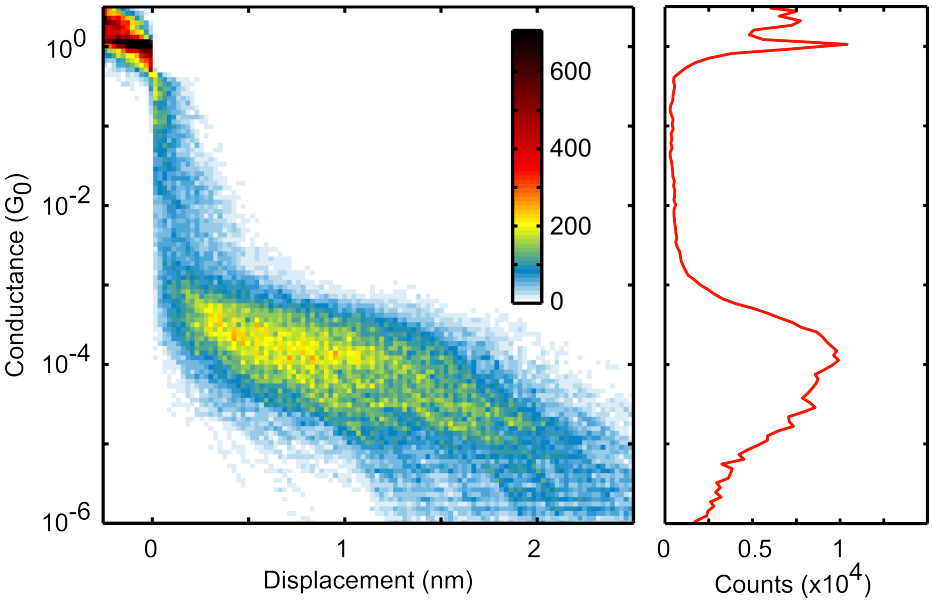

Figure 6.5: Conductance histograms with tunneling traces removed. All traces are aligned at 0.5 G_0. Left Panel) Conductance-displacement histogram built from 667 traces. The traces are binned logarithmic along the conductance (y) axis with 16 bins/decade and linearly binned along the displacement (x) axis with 40 bins/nm. Right panel) Conductance histogram, red line is built by summing the histogram in the left panel along the displacement axis.

the set of traces (for tunneling traces the conductance generally decays faster then 2 orders of magnitude per 1 nm electrode displacement). The length of TYPI (1,85 nm), matches with the approximate length of the traces shown in the histogram. Therefore we attribute the traces in figure 6.5 to the formation of a molecular junction between the gold tips.

DFT+Σ/NEGF CALCULATIONS

The DFT calculations were performed with the Amsterdam Density Functional (ADF) quantum chemistry package[34, 35]. All calculations used a generalized gradient approximation (GGA-PBE) as exchange correlation functional and a triple-ζ plus polarization (TZP) basis set. All electrons were considered, expect for the gold atoms were the frozen core approximation was used. To account for relativistic effects in the gold electrodes, the zeroth order regular approximation (ZORA) to the Dirac equation was employed.

All geometries were relaxed and converged to energy changes of less than $1 \cdot 10^{-3}$ hartree, energy gradients of less than $1 \cdot 10^{-3}$ hartree/Å and $6.7 \cdot 10^{-4}$ hartree/Å RMS. The transmissions through the junctions (figure 6.3d) were obtained using the non-

equilibrium Green's function (NEGF) formalism and coupling the outermost Au layer of each electrode to wide-band limit electrodes with a coupling strength of 1eV[36].

To correct for well-known electron correlation errors upon addition/removal of a charge on the molecule, the DFT + Σ method was used[37], implemented as a scissor operator. The Σ correction consists of two parts. First, a correction to the ionisation potential and electron affinity is calculated based on the anion and cation charge states of the molecule in gas phase. Second, image-charge effects were calculated for the different charge states (also in gas-phase). This was done using the atomic (Hirschfeld) charge distribution between two parallel plates (classic image charge model). The image planes were set at a distance of 1.3 Angstrom away from the bonding sulphur atoms.

To determine the transmission for the metal/molecule/metal junctions, it was calculated for multiple electrode separations by moving the electrodes outwards in steps of 0.02 Angstrom. At each step the geometry of the molecule in the previous electrode separation was used and then relaxed for the new electrode separation. For the new relaxed geometry the metal/molecule/metal transmission was calculated. This was repeated until the junction ruptured, signalled by a large drop in the transmission. The last Angstrom before the rupture was used to determine a transmission for the junctions, which is 50 individual transmissions in total. This formed a band of transmissions which is shown for each junction in figure 6.6 for 1 eV around the calculated fermi energy (-4.8 eV). The solid line is the transmission for the junction that crosses the median transmission value calculated from the value of all transmission curves at the fermi energy. This is also the transmission that is shown for each junction in figure 6.3d in the main article. Comparing all three molecules in figure 6.6 it can be seen that the bands overlap and that TYPI has the largest variation in transmission and OPA3 the smallest.

CHEMICAL CHARACTERIZATION AND SYNTHESIS OF TYPI, (THIOPHENE-2,5-DIYLBIS (N-PHENYLMETHANIMINE))

All chemicals were purchased from commercial sources and used as received unless stated otherwise. The structure was confirmed using ^{1}H-NMR (Bruker WM-400, 400 MHz). The recorded spectra were referenced to the solvent ($CDCl_3$: ^{1}H, 7.26 ppm) relative to TMS. The infrared spectrum was obtained with a PerkinElmer Spectrum 100 and the UV-vis spectrum was collected using a PerkinElmer Lambda 35 UV-vis spectrometer. The mass spectrum was generated by electron impact and data was collected over the *m/z* range 45–900. Mass spectra were recorded using a Shimadzu QP2010S with direct injection port.

2,5-Thiophenedicarboxaldehyde was purified by vacuum sublimation, prior to use. 4-aminobenzenethiol (339 mg, 2.7 mmol) and 2,5-thiophenedicarboxaldehyde (173 mg, 1.2 mmol) were placed in a dry round-bottom flask with reflux condenser under argon atmosphere. Dry chloroform (20 mL) was added, followed by a crystal of *p*-toluenesulfonic acid as a catalyst while stirring. The mixture turned yellow and was

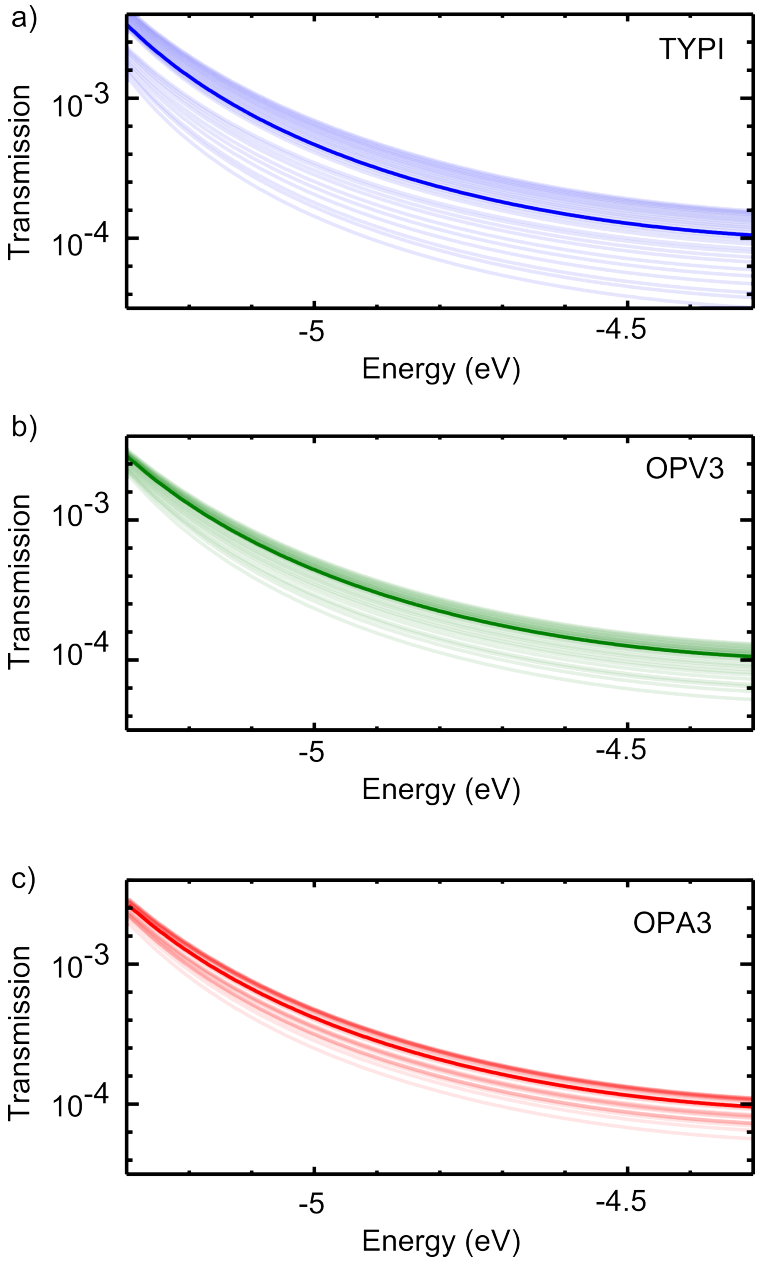

Figure 6.6: Variation in the transmission by changing the electrode separation by steps of 0.02 Å for 1 Å in total. The thick line is the transmission, which crosses the median transmission value at the fermi energy for all transmission curves. The lighter curves are individual transmissions for different electrode separations.

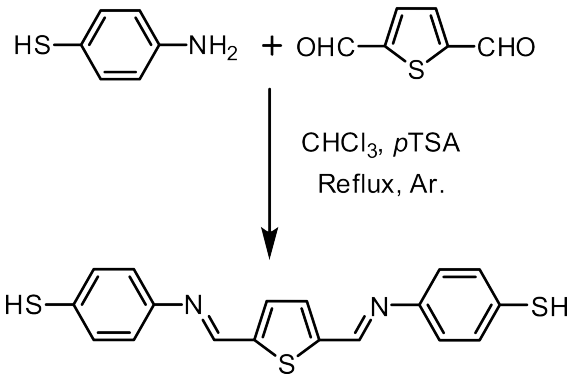

Figure 6.7: Synthesis of thiophene-2,5-diylbis(N-phenylmethanimine)

heated to reflux. A precipitate was formed overnight. After 3 days the reaction mixture was poured in methanol and filtered off. The product was washed with methanol, isopropanol, isopropanol:triethylamine (98:2) and again isopropanol and dried in vacuo. Yield 0.40 g (87%, 1.1 mmol). λ_{max} (CHCl3) = 398 nm; ^{1}H-NMR (CDCl3, 400MHz) δ 8.56 (s, 2H); 7.48 (s, 2H); 7.30 (d, J = 8.4Hz, 4H); 7.15 (d, J = 8.4Hz, 4H); 3.50 (s, 2H) ppm; FTIR: 3037, 2570, 1902, 1604, 1575, 1480, 1404, 1195, 828 cm^{-1}; MS m/z (relative intensity): 355.0 (24), 353.9 (M$^+$, 99), 321.0 (75), 217.9 (22), 136.0 (59), 109.0 (100), 108.0 (32), 77.1 (23), 69.0 (37), 65.1 (85), 45.1 (27).

REFERENCES

[1] M. Koole, R. Frisenda, M. L. Petrus, M. L. Perrin, H. S. J. van der Zant, and T. J. Dingemans, *Charge transport through conjugated azomethine-based single molecules for optoelectronic applications,* Org. Electron. **34**, 38 (2016).

[2] A. Mishra and P. Bäuerle, *Small molecule organic semiconductors on the move: Promises for future solar energy technology,* Angew. Chem. **51**, 2020 (2012).

[3] M. C. Gather, A. Köhnen, and K. Meerholz, *White organic light-emitting diodes,* Adv. Matter. **23**, 233 (2011).

[4] C. Wang, H. Dong, W. Hu, Y. Liu, and D. Zhu, *Semiconducting π-conjugated systems in field-effect transistors: A material odyssey of organic electronics,* Chem. Rev. **112**, 2208 (2012).

[5] V. K. Thakur, G. Ding, J. Ma, P. S. Lee, and X. Lu, *Hybrid materials and polymer electrolytes for electrochromic device applications,* Adv. Mater. **24**, 4071 (2012).

[6] Y.-J. Cheng, S.-H. Yang, and C.-S. Hsu, *Synthesis of conjugated polymers for organic solar cell applications,* Chem. Rev. **109**, 5868 (2009).

[7] K. T. Nielsen, K. Bechgaard, and F. C. Krebs, *Removal of palladium nanoparticles from polymer materials,* Macromolecules **38**, 658 (2005).

[8] T. P. Osedach, T. L. Andrew, and V. Bulovic, *Effect of synthetic accessibility on the commercial viability of organic photovoltaics,* Energ. Environ. Sci. **6**, 711 (2013).

[9] R. Po, G. Bianchi, C. Carbonera, and A. Pellegrino, *All that glisters is not gold?: An analysis of the synthetic complexity of efficient polymer donors for polymer solar cells,* Macromolecules **48**, 453 (2015).

[10] M. L. Petrus, R. K. M. Bouwer, U. Lafont, S. Athanasopoulos, N. C. Greenham, and T. J. Dingemans, *Small-molecule azomethines: organic photovoltaics via Schiff base condensation chemistry,* J. Mater. Chem. A **2**, 9474 (2014).

[11] J.-M. Lehn, *Conjecture: Imines as unidirectional photodriven molecular motors—motional and constitutional dynamic devices,* Chem. Eur. J. **12**, 5910 (2006).

[12] M. Bourgeaux, S. A. P. Guarin, and W. G. Skene, *Photophysical, crystallographic, and electrochemical characterization of novel conjugated thiopheno azomethines,* J. Mater. Chem. **17**, 972 (2007).

[13] M. Bourgeaux and W. G. Skene, *Photophysics and electrochemistry of conjugated oligothiophenes prepared by using azomethine connections,* J. Org. Chem. **72**, 8882 (2007).

[14] J. C. Hindson, B. Ulgut, R. H. Friend, N. C. Greenham, B. Norder, A. Kotlewski, and T. J. Dingemans, *All-aromatic liquid crystal triphenylamine-based poly(azomethine)s as hole transport materials for opto-electronic applications,* J. Mater. Chem. **20**, 937 (2010).

[15] A. Iwan, M. Palewicz, A. Chuchmała, L. Gorecki, A. Sikora, B. Mazurek, and G. Pasciak, *Opto(electrical) properties of new aromatic polyazomethines with fluorene moieties in the main chain for polymeric photovoltaic devices,* Synthetic Met. **162**, 143 (2012).

[16] A. Iwan, B. Boharewicz, K. Parafiniuk, I. Tazbir, L. Gorecki, A. Sikora, M. Filapek, and E. Schab-Balcerzak, *New air-stable aromatic polyazomethines with triphenylamine or phenylenevinylene moieties towards photovoltaic application,* Synthetic Met. **195**, 341 (2014).

[17] M. L. Petrus, R. K. M. Bouwer, U. Lafont, D. H. K. Murthy, R. J. P. Kist, M. L. Bohm, Y. Olivier, T. J. Savenije, L. D. A. Siebbeles, N. C. Greenham, and T. J. Dingemans, *Conjugated poly(azomethine)s via simple one-step polycondensation chemistry: synthesis, thermal and optoelectronic properties,* Polym. Chem. **4**, 4182 (2013).

[18] C. Moussalem, O. Segut, F. Gohier, M. Allain, and P. Frère, *Facile access via green procedures to a material with the benzodifuran moiety for organic photovoltaics,* ACS Sustainable Chem. Eng. **2**, 1043 (2014).

[19] M. L. Petrus, T. Bein, T. J. Dingemans, and P. Docampo, *A low cost azomethine-based hole transporting material for perovskite photovoltaics,* J. Mater. Chem. A **3**, 12159 (2015).

[20] H.-J. Niu, Y.-D. Huang, X.-D. Bai, and X. Li, *Novel poly-Schiff bases containing 4,4-diamino-triphenylamine as hole transport material for organic electronic device,* Mater. Lett. **58**, 2979 (2004).

[21] D. Islangek, C. Santato, S. Barik, and W. Skene, *Charge-carrier transport in thin films of π-conjugated thiopheno-azomethines,* Org. Electron. **13**, 3022 (2012).

[22] M. E. Mulholland, D. Navarathne, M. L. Petrus, T. J. Dingemans, and W. G. Skene, *Correlating on-substrate prepared electrochromes with their solution processed counterparts - towards validating polyazomethines as electrochromes in functioning devices,* J. Mater. Chem. C **2**, 9099 (2014).

[23] X. Ma, H. Niu, H. Wen, S. Wang, Y. Lian, X. Jiang, C. Wang, X. Bai, and W. Wang, *Synthesis, electrochromic, halochromic and electro-optical properties of polyazomethines with a carbazole core and triarylamine units serving as functional groups,* J. Mater. Chem. C **3**, 3482 (2015).

[24] M. L. Petrus, F. S. F. Morgenstern, A. Sadhanala, R. H. Friend, N. C. Greenham, and T. J. Dingemans, *Device performance of small-molecule azomethine-based bulk heterojunction solar cells,* Chem. Mater. **27**, 2990 (2015).

[25] A. Bolduc, A. Al Ouahabi, C. Mallet, and W. G. Skene, *Insight into the isoelectronic character of azomethines and vinylenes using representative models: A spectroscopic and electrochemical study,* J. Org. Chem. **78**, 9258 (2013).

[26] C. A. Martin, R. H. M. Smit, R. v. Egmond, H. S. J. van der Zant, and J. M. van Ruitenbeek, *A versatile low-temperature setup for the electrical characterization of single-molecule junctions,* Rev. Sci. Instrum. **82**, 053907 (2011).

[27] C. Untiedt, A. I. Yanson, R. Grande, G. Rubio-Bollinger, N. Agraït, S. Vieira, and J. van Ruitenbeek, *Calibration of the length of a chain of single gold atoms,* Phys. Rev. B **66**, 085418 (2002).

[28] S. Wu, M. T. Gonzalez, R. Huber, S. Grunder, M. Mayor, C. Schonenberger, and M. Calame, *Molecular junctions based on aromatic coupling,* Nat. Nano. **3**, 569 (2008).

[29] R. Huber, M. T. González, S. Wu, M. Langer, S. Grunder, V. Horhoiu, M. Mayor, M. R. Bryce, C. Wang, R. Jitchati, C. Schönenberger, and M. Calame, *Electrical conductance of conjugated oligomers at the single molecule level,* J. Am. Chem. Soc. **130**, 1080 (2008).

[30] C. R. Arroyo, R. Frisenda, K. Moth-Poulsen, J. S. Seldenthuis, T. Bjørnholm, and H. S. van der Zant, *Quantum interference effects at room temperature in opv-based single-molecule junctions,* Nanoscale Res. Lett. **8**, 1 (2013).

[31] Kim, J. M. Beebe, Y. Jun, X.-Y. Zhu, and C. D. Frisbie, *Correlation between homo alignment and contact resistance in molecular junctions: Aromatic thiols versus aromatic isocyanides,* J. Am. Chem. Soc. **128**, 4970 (2006).

[32] R. Cohen, K. Stokbro, J. M. L. Martin, and M. A. Ratner, *Charge transport in conjugated aromatic molecular junctions: Molecular conjugation and molecule-electrode coupling,* J. Phys. Chem. C **111**, 14893 (2007).

[33] E. J. Dell, B. Capozzi, K. H. DuBay, T. C. Berkelbach, J. R. Moreno, D. R. Reichman, L. Venkataraman, and L. M. Campos, *Impact of molecular symmetry on single-molecule conductance,* J. Am. Chem. Soc. **135**, 11724 (2013).

[34] C. Fonseca Guerra, J. G. Snijders, G. te Velde, and E. J. Baerends, *Towards an order-N DFT method,* Theor. Chem. Acc. **99**, 391 (1998).

[35] G. te Velde, F. M. Bickelhaupt, E. J. Baerends, C. Fonseca Guerra, S. J. A. van Gisbergen, J. G. Snijders, and T. Ziegler, *Chemistry with ADF,* J. Comput. Chem. **22**, 931 (2001).

[36] C. J. O. Verzijl, J. S. Seldenthuis, and J. M. Thijssen, *Applicability of the wide-band limit in DFT-based molecular transport calculations,* J. Chem. Phys. **138**, 094102 (2013).

[37] P. Darancet, J. R. Widawsky, H. J. Choi, L. Venkataraman, and J. B. Neaton, *Quantitative current–voltage characteristics in molecular junctions from first principles,* Nano Lett. **12**, 6250 (2012).

7

OUTLOOK

In this chapter the challenges and opportunities of quantum interference and nearly degenerate orbitals in molecular electronics are discussed. An increase in the effectiveness of gate coupling is deemed essential to study these effects in more detail; a few promising approaches for this are suggested. Furthermore, a proposal is given for a single-molecule junction that combines degenerate orbitals and quantum interference to study single-electron tunneling events.

One of the main selling points of molecular electronics is the promise to create electrical components smaller than those fabricated with semiconductor materials[1]. However, in the last decade the innovations in silicon technology have been impressive and nowadays components are fabricated with dimensions down to the 10 nm scale. It is therefore unlikely that for a fundamental component like a transistor, the use of a single molecule can be of a significant advantage. The present opportunities in molecular electronics lie in designing electronic components with functionality difficult to achieve with silicon technology. An example of this is the use of quantum interference to create devices which show a larger thermo-electric effect than possible in silicon technology[2].

Another application of molecular electronics is in the field of organic electronics. In the last few decades organic light-emitting diodes have become widespread[3] and the research field of photovoltaics with organic molecules has grown significantly[4]. These fields do not directly capitalize on a single molecule, but rather on the properties of bulk or thin films of organic materials. The difficulty in designing organic electronic materials is that effects on multiple length scales should be taken into account, ranging from the collective action of the bulk, the interaction between the molecules, down to the processes that happen inside the molecule itself. It is at the single-molecule level that molecular electronics can contribute[5]. An example of this is shown in chapter 6, where organic solar cells show promising efficiency in converting light to charge, but the mobility of the electrons in the bulk is low. The question posed is if the low mobility is from an inter- or intra-molecular origin. The mechanically controlled breakjunction was used to study the conductance of a single molecule demonstrating a level of conductance consistent with a relative easy transfer of electrons along the molecule. This suggests that the low mobility in bulk has an inter-molecular origin.

In the rest of this chapter we will discuss some aspects concerning the opportunities and challenges of research on quantum interference and degenerate orbitals in single molecules. We show that both fields could lead to novel single-molecule components or contribute to our understanding of electron transport in organic electronics. We will see that the existing gate electrode technologies are a limiting factor in investigation of both effects. A few promising alternatives are therefore discussed. Furthermore, quantum interference and degenerate orbitals are combined in a single molecule to propose a single molecule junction capable of detecting single electron tunneling events.

7.1. QUANTUM INTERFERENCE

Quantum interference has been one of the main research topics in molecular electronics. The small size of a single-molecule junction makes it possible for the orbitals of the molecule to influence the phase of the electrons passing through it in a well defined manner. This is much more difficult to achieve in semiconductor quantum dots, due to the limited control of the shape of the dot[6]. Quantum interference can

be useful in designing molecules, as it for example provides a method with which conjugation can be preserved in a molecule, but inhibit the movement of electrons across it. On the single-molecule scale this can be applied in for example dielectrics[7], as quantum interference keeps the polarizability of a conjugated system, but impedes the flow of electrons. In organic bulk materials it could be possible to use quantum interference to limit the flow of electrons in certain areas of the material, but still be able to use conjugated structures to design the material.

However, there are significant open questions concerning quantum interference in charge transport through single molecules. As shown in theory chapter 2 and in Solomon *et al.* [8], a correctly coupled two-site model will show suppression of the transmission between two orbitals and the appearance of the characteristic logarithmic quantum interference dip. Translating this theoretical model to a prediction of the features that can be expected in a realistic junction is difficult. First, most research has taken an effective single-particle NEGF approach to calculate the off-resonant transmission through a molecule. How does quantum interference in transport look like if second-order co-tunneling is included[6] and what happens when the molecule is not strongly coupled to the electrodes? Secondly, how many destructive interference dips are present in off-resonant transport and where are they in energy? Research has shown that the exact structure and composition of the molecules can influence the dip's location in energy[9]. Electron-electron interactions can also play a significant role, resulting in multiple interference dips in off-resonant transport[6]. Lastly, can the logarithmic dip be observed? Temperature, vibrations[10, 11] and contributions from the σ-system[12] can play a significant role in transport and may therefore suppress the appearance of logarithmic dips in low-bias transport.

Further experiments on quantum interference are therefore crucial in validating which predictions are correct. At this moment a measurement of the low-bias conductance as a function of energy showing signs of quantum interference would be the most relevant data in supporting theoretical predictions. However, this proves to be challenging as the only evidence of a dip being present has been reported in the bias dependence of self-assembled monolayers[13, 14]. The difficulty often lies in the limited gate coupling of a single-molecule junction. Improvements to the limited gate coupling will be discussed in section 7.3.

There are some promising approaches to increase the sensitivity to detect the presence of a quantum interference dip in transport. One approach, already introduced in chapter 5, is the use of Kondo correlations as a means to observe quantum interference. It is predicted that these Kondo correlations are suppressed at the energy of the quantum interference dip[15]. Tentative evidence of this can be seen in Fock *et al.* [16] and in the inset of figure 3.5b in chapter 3. Another approach could be to directly measure the slope of the low-bias transmission using thermo-power[17]. Lastly if the interference dip is located close to a charge degeneracy point, it can interfere with the shape of the resonance peak of the molecule[18]. As a consequence the peak shape changes and from this distorted resonance-peak information about

the dip could in principle be extracted. The measurements of chapter 3 could potentially be reinterpreted in this way.

7.2. DEGENERATE ORBITALS

In chapter 4 and 5 we discussed transport through molecules which possess a pair of nearly degenerate orbitals. This orbital degree of freedom makes it possible for singlet-triplet physics to occur at relatively low-energies. As the other energy scales are large due to the small size of the molecule, the singlet-triplet features are isolated from them (e.g. resonant transport). This makes these molecules an interesting system to study features such as singlet to triplet transitions and spin-1 Kondo effects[19].

In chapter 4 we showed that a non-conjugated barrier in a molecule may result in degenerate orbitals by effectively creating a double quantum dot in the molecule. As can be seen in the field of semiconductor quantum dots[20, 21], it opens the way to study physical processes in molecules not possible when only a single dot is present. For example, a double quantum dot molecule under irradiation should show photon assisted tunneling[22], making it possible to determine the tunnel coupling between the two dots and study excited state decay mechanisms. Significantly weakening the coupling between the dots and between the molecule and the electrodes, could lead to Pauli-spin blockade[23]. In such a case the current through the molecule is suppressed when two electrons are in the triplet state compared to the singlet state. Information can then be gained about the spin state of the molecule. This creates the opportunity to study spin-relaxation mechanisms and the possibility to create spin qubits where the physical surrounding can be engineered on an atomic scale using organic synthesis.

For both the excited state and spin-dependent relaxation mechanisms, techniques have been developed to study them in ensembles of molecules. However, in our proposed experiments, interactions between molecules and averaging over all molecules present is eliminated. As a consequence features may appear that are masked in bulk experiments. This makes the formation of nearly degenerate orbitals and double quantum dots in single molecules an interesting avenue to explore in the future.

7.3. GATE ELECTRODE

Improving the gate efficiency makes it possible to study features at a larger range of energies. Crucial in for example quantum interference experiments and results in an increased ability to tune the orbitals to a favorable configuration necessary to observe for example Pauli-spin blockade in double quantum dots. In single-molecule junctions formed with the electromigration technique, the effect of the gate on the molecule is generally small compared to the level spacing. The source and drain electrodes play an important role in the limited effect of the gate[24]. As the electrodes are metals they screen the electric potential, this is shown in figure 7.1. A spatial map

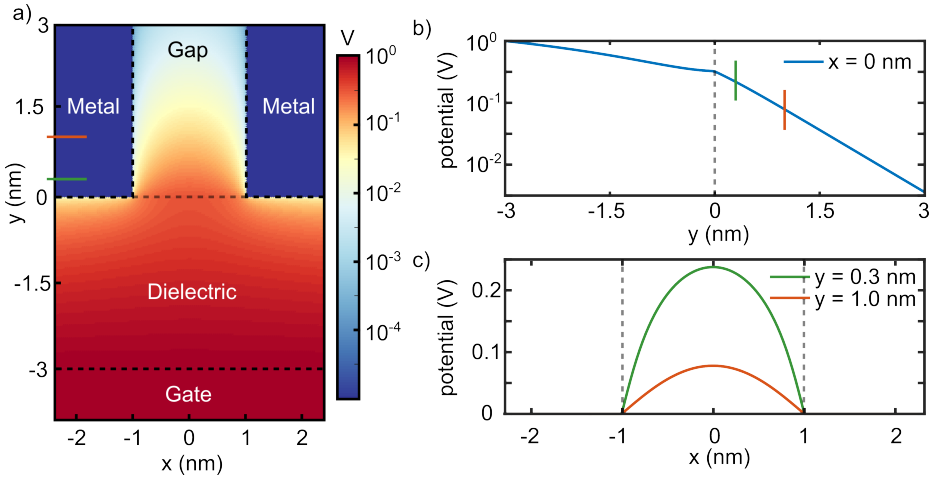

Figure 7.1: Numerical calculation of the electric potential in a metal-vacuum-metal junction. a) Electric potential map on a logarithmic scale. The dielectric ($\epsilon_r = 10$) is chosen to be 3 nm thick, across which a gate voltage of 1 V is applied. For $y > 0$ nm, the gap is present with on both sides grounded electrodes; gap size is 2 nm. b) Dependence of the electric potential as a function of y at $x = 0$ nm (middle of the gap). Dashed line is the interface between the dielectric and the vacuum gap. c) Electric potential in the gap as a function of x for two different distances from the dielectric. Distances are marked in b) and c). Dashed lines are the electrodes.

of the electric potential is shown in panel a); a voltage of 1 V is applied to the gate (below $y = -3$ nm). The electric potential decreases less than one order of magnitude in the dielectric, however when it comes into the gap (above $y = 0$ nm) it decays significantly quicker. This is seen more clearly in panel b), which shows the electric potential at $x = 0$ nm (on a logarithmic scale) as a function of distance from the gate. A clear change in the exponential decrease is visible in the gap ($y > 0$ nm). Panel c) shows that the strength of the potential varies with distance from the electrodes. It is significantly stronger in the middle of the gap, compared to a location near the electrodes.

The calculations in figure 7.1 show that the largest contribution to a low gate-coupling is the screening of the electrodes. Using thinner dielectrics could improve the gate efficiency, but if the molecule is not located at the dielectric interface it is futile. Thinner gold electrodes are not possible, as going below 10 nm thickness results in discontinuous films[25]. In the following we will discuss three alternative approaches to create single-molecule junctions with a more effective gate.

ELECTROCHEMICAL GATE

An approach to increase the gate efficiency is to change the method of gating and use an electrochemical gate[26]. In liquid, ions can move, making it possible to let these

ions surround the molecule resulting in a shift of the molecule's potential. Measuring the low-bias conductance of a single molecule continuously as a function of electrochemical gate is difficult due to the limited stability of the molecular junction. It has been achieved in only a few experiments[27]. Statistically determining the conductance at different gate potentials has on the other hand already been performed more often, for example on the quinone molecule[28]. Although it is possible to achieve a higher gate efficiency than electromigration junctions, there are a few drawbacks with electrochemical gating. First, the molecule will be surrounded by the electrolyte containing the ions. For systems where relaxation mechanisms are studied, as proposed in the double quantum dot molecule, the extra interaction (as compared to vacuum in electromigration junctions) is undesirable. Second, as the gate is a liquid, it will not be possible to gate at cryogenic temperatures due to freezing. This would make electrochemical gating unsuitable for double quantum dots and the study of its low-energy excitations. For the study of quantum interference at room temperature electrochemical gating can be a viable alternative, as low temperatures are not crucial to observe the expected conductance decrease due to destructive interference.

GRAPHENE

A second alternative is the use of graphene electrodes[29] instead of gold electrodes. A single layer of graphene (thickness 0.3 ~ 0.4 nm) can significantly decrease the screening of the gate electrode. In this Ph.D. research, experiments have been performed on molecular junctions with single- and multi-layer graphene electrodes. Preliminary data for multi-layer graphene electrodes is shown in figure 7.2. Here, the graphene was electroburned[29], whereafter a peptide coupling reaction[30] was used to bridge the gap with a molecule. Figure 7.2a shows a graphene flake on which the device layout is drawn with in green the graphene bridges that are to be etched and the gold electrodes in white. These junctions have a starting resistance in the order of 5 KΩ; after electroburning the junctions have a resistance at cryogenic temperature of approximately 100 GΩ (blue line in figure 7.2b). Performing an amide coupling reaction between the carboxyl groups possibly present at the graphene edges and the amine terminated terphenyl molecule (inset figure 7.2b), results in the green current-voltage trace. It presents a significant increase in current and non-linear features. The differential conductance map of this junction is shown in panel c) and shows charge degeneracy points forming a coulomb-diamond pattern. Focusing on a single charge degeneracy point in panel d), it can be seen that an asymmetric coupling is present.

The challenge of these measurements is to prove that the observed transport features are actually from a molecule. The electroburning technique itself can cause quantum dots[31] with charging energies of the same order as expected of a single molecule. Even in the graphene electrodes (especially when single-layer graphene is used) quantum dots can form[32]. Although some approaches have been tried to identify molecular features in transport through the junctions, for example, by looking at the excitation spectra[33] or by comparing transport features to a molec-

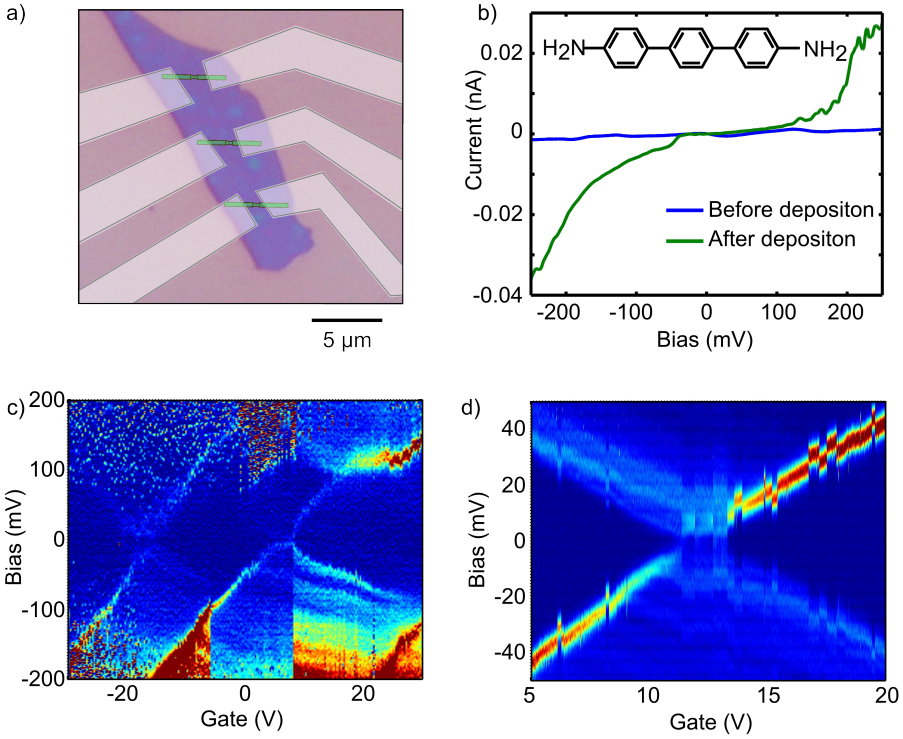

Figure 7.2: Preliminary data on graphene nano-gaps possibly bridged by covalently bound terphenyl. a) Optical image of a multi-layer graphene flake. The white area will be where the Au electrodes are deposited and the green areas the three graphene bridges, the rest of the graphene flake will be etched away. b) IV curves taken at T = 4 K. Blue curve is taken after electroburning. The green curve is taken after performing the peptide coupling reaction with terphenyl (shown at the top). c) Differential conductance map of the graphene junction after performing the peptide coupling reaction with terphenyl. d) Same sample as in c), however now zoomed in on the right charge degeneracy point. A gate coupling of $\alpha = 3$ mV/V and an asymmetric electrode coupling of $\Gamma_S = 8$ mV and $\Gamma_D = 2.5$ mV can be extracted.

ular junction with gold electrodes[34], it still remains challenging to identify without doubt their molecular origin. Another important consideration, especially for single-layer graphene, is that the graphene itself has a more complex electronic structure than gold. Examples are the Dirac cone and localized edge states[35]. These can result in a convolution with the molecular signatures in transport, making it a challenge to identify features of the molecule and study them.

MOLECULAR ORBITALS

An ineffective gate coupling can also be addressed by improving the molecule and not the experimental technique. An example is already given in chapter 5, where there is

strong differential gating. A suggested explanation for the differential gating is that two orbitals are localized at different locations on the molecule. One is located close to the electrodes, where the electric potential of the gate is screened, and the other is localized in the middle of the molecule and is therefore less affected by the screening properties of the electrodes. Extending this method, it is possible to design molecules where the frontier orbitals are localized at the center of the molecule. This could be an interesting solution for constructing weakly coupled double quantum dots in molecules for Pauli spin-blockade, as localizing the orbitals would possibly result in the weak coupling needed for spin-blockade. Another option would be to lengthen the molecule, resulting in the possibility to use a larger gap between the electrodes and therefore decrease the screening of the gate electrode, however in that case the current levels will be lower.

7.4. CONCLUSION

To conclude, both the research on quantum interference and degenerate orbitals in molecules show potential for further study. At this moment the gate electrode is a limiting factor. Different approaches exist to improve the gate coupling; each has its advantages and drawbacks. In case of quantum interference, as it is present at room-temperature, electrochemical gating could be an interesting approach to take. For double quantum dots and the study of relaxation mechanisms in a single molecule, a smart design of molecular orbitals is the most promising route.

When further knowledge is gained on the effects of interacting orbitals it would be interesting to design molecules which incorporate both quantum interference and nearly degenerate orbitals. An idea could be to use the sensitivity of quantum interference to detect single electron tunneling events. Figure 7.3 shows an implementation of this. In the top panels a single molecule in between electrodes is shown which is divided in two sections (labeled 'sens' and 'stub') weakly connected by a bridge. The part, labeled 'sens', is strongly coupled to the electrodes and displays quantum interference effects as studied in chapter 3; the off-resonant current through this section of the molecule will dependent on its charge state. The second part, labeled 'stub', is weakly coupled to the 'sens' part (coupling 'stub' to 'sens' (Γ_b) should be significantly smaller than the coupling of 'sens' to the electrodes (Γ)). Each section of the molecule therefore has its own chemical potential; these can be shifted relative to each other by differential gating (e.g. chapter 5). If we charge the molecule with a single electron, then the current through the molecule will depend on where that electron is located. Following the behavior of anthraquinone shown in chapter 3, if the electron is on the 'stub', 'sens' is not charged and current will be low due to destructive quantum interference (left panel). If the electron is on the 'sens' part of the molecule then it is charged, destructive quantum interference will be suppressed, and current will be high (right panel).

If the electron transfer rate between the two regions is low enough, then it could be possible to measure a single electron tunnelling event in a molecule as shown in

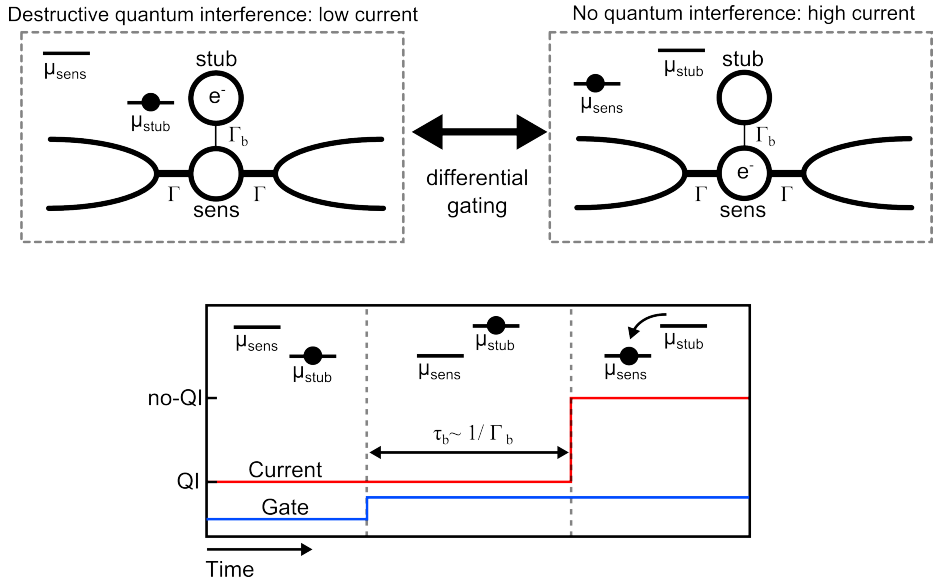

Figure 7.3: Charge sensing with quantum interference. Top panels: the left panel shows the molecule with two regions, were the sens region is bridging the electrodes. The electron is in the stub region, quantum interference is present in the sens region, current is thus low. The right panel shows that upon differential gating the molecule, the electron can be moved to the sense region, quantum interference is lifted and current is high. Bottom panel: if the electron transfer between the two regions is low enough, then there will be a delay between the moment of differential gating and movement of the electron resulting in the increase of current. This makes it possible to detect a single electron tunneling event in a time resolved manner.

the lower panel. Starting with the electron on the 'stub', the gate voltage is changed to make it energetically favourable for the electron to tunnel to the 'sense' region of the molecule. After some time depending on the electron transfer rate of the bridge ($\tau_b = \hbar/\Gamma_b$), the electron will move to the 'sens' region increasing the current by lifting the destructive quantum interference. To detect single tunneling events the time between two tunneling events (τ_b) should be of the same order as the time resolution of the measurement setup. In single-electron tunneling experiments with a semiconductor quantum dot capacitivily coupled to a quantum point contact a time resolution of a microseconds can be reached[36]. A nanometer long non-conjugated androstane bridge can give a tunneling rate of the order of $1 \cdot 10^6$[37] electrons per second. This suggests that it could be possible to observe a single tunneling event in a time resolved manner by using conjugation to define functionality in a single molecule.

REFERENCES

[1] R. M. Metzger, *Unimolecular electronics,* Chem. Rev. **115**, 5056 (2015).

[2] M. Strange, J. S. Seldenthuis, C. J. O. Verzijl, J. M. Thijssen, and G. C. Solomon, *Interference enhanced thermoelectricity in quinoid type structures,* J. Chem. Phys. **142**, 084703 (2015).

[3] J. Zaumseil and H. Sirringhaus, *Electron and ambipolar transport in organic field-effect transistors,* Chem. Rev. **107**, 1296 (2007).

[4] A. Facchetti, *Polymer donor–polymer acceptor (all-polymer) solar cells,* Mater. Today **16**, 123 (2013).

[5] J. Z. Low, S. N. Sanders, and L. M. Campos, *Correlating structure and function in organic electronics: From single molecule transport to singlet fission,* Chem. Mater. **27**, 5453 (2015).

[6] K. G. L. Pedersen, M. Strange, M. Leijnse, P. Hedegård, G. C. Solomon, and J. Paaske, *Quantum interference in off-resonant transport through single molecules,* Phys. Rev. B **90**, 125413 (2014).

[7] J. P. Bergfield, H. M. Heitzer, C. Van Dyck, T. J. Marks, and M. A. Ratner, *Harnessing quantum interference in molecular dielectric materials,* ACS Nano **9**, 6412 (2015).

[8] G. C. Solomon, D. Q. Andrews, T. Hansen, R. H. Goldsmith, M. R. Wasielewski, R. P. Van Duyne, and M. A. Ratner, *Understanding quantum interference in coherent molecular conduction,* J. Chem. Phys. **129**, 054701 (2008).

[9] D. Q. Andrews, G. C. Solomon, R. P. Van Duyne, and M. A. Ratner, *Single molecule electronics: Increasing dynamic range and switching speed using cross-conjugated species,* J. Am. Chem. Soc. **130**, 17309 (2008).

[10] T. Markussen and K. S. Thygesen, *Temperature effects on quantum interference in molecular junctions,* Phys. Rev. B **89**, 085420 (2014).

[11] C. Bessis, M. L. Della Rocca, C. Barraud, P. Martin, J. C. Lacroix, T. Markussen, and P. Lafarge, *Probing electron-phonon excitations in molecular junctions by quantum interference,* Scientific Reports **6**, 20899 (2016).

[12] G. C. Solomon, D. Q. Andrews, R. P. Van Duyne, and M. A. Ratner, *Electron transport through conjugated molecules: When the π system only tells part of the story,* ChemPhysChem **10**, 257 (2009).

[13] C. M. Guedon, H. Valkenier, T. Markussen, K. S. Thygesen, J. C. Hummelen, and S. J. van der Molen, *Observation of quantum interference in molecular charge transport,* Nat. Nano. **7**, 305 (2012).

[14] V. Rabache, J. Chaste, P. Petit, M. L. Della Rocca, P. Martin, J.-C. Lacroix, R. L. McCreery, and P. Lafarge, *Direct observation of large quantum interference effect in anthraquinone solid-state junctions,* J. Am. Chem. Soc. **135**, 10218 (2013).

[15] A. K. Mitchel, K. G. L. Pedersen, P. Hedegård, and J. Paaske, *Kondo blockade due to quantum interference in single-molecule junctions,* unpublished (2016).

[16] J. Fock, M. Leijnse, K. Jennum, A. S. Zyazin, J. Paaske, P. Hedegård, M. Brøndsted Nielsen, and H. S. J. van der Zant, *Manipulation of organic polyradicals in a single-molecule transistor,* Phys. Rev. B **86**, 235403 (2012).

[17] P. Reddy, S.-Y. Jang, R. A. Segalman, and A. Majumdar, *Thermoelectricity in molecular junctions,* Science **315**, 1568 (2007).

[18] J. P. Bergfield, P. Jacquod, and C. A. Stafford, *Coherent destruction of coulomb blockade peaks in molecular junctions,* Phys. Rev. B **82**, 205405 (2010).

[19] S. Florens, A. Freyn, N. Roch, W. Wernsdorfer, F. Balestro, P. Roura-Bas, and A. A. Aligia, *Universal transport signatures in two-electron molecular quantum dots: gate-tunable Hund's rule, underscreened Kondo effect and quantum phase transitions,* J. Phys. Condens. Mater. **23**, 243202 (2011).

[20] W. G. van der Wiel, S. De Franceschi, J. M. Elzerman, T. Fujisawa, S. Tarucha, and L. P. Kouwenhoven, *Electron transport through double quantum dots,* Rev. Mod. Phys. **75**, 1 (2002).

[21] R. Hanson, L. P. Kouwenhoven, J. R. Petta, S. Tarucha, and L. M. K. Vandersypen, *Spins in few-electron quantum dots,* Rev. Mod. Phys. **79**, 1217 (2007).

[22] L. P. Kouwenhoven, S. Jauhar, J. Orenstein, P. L. McEuen, Y. Nagamune, J. Motohisa, and H. Sakaki, *Observation of photon-assisted tunneling through a quantum dot,* Phys. Rev. Lett. **73**, 3443 (1994).

[23] K. Ono, D. G. Austing, Y. Tokura, and S. Tarucha, *Current rectification by Pauli exclusion in a weakly coupled double quantum dot system,* Science **297**, 1313 (2002).

[24] S. S. Datta, D. R. Strachan, and A. T. C. Johnson, *Gate coupling to nanoscale electronics,* Phys. Rev. B **79**, 205404 (2009).

[25] M. Walther, D. G. Cooke, C. Sherstan, M. Hajar, M. R. Freeman, and F. A. Hegmann, *Terahertz conductivity of thin gold films at the metal-insulator percolation transition,* Phys. Rev. B **76**, 125408 (2007).

[26] W. Haiss, H. van Zalinge, S. J. Higgins, D. Bethell, H. Höbenreich, D. J. Schiffrin, and R. J. Nichols, *Redox state dependence of single molecule conductivity,* J. Am. Chem. Soc. **125**, 15294 (2003).

[27] X. Li, B. Xu, X. Xiao, X. Yang, L. Zang, and N. Tao, *Controlling charge transport in single molecules using electrochemical gate,* Faraday Discuss. **131**, 111 (2006).

[28] M. Baghernejad, X. Zhao, K. Baruël Ørnsø, M. Füeg, P. Moreno-García, A. V. Rudnev, V. Kaliginedi, S. Vesztergom, C. Huang, W. Hong, P. Broekmann, T. Wandlowski, K. S. Thygesen, and M. R. Bryce, *Electrochemical control of single-molecule conductance by Fermi-level tuning and conjugation switching,* J. Am. Chem. Soc. **136**, 17922 (2014).

[29] F. Prins, A. Barreiro, J. W. Ruitenberg, J. S. Seldenthuis, N. Aliaga-Alcalde, L. M. K. Vandersypen, and H. S. J. van der Zant, *Room-temperature gating of molecular junctions using few-layer graphene nanogap electrodes,* Nano Lett. **11**, 4607 (2011).

[30] X. Guo, J. P. Small, J. E. Klare, Y. Wang, M. S. Purewal, I. W. Tam, B. H. Hong, R. Caldwell, L. Huang, S. O'Brien, J. Yan, R. Breslow, S. J. Wind, J. Hone, P. Kim, and C. Nuckolls, *Covalently bridging gaps in single-walled carbon nanotubes with conducting molecules,* Science **311**, 356 (2006).

[31] J. Moser and A. Bachtold, *Fabrication of large addition energy quantum dots in graphene,* Appl. Phys. Lett. **95**, 173506 (2009).

[32] J. Güttinger, F. Molitor, C. Stampfer, S. Schnez, A. Jacobsen, S. Dröscher, T. Ihn, and K. Ensslin, *Transport through graphene quantum dots,* Rep. Prog. Phys. **75**, 126502 (2012).

[33] E. Burzurí, J. O. Island, R. Díaz-Torres, A. Fursina, A. González-Campo, O. Roubeau, S. J. Teat, N. Aliaga-Alcalde, E. Ruiz, and H. S. J. van der Zant, *Sequential electron transport and vibrational excitations in an organic molecule coupled to few-layer graphene electrodes,* ACS Nano **10**, 2521 (2016).

[34] K. Ullmann, P. B. Coto, S. Leitherer, A. Molina-Ontoria, N. Martín, M. Thoss, and H. B. Weber, *Single-molecule junctions with epitaxial graphene nanoelectrodes,* Nano Lett. **15**, 3512 (2015).

[35] Y. Niimi, T. Matsui, H. Kambara, K. Tagami, M. Tsukada, and H. Fukuyama, *Scanning tunneling microscopy and spectroscopy of the electronic local density of states of graphite surfaces near monoatomic step edges,* Phys. Rev. B **73**, 085421 (2006).

[36] L. M. K. Vandersypen, J. M. Elzerman, R. N. Schouten, L. H. W. van Beveren, R. Hanson, and L. P. Kouwenhoven, *Real-time detection of single-electron tunneling using a quantum point contact,* Applied Physics Letters **85**, 4394 (2004).

[37] G. L. Closs, L. T. Calcaterra, N. J. Green, K. W. Penfield, and J. R. Miller, *Distance, stereoelectronic effects, and the Marcus inverted region in intramolecular electron transfer in organic radical anions,* J. Phys. Chem. **90**, 3673 (1986).

SUMMARY

The investigation of new electronic materials drives the development of electrical devices and component. In the field of molecular electronics electron transport through single molecules is studied. The main goals of molecular electronics are to facilitate the design electronic materials with molecules and develop components on a single-molecule scale. This thesis is mostly about using the electromigration technique to experimentally investigate electron transport through a family of three anthracene-like molecules, each with a different side-group at the central ring.

Using oxygen side-groups (chapter 3) results in an anthraquinone like molecule, which in between gold electrodes shows an order of magnitude difference in off-resonant conductance between two charge states. The explanation supported by theoretical calculations is that upon adding an electron to the molecule destructive quantum interference is lifted, thus increasing the conductance.

In chapter 4 two hydrogen atoms are used instead of oxygen. Transport through the molecule now displays low-bias excitations. The magnetic and temperature dependence of these excitations point to two unpaired electrons on the molecule, forming a single/triplet state. The presence of two unpaired electrons is suggested to be due to the broken conjugation of the carbons at the hydrogen side groups. This molecule thus effectively forms a strongly coupled double quantum dot.

Replacing the two hydrogens with a 1,3-dithiole group (chapter 5), again results in the observation of low-energy excitations that can be linked to two unpaired electrons. However, the energy of the excitation can now be strongly tuned by the gate electrode. A possible mechanism for this is differential gating due to the presence of two spatially separated orbitals.

Chapter 6 is on a different topic than the preceding three chapters. Here, the conductance of a molecule with azomethine linkers is determined statistically with the mechanically controlled break-junction technique. The conductance is shown to be comparable to its vinyl analogue, which is widely used in molecular and organic electronics. Azomethine linkers have the advantage that they are more easily formed and less demanding on the environment than vinyl bonds.

The last chapter is the outlook, here we discuss the opportunities of molecular electronics with a specific focus on the effects studied in this thesis. The limited gate coupling is identified as one of the main challenges. Electrochemical gate, graphene electrodes and designing molecules focused on enhancing the gate coupling are suggested as potential solutions. In the last part of the outlook, a molecule is proposed that incorporates both broken conjugation and quantum interference to probe single-electron tunneling events in a single molecule.

SAMENVATTING

Onderzoek aan nieuwe elektronische materialen drijft de ontwikkeling van elektronische apparaten en componenten. In de moleculaire elektronica wordt elektron transport door enkele moleculen bestudeerd. Doelen zijn om moleculaire elektronische materialen te ontwikkelen en elektronische componenten te realiseren op moleculaire schaal. Dit proefschrift gaat grotendeels over het gebruik van de electromigratie techniek om experimenteel onderzoek uit te voeren aan elektron transport door drie verschillende anthraceen-achtige moleculen. De drie moleculen zij identiek, afgezien van de zij-groepen aan de middelste ring van het anthraceen.

Als zuurstof zij-groepen worden gebruikt (hoofdstuk 3), is de niet-resonante geleiding afhankelijk van het aantal elektronen op het molecuul. Met behulp van theoretische berekeningen kan deze afhankelijkheid toeschreven worden aan de opheffing van destructieve kwantuminterferentie als gevolg van het toevoegen van het extra elektron op het molecuul.

Als er in plaats van het zuurstof atoom twee waterstof atomen worden gebruikt (hoofdstuk 4), verschijnen er laag-energetische excitaties. De temperatuur- en magneetafhankelijkheid van deze excitaties suggereren dat ze veroorzaakt worden door de aanwezigheid van twee ongepaarde elektronen op het molecuul. De verklaring voor het ontstaan van de ongepaarde elektronen is de gebroken conjugatie in het molecuul die gecreëerd wordt door de waterstof zij-groepen. Dit zorgt effectief voor de vorming van een dubbele kwantum dot in het molecuul.

Wanneer de twee waterstof atomen worden vervangen door een 1,3-dithiole groep (hoofdstuk 5), verschijnen er ook laag-energetische excitaties. Maar bij dit molecuul is de energie van de excitatie sterk afhankelijk van het elektrisch veld. De metingen wijzen in de richting van differentiaal gating door de aanwezigheid van twee ruimtelijk van elkaar verwijderde orbitalen in het molecuul.

Hoofdstuk 6 gaat over een ander onderwerp binnen de moleculaire elektronica. Hier wordt met behulp van de mechanische gestuurde breakjunctie de geleiding van een molecuul bepaald dat gebaseerd is op azomethine bindingen. De geleiding blijkt van dezelfde orde te zijn als die van moleculen met vinyl bindingen. Die moleculen zijn veelvuldig in gebruik in organisch en moleculaire elektronica. Azomethine bindingen hebben het voordeel dat ze gemakkelijker te maken en minder belastend zijn voor het milieu dan de vinyl bindingen.

Het laatste hoofdstuk van dit proefschrift behandelt mogelijke vervolgprojecten in de moleculaire elektronica, met een focus op de effecten bestudeerd in dit proefschrift. De vaak gelimiteerde gate koppeling wordt gezien als de grootste uitdaging. Elektrochemisch gaten, grafeen elektrodes en het ontwerpen van moleculen gericht

op het vergroten van de gate koppeling worden geopperd als een mogelijkheid om dit op te lossen. Verder wordt er een suggestie gedaan voor een molecuul dat dubbel kwantum dot gedrag en kwantum interferentie combineert om het tunnelen van een enkel elektron door het molecuul te bestuderen.

CURRICULUM VITÆ

Max KOOLE

03-05-1987	Born in Seria, Brunei.

EDUCATION

1999–2005	Secondary school British School Muscat, Oman (1999–2001) International School Hilversum, The Netherlands (2001–2005)
2005–2010	Bachelor Applied Physics Delft University of Technology, The Netherlands *Thesis:* Modeling Slow Light in Alkali Vapors *Supervisor:* dr. N. Akopian
2010–2012	Master Applied Physics Delft University of Technology, The Netherlands *Thesis:* Gated Mechanically Controlled Breakjunctions & Negative Differential Resistance in Dihydroanthracene *Supervisor:* dr. ir. M.L. Perrin & Prof. dr. ir. H.S.J. van der Zant
2011	Internship University of New South Wales, Australia *Project:* Optical Ionisation and Electrical Detection of single Dopants in Solid State Structures *Supervisor:* dr. ir. J.A. Mol & Prof. dr. S. Rogge
2012–2017	Ph.D. Applied Physics Delft University of Technology, The Netherlands *Thesis:* Molecular Electronics: When Multiple Orbitals Matter *Promotor:* Prof. dr. ir. H.S.J. van der Zant

LIST OF PUBLICATIONS

6. M Koole, JC Hummelen, HSJ van der Zant, *Spin excitations in an all-organic double quantum dot molecule*, Phys. Rev. B **94**, 165414 (2016).

5. M Mansø, M Koole, M Mulder, IJ Olavarria-Contreras, L Andersen, M Jevric, SL Broman, A Kadziola, O Hammerich, HSJ van der Zant, MB Nielsen, *Synthesis and Single-Molecule Conductances of Neutral and Cationic Indenofluorene-Extended Tetrathiafulvalenes: Kondo Effect Molecules*, J. Org. Chem. **81**, 8406-8414 (2016).

4. M Koole, R Frisenda, ML Petrus, ML Perrin, HSJ van der Zant, TJ Dingemans, *Charge transport through conjugated azomethine-based single molecules for optoelectronic applications*, Org. Electron. **34**, 38-41 (2016).

3. M Koole, JM Thijssen, H Valkenier, JC Hummelen, HSJ van der Zant, *Electric-field control of interfering transport pathways in a single-molecule anthraquinone transistor*, Nano Lett. **15**, 5569-5573 (2015).

2. JO Island, A Holovchenko, M Koole, PFA Alkemade, M Menelaou, N Aliaga-Alcalde, E Burzurí, HSJ van der Zant, *Fabrication of hybrid molecular devices using multi-layer graphene break junctions*, J. Phys.-Condens. Mat. **26**, 474205 (2014).

1. ML Perrin, R Frisenda, M Koole, JS Seldenthuis, JA Celis Gil, H Valkenier, JC Hummelen, N Renaud, FC Grozema, JM Thijssen, D Dulić, HSJ van der Zant, *Large negative differential conductance in single-molecule break junctions*, Nat. Nano. **9**, 830-834 (2014).

ACKNOWLEDGEMENTS

The past four years working at MED has been a very valuable experience. I am impressed by the drive and passion that colleagues (from PI's to bachelor students) display in doing science. The great diversity of nationalities has surprised me as one of the unexpected perks of doing a PhD, where the difference in culture makes it possible to learn a lot about yourself and other people. There are many people who played an important role in this PhD. The list is long, so it is not on purpose if I forget to thank a few of you.

To start, Herre, thank you for offering me to do this PhD. I also want to thank you for the opportunity "to not play by the rules of the game" (Emre). You have taught me a lot about how to do science and what should be done to become a scientist. Some advice I neglected, which to my surprise you always tolerated. It is remarkable to see that with the amount of work you have, you still find the time to help me when I needed it. If there is one thing I would like to take with me, it is the peace and happiness you emanate, even when the proverbial shit hits the fan. If we would all do this the world would definitely be a happier place. Ferdinand, my co-promotor, our contact hours were limited, however I sincerely enjoyed the meetings we had. Thank you for writing the proposal that got my PhD funded. I would also like to thank Kees for the amazing molecules, for the chemists view of all my problems and for being part of my committee. I also want to thank the other committee members Professor Blanter, Professor Kuipers, Professor Hedegård and Professor Lafarge for taking time to be part of my PhD ceremony. Theo en Michiel, thank you for the opportunity to work together. I would also like to thank Mogens Brøndsted Nielsen, M. Herranz and Nazario Martín for the opportunity to work with their molecules.

Riccardo, the many years shaping my ideas with your destructive criticism was vital for creating the research which is now in this thesis. Emre, wherever you go the coming years I hope we can keep meeting up. Also the rest of the San Sebastian crew (Dejan, Rocco, Giordano, Santiago), we had an epic two weeks. With many follow ups in the years after. Nicola, Davide and Mickael, the ski trip was one of the social highlights. These trips resulted in a very social atmosphere in the lab. Ricardo, Mickael, and later also Nandini and Ignazio, who knew that French rap could be such a motivator. The right lab (Rocco, Enrique, Joeri), let the gospel sing! The left lab (Vera, Anastasia, Alexandra), good luck in starting, finishing and moving further in science. The delocalized one (Joshua), care to share some work ethos? Yanai, I believe in you, you can do it! Dirkfalda, good luck with becoming a science power couple. Nikos, take care of the Animal, watch out that it doesn't consume you. Tino! Dank voor alle gezelligheid. Ik zou als ik jou was een salaris verhoging aanvragen, gezien je bijbaan als

PhD-student motivator. Furthermore, I want to thank the PIs, staff and all the other students in MED for creating a nice and friendly place to work.

Beste Julia en Andries, jullie waren beiden cruciaal in hoe ik mijn PhD tot een einde heb gebracht. Hoe jij, Juul, jouw PhD hebt gedaan is erg dapper en een inspiratie voor mij. Jouw voorbeeld heeft geleid tot een leuk laatste jaar, iets wat vaak niet vanzelfsprekend is. Andries, in het derde jaar hebben we veel gepraat over het leven en wat je ermee kan doen als je je zorgen maar los laat, cruciaal voor een PhD. Koos en Jean-luc, dank voor het zijn van mijn paranimfen, de nonchalance die jullie beide tegenover het leven hebben vind ik erg indrukwekkend en in mijn ogen noodzakelijk in de positie van paranimf. Rotterdam Fawaka: Niels, Kees, Anne-Marije, Lex, Bush, Jotte, Jules, Perijne, Eva. Bedankt voor alle spontane dingen die gebeuren in Rotterdam, ik hoop dat we dit nog jaren kunnen doorzetten. Lex en Bart, als de cunningham maar strak staat. De tiger, maar ook de 16, gaven een heel fijn tegenwicht voor de PhD. Ik heb nu alweer zin in de zomer! Er zijn nog veel mensen die ik zou willen bedanken: Katrien & JW, de Nepal groep, Sven & Jooz, Lex & Bianca en de vrienden van Iris, dank voor alle gezelligheid en het luisteren naar de verhalen over enkele moleculen.

Mams, Koos, Tob en Emma, dankjulliewel voor alle steun in de afgelopen jaren en laten we ook de komende jaren veel plezier maken. Mams, bedankt voor je hulp met het ontwerpen van de voorkant. Rens, Roos, Pieter, Mieke, Maarten en Meike bedankt voor alle gezelligheid en de alsmaar expanderende familie. Iris, allerliefste, ik heb super veel zin in de toekomst met jou.